INTERNATIONAL JOURNAL OF
IJCOE
COASTAL, OFFSHORE & ENVIRONMENTAL ENGINEERING

Volume 7 | Issue 2 | May 2022

www.ijcoe.org info@ijcoe.org

International Journal of Coastal, Offshore and Environmental Engineering (IJCOE) Vol. 7 / Issue. 2 / May 2022

27

Since 2015

International Journal of Coastal, Offshore & Environmental Engineering

ISSN: 2980-8731 (online)

Volume 7 | Issue 2 | May 2022

IJCOE

Editor-in-Chief: Prof. Hamid S.Bahai

International Journal of Coastal, Offshore & Environmental Engineering
Since 2015
ISSN: 2980-8721 (online)

In The Name of God

Message from the Editor-in-Chief

The IJCOE journal office was established in 2015,and its first issue was published in 2016. TheIJCOE covers a wide range of research in thefields of oceanography & ocean technology, aswell as marine industries & marine engineering.The editorial board of IJCOE consists of nearly130 of the greatest scientists and researchersfrom over 30 countries worldwide, and thejournal's review board comprises 1,000 membersfrom all five continents. The membership andapplication process for joining the editorial andreview boards of this journal is ongoing. IJCOE isa research-academic quarterly journal that haspublication and distribution permissions fromthe Press Organization and permission topublish scientific-research articles from theMinistry of Science, Research, and Technology(MSRT) with an "A" rating. It also holds a "Q1"rating from the ISC institute with an impactfactor (IF) of approximately 0.43 and isconsidered a "core journal" (prestigious andoutstanding journal). IJCOE is an open-accessjournal and allows the download and receipt ofaccepted articles in full text for free. It respectsand adheres to copyright and COPE regulations.The journal's office operates 24/7, providingservices to researchers. In addition to publishinga regular quarterly journal, IJCOE has 16 specialissues on specific topics in preparation. It alsoprovides conditions for publishing specializedbooks, references, and handbooks. Moreover, itis ready to cooperate with the secretariats ofreputable international conferences to publishtheir selected and outstanding articles. IJCOEevaluates, appraises, and publishes books,articles, and the scientific achievements andfindings of esteemed researchers and scientistsworldwide who are innovating and conductingin-depth research in the "important and strategicfield of the maritime technology & Oceanengineering." It welcomes any form of jointcooperation with universities, research institutes,and related research centers at the national,regional, and international levels, and extends ahand for collaboration.

Classification of Editorial Board in IJCOE

Editor-in-Chief

Director-in-Chief

Deputy Editor

Executive Managers

English Text Editor

Technical Editor

International Editorial Board

National Editorial Board

Editorial Board Associate

Editorial Board Assistant

Guest Editorial Board

Advisory Board

Administrative Coordinator

Honorary Board Member

Methodology Advisor

Author Benefits

- Open Access
- Rapid Publication
- Thorough Peer-Review
- No Copyright Constraints
- Coverage by Leading Indexing Services
- Discounts On Article Processing Charges (APC)
- No Space Constraints, No restriction on the maximum length of the papers, number of figures or colors

INTERNATIONAL JOURNAL OF IJCOE COASTAL, OFFSHORE & ENVIRONMENTAL ENGINEERING

Aims of IJCOE

Hydrodynamics

Marine equipment

Structural mechanics

Ocean environmental predictions

Stochastic calculations Experimental

Automatic Control of Marine Systems

Scope of IJCOE

Marine Hazards

Ocean Acoustics

Naval Architecture

Ocean Engineering

Coastal Engineering

Marine Meteorology

Marine Earth Sciences

Underwater Technology

Marine Renewable Energy

Polar & Arctic Engineering

Marine Renewable Energy

Marine Geography & Geodesy

Marine Environmental Engineering

Automatic Control of Marine Systems

Hydro Physics & Physical Oceanography

Type of papers

- Case Studies
- Book Reviews
- Review Article
- Letters to the Editor
- Methodology Papers
- Editorials and Commentaries
- Response or Rejoinder Papers
- Perspective or Opinion Papers
- Conceptual or Theoretical Papers
- Meta-Analysis and Systematic Reviews
- Short Communications or Brief Reports
- Research Articles (Original Research Papers)

Scientific Research Journal

Ministry of Science, Research And Technology (MSRT)

Jurnal Ranking 2023: A

Ministry Of Science, Research And Technology (ISC)

Citation Impact 2022: 0.429

Quartile 2022 : Q1

Core Collection

IJCOE is a Member of

Cantact Us

Office 1 | Research Institute of Meteorology and Atmospheric Science

Address | Tehran, Shahid Kharrazi Highway, Pajoohesh Blvd, Research Institute of Meteorology and Atmospheric Science, Sand and Dust Storm International Research Center (SDS-IRC), No. 13, 1st floor.

Phone | +982144787652

Postal code | 13611-14977

website | www.rimac.ac.ir

Office 2 | Iranian National Institute for Oceanography and Atmospheric Science

Address | Tehran, Dr. Fatemi Gharbi St., Shahid Etemadzade St., No. 3, third floor.

Phone | +982166944873

Postal code | 13389 – 14118

website | www.inio.ac.ir

Email | Info@ijcoe.org

Website | www.ijcoe.org

Follow Us

www.ijcoe.org

INTERNATIONAL JOURNAL OF IJCOE COASTAL, OFFSHORE & ENVIRONMENTAL ENGINEERING

Volume & Issue:

Volume 7, Issue 2, May 2022

Number of Articles: 6

Content

INTERNATIONAL JOURNAL OF
COASTAL, OFFSHORE & ENVIRONMENTAL ENGINEERING IJCOE Vol.7/No. 2/Spring 2022 (1-10)

Available online at: www. Ijcoe.org

Inter-comparison of single-sensor and merged multi-sensor ocean color chlorophyll-a products in the shallow turbid waters - case study: Persian Gulf

Masoud, Moradi

Iranian National Institute of Oceanography and Atmospheric Science, moradi_msd@yahoo.com

ARTICLE INFO

Article History:
Received: 15 Dec. 2021
Accepted: 15 Mar. 2022

Keywords:
Remote sensing
Phytoplankton
Spatial coverage
Complex waters
Dusty atmosphere

ABSTRACT

Ocean color satellite sensors provide the only long-term Essential Climate Variable (ECV) globally that targets Chlorophyll-a concentrations (Chl-a) as the most important biological factor in the oceans. It is difficult to develop the long-term and consistent ocean color time-series for climate studies due to the differences in characteristics, atmospheric correction, Chl-a retrieval algorithms, and limited lifespans of individual satellite sensors. Therefore, the merged multi-sensor ocean color datasets were developed by merging data from different satellite sensor products. The performance of the commonly used single-sensor and multi-sensor merged ocean color datasets is a challenging issue over highly turbid coastal waters and dusty atmospheric conditions. In this study, we compared the common single-sensor [Sea-viewing Wide Field-of-view Sensor (SeaWiFS), Moderate Resolution Imaging Spectroradiometer (MODIS), Medium Resolution Imaging Spectrometer (MERIS), Visible Imager Radiometer (VIIRS), and Sentinel-3 Ocean and Land Colour Instrument (OLCI)], and merged multi-sensor [Ocean Colour Climate Change Initiative (OC-CCI), and GlobColour weighted average (GC-AVW) and Garver-Siegel-Maritorena (GC-GSM)] Chl-a datasets over the Persian Gulf, known as optically complex and highly turbid water bodies in a dusty atmospheric condition. The results indicate that the OC-CCI dataset provides more spatial and temporal coverages than the other datasets. Temporal consistency between single-sensor and merged datasets was made in two different timespans during the common period of sensors and during the continuous lifespan intersection between individual two-paired of datasets. The statistical metrics were calculated to show the temporal consistency between Chl-a datasets during the common and continuous time periods. Correlation between OC-CCI and the other datasets showed that the relationships between datasets did not change significantly during the proposed time periods. Further, it was indicated that the OC-CCI product is more constant than the other single-sensor and merged products. It was shown that OC-CCI datasets were more consistent with MERIS and GC-GSM datasets, and SeaWiFS and GC-AVW were not significantly correlated to the other datasets. The results revealed that the single sensor products that use POLYMER atmospheric correction algorithm (e.g. MERIS), and merged multi-sensor product that performs the GSM blending algorithms (e.g. GC-GSM) are more consistent and stable than the other products over the study area.

1. Introduction

Marine phytoplankton display a great role in the cycling of other elements in the marine environments including iron, silica, nitrogen, nitrate, and phosphate [1]. They also consume carbon dioxide and control the cycling of carbon over global oceans [2]. Knowledge of phytoplankton variations and abundances is used to predict the impact of marine ecosystem on climate variability and climate change [3]. Hence, monitoring of phytoplankton variations with proper temporal and spatial resolutions is an imperative task for climate change and marine ecosystem studies [4].

Ocean color has been indicated as an Essential Climate Variable (ECV) for climate research purposes [4]. In this regard, ocean color datasets should be sustainable at least over a few decades because of decadal

variability of oceanic factors [5,6]. Ocean color remote sensing is the only available technique for monitoring of phytoplankton on synoptic scales, and it provides time-series datasets of chlorophyll-a concentration (Chl-a) as an indicator of phytoplankton abundances. However, ocean color satellite sensors have limited lifespans typically about 10 years, and visible spectral radiometry, which is used for ocean color estimations, needs to be improved. This type of improvements includes: failure to identify the source of errors related to the main features retrieved by standard methods, reduction of consistency in data due to the different spectral characteristics of sensors performed in successive mission, occurrence of missing data, gaps in datasets, limited duration of each satellite mission. Therefore, continuous time-series ocean color data are required to be merged from different satellite missions as seamless data and free of artificial gaps, missing data, and trends which rise from blending of disparate ocean color datasets.

European Space Agency (ESA) developed the first ocean color blended time series from different single satellite sensors in 2010, known as Ocean Colour Climate Change Initiative (OC-CCI). The OC-CCI has generated globally by merging observations from Sea-viewing Wide Field-of-view Sensor (SeaWiFS), Moderate Resolution Imaging Spectroradiometer (MODIS), and Medium Resolution Imaging Spectrometer (MERIS) satellite sensors [4]. The final version of OC-CCI has been corrected for inter-sensor biases and all radiometric bands shifted to the bands of SeaWiFS. The OC-CCI performs the POLYMER atmospheric correction algorithm applied to MERIS and MODIS [7]. Similarly, the Copernicus Marine Environment Service (CMEMS) has developed a regular dataset for marine ecosystems globally on the physical state of marine environment including temperature, currents, salinity, sea surface height, sea ice, marine optical properties, and ocean color chlorophyll-a concentrations (known as GlobColour) [8]. The GlobColour merged Chl-a products have been generated based on observations from SeaWiFS, MERIS, MODIS, Visible Imager Radiometer (VIIRS), and Sentinel-3 Ocean and Land Colour Instrument (OLCI). GlobColour has performed different algorithms to retrieve Chl-a from reflectance data. It uses three algorithms including: the Ocean Color Index (OCI) algorithm for oligotrophic waters (9), common NASA OCX (OC3 and OC4) algorithms depending on the sensor, and the OC5 algorithm [10] for coastal complex waters. The OC-CCI and GlobColour datasets are available from 1997 to present and provide fewer missing data than any other single sensor ocean color dataset. They both use OC5 and OCI Chl-a retrieval algorithms over complex turbid waters [8], and often provide relatively similar datasets in the coastal waters, although some differences exist because of the merging and flagging approaches. The OC5 and OCI retrieval algorithms have been developed for SeaWiFS, MERIS, MODIS, VIIRS, and OLCI sensors over the complex water bodies. Therefore, merged multi-sensor and single-sensor Chl-a products are available in the complex turbid coastal water bodies with similar retrieval algorithms.

Comparing the OC-CCI and GlobColour datasets with those available from single sensor data in the coastal complex waters provide required information for adopting the most reliable Chl-a data for studying the phytoplankton dynamics from all available ocean color datasets. However, the accuracy of long-term merged and single sensors Chl-a datasets in the complex water bodies remains as a challenging issue. Furthermore, comparison of merged multi-sensor with single-sensor Chl-a datasets contributes to give some insight on the uncertainties affecting the Chl-a products in the coastal turbid waters. In this article, we evaluate the performance of OC-CCI and GlobColour merged multi-sensor Chl-a datasets with other existing single-sensor (SeaWiFS, MERIS, MODIS, VIIRS, and OLCI) satellite-derived Chl-a using OCI and OC5 algorithms in the highly turbid complex waters of the Persian Gulf. We focus on the instabilities in the merged Chl-a products that rise from merging and flagging of merged multi-sensor observations, and demonstrate the consistency between different Chl-a datasets which have been estimated using similar retrieval algorithms (OC5 and OCI).

2. Data and Methods

2.1. Satellite data

The Chl-a datasets used in this study comprise from monthly different single-sensor and merged multi-sensor satellite datasets with spatial resolution 4km during 1997-2020. The single-sensor datasets were obtained from National Aeronautics and Space Administration (NASA) ocean color website (http://oceandata.sci.gsfc.nasa.gov/) during their mission lifespans including: SeaWiFS (1997-2010), MERIS (2002-2012), MODIS (2002-2020), VIIRS (2012-2020), and OLCI (2016-2020). The OC5 retrieval algorithm was performed to retrieve Chl-a from each of the selected satellite sensors during the time period.

Two different Chl-a datasets are available from GlobColour (hereafter known as GC) that differ in the merging techniques. The GlobColour provides the weighted average (GC-AVW) and the Garver-Siegel-Maritorena (GC-GSM) datasets. The daily Chl-a products from level-2 of the single-sensor datasets were computed and then the corresponding Chl-a from SeaWiFS and MODIS were adjusted to the Morel algorithm [11] to transforms the Chl-a data to the MERIS data [8]. The GC products performs the OC5 algorithms for Chl-a retrieval in the complex waters and utilizes Neural Network merging approaches to develop Level-3 gridded datasets [12]. The number of

valid pixels from each sensor was used as the weights in the merged products. The monthly datasets of both GC were downloaded from CMEMS website (http://www.globcolor.info) and transformed in local plate carree grid format with average spatial resolution of 4km.

The OC-CCI uses the OC5 and OCI retrieval algorithms to estimates Chl-a and performs the POLYMER atmospheric correction algorithm [4]. Hence, the Chl-a datasets of OC-CCI comprise high number of measurements from MERIS and show a better spatial coverage than the other single-sensor and/or merged products [8]. Here, the monthly of OC-CCI version 5.0 downloaded from ESA website (http://www.esa-ocean clour-cci.org) and then transformed in local plate carree grid format with average spatial resolution of 4km. The spatial and temporal resolution of merged multi-sensor and single sensor ocean color derived Chl-a datasets were matched for comparisons and further analysis.

2.2. Methods

The OC-CCI and GC datasets are compared with the corresponding records of single-sensor (SeaWiFS, MERIS, MODIS, VIIRS, and OLCI) Chl-a datasets pixel-by-pixel across the whole Persian Gulf. The bias (δ), unbiased root mean square (RMS) and its difference (Δu,RMS), mean ratio (φ), and correlation coefficient (r) are used to calculate the consistency between Chl-a datasets. These statistical indices are metrics commonly used for assessment and comparison evaluation of products of satellite-derived Chl-a [13]. The analyses were performed in two groups: (a) for common period with continuous observations that is no gaps in the monthly datasets in the purpose of assessing the similarity between each record, given: 2002-2010 for SeaWiFS, MERIS, MODIS, and merged-sensor datasets, and 2016-2020 for MODIS, VIIRS, OLCI, and merged-sensor datasets, and (b) for periods to any pair of datasets. The monthly Chl-a datasets were transformed to Log10 bases (here after will be shown as Log10(Chl-a)) before analyses to fully cover the log-normal distribution of these datasets [14]. The bias (δ) is calculated as bellow [15]:

$$\delta = \frac{1}{N}\sum_{i=1}^{n}[Log10(y_i) - Log10(x_i)] \quad (1)$$

where N is the total number of matched observations, y_i and x_i are the pairs of observations. The unbiased RMS ($\Delta_{u,RMS}$) is defined as [16]:

$$\Delta_{u.RMS} = \left(\frac{1}{N}\sum_{i=1}^{N}\{[log10(y_{2.i}) - \overline{log10(x_{2.i})}] - [log10(y_{1.i}) - \overline{log10(x_{1.i})}]\}\text{^}2\right)^{1/2} \quad (2)$$

The average values are shown with overbars. The mean ratio (φ) is defined as:

$$\emptyset = \frac{1}{N}\sum_{i=1}^{n}\frac{y_{2.i}}{y_{1.i}} \quad (3)$$

Unbiased RMS is defined as:

$$\text{RMS} = \sqrt{\frac{1}{n}\sum_{i=1}^{n}[Log10(y_i) - Log10(x_i)]^2} \quad (4)$$

The relationship between datasets are defined using the multiple statistical metrics defined above, that makes interpretation difficult. To do this, Target and Taylor diagrams are used to combine and summarize the results [16]. These diagrams have been widely used in remote sensing researches and represents one the most quantitate description of consistency between datasets [17–19]. Taylor diagram displays the standard deviation (σ), correlation coefficient (r), and unbiased RMS between pairs of data [20]. Target diagrams show the bias (δ) and Δu,RMS in a scatter polar plot [16].

The accurate consistency between two datasets are clearly indicated using time-series analysis of the unbiased differences between measurements of two different datasets [21]. Δu,RMS (equation 2) is used as a measure of consistency between two datasets, and the smaller values represent a more stable relationship.

3. Results

3.1. Spatial and temporal coverage

To compare the monthly Chl-a imageries from the selected single and merged-sensor, missing data were excluded from all satellite sensors. Only common grid pixels with valid measurements were used in the statistical analysis to minimize the influence of spatio-temporal bad sampling among datasets. However, we have to acknowledge that the effect of missed data would not have been entirely eliminated because there are desperate number of satellite sensor measurements due to differences in orbits and sampling rates which have been used by data providers to compute the monthly averages. Fig. 1 shows the percent of valid observation of each datasets over the entire period of each satellite mission, given that: SeaWiFS 1997-2010, MERIS 2002-2012, MODIS 2002-2020, VIIRS 2012-2020, OLCI 2016-2020, GC-GSM and GC-AVW 1997-2020, OC-CCI 1997-2020. The geographical distribution of valid measurements over grid point measurements seems to be regular, with the most valid

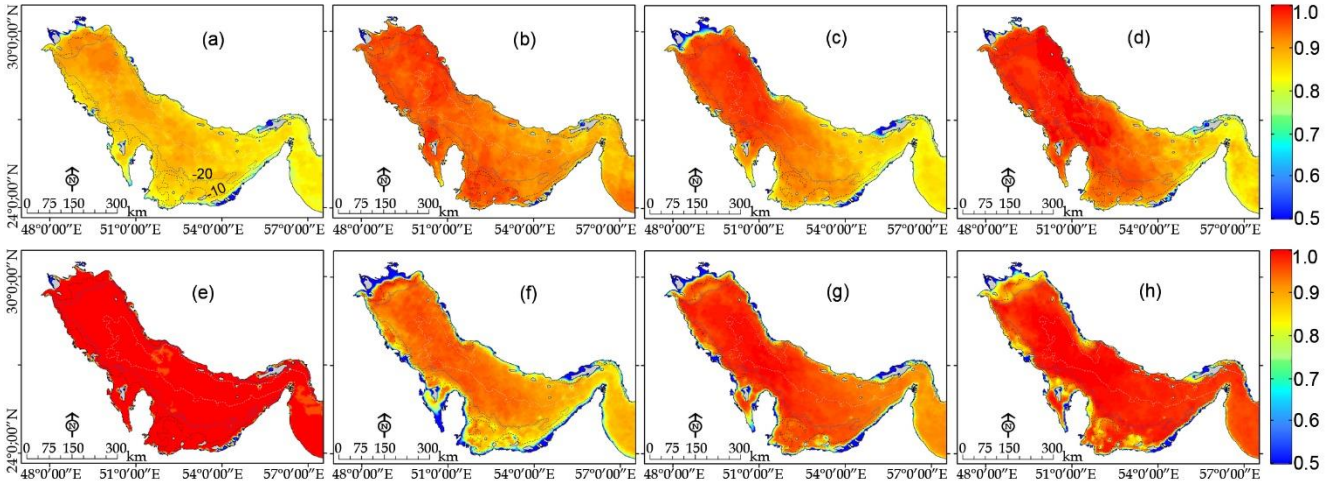

Figure 1. Spatial coverage of the percentage of valid measurements during the lifespan of each dataset. (a) SeaWiFS, (b) MERIS, (c) MODIS, (d) VIIRS, (e) OLCI, (f) GC-AVW, (g) GC-GSM, (h) OC-CCI. Overlaid dashed lines show isobaths. Color bars show percentage of the valid measurements, given bad observations and missing data eliminated.

points in the deeper areas and lowest valid points along coastal areas. Among the single sensor data sets, SeaWiFS (Fig. 1a) and OLCI (Fig. 1e) show the lowest and highest number of valid measurements in the deeper areas of the Persian Gulf, respectively. Among merged-sensor datasets, GC-GSM (Fig. 1g) and OC-CCI (Fig. 1h) show the highest (>0.93) and GC-AVW (Fig. f) shows the lowest (>0.84) percent of spatial coverage valid measurements. In all cases, the spatial coverage of valid data along the coastal regions (depth <10 m) are less than 0.65 of satellite measurements. Along the north-west regions of the Persian Gulf, the percentage of valid measurements is less than 0.55 for all of the datasets.

The number of valid monthly observations (N) of each Chl-a datasets across Persian Gulf during the study period are shown in Fig. 2. The N values of the single-sensor datasets are about 13600 for SeaWiFS, 13700 for MERIS, 13600 for MODIS, 13700 for VIIRS, and 13800 for OLCI. During the temporal coverage by merged datasets from 1997 to 2020, the number of valid monthly measurements increased greatly from mid-2002 onward. Before mid-2002, the N values of OC-CCI, GC-AVW, and GC-GSM were 12300, 12500, and 12200, respectively. After mid-2002, the N values of OC-CCI increased in average to 14200 till mid-2002, and then decreased to 13300. The N values of GC-AVW and GC-GSM reached in average to 13300 after mid-2002 and continued to the end of 2020. The OC-CCI uses the MERIS datasets as a reference of atmospheric correction (POLYMER) to blend the other sensor Chl-a data. Hence, during the lifespan of MERIS (Mid-2002 to 2012) the OC-CCI datasets show the greatest values of valid observations.

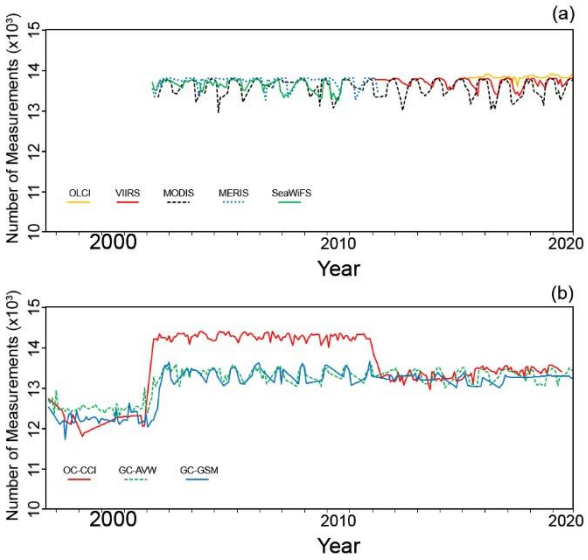

Figure 2. Temporal coverage of valid monthly measurement across grid pixels of Persian Gulf (Fig. 1) during the lifespan of single-sensor (a) and merged-sensor (b) datasets.

3.2. Comparison of Chl-a datasets in common periods

Here, we considered the common time periods as a frame of temporal coverage from July-2002 to Nov-2010 to compare SeaWiFS, MERIS, MODIS, and the three merged datasets, and from Apr-2016 to Dec-2020 to compare MODIS, VIIRS, OLCI, and the three merged datasets. Previous studies show that the OC-CCI datasets have the greatest correlation with in situ Chl-a measurements than the other single-sensor and merged datasets across the Persian Gulf [22]. Further, the OC-CCI shows the most temporal continuous valid monthly observations in the study area that covers the temporal coverages of the whole proposed common periods (Fig. 2). Therefore, we deem the OC-CCI as a baseline observation and calculate the statistical parameters according to this data.

Table 1. Statistical results of the spatially averaged between OC-CCI and selected single-sensor and all GC datasets during the common time periods. All correlations have been calculated for p<0.05, N is the number of matched common monthly observations between data pairs. P1% and P99% are the 1st and 99th percentiles.

Period	Dataset	φ	r	$\Delta_{u,RMS}$	δ	mean	σ	$P_{1\%}$	$P_{99\%}$	N
2002-2010	SeaWiFS	0.830	0.734	0.291	0.217	1.140	0.395	0.751	3.374	94
	MERIS	0.831	0.895	0.173	0.215	1.142	0.313	0.761	2.668	101
	MODIS	0.728	0.728	0.179	0.362	0.995	0.260	0.583	2.969	101
	GC-AVW	1.293	0.709	0.323	-0.411	1.769	0.248	1.086	3.833	101
	GC-GSM	0.618	0.872	0.174	0.505	0.852	0.466	0.426	3.668	101
2016-2020	MODIS	0.742	0.757	0.171	0.053	0.977	0.256	0.628	1.325	51
	VIIRS	0.784	0.789	0.114	0.219	0.811	0.185	0.578	1.425	51
	OLCI	1.085	0.695	0.116	-0.076	1.106	0.136	0.851	1.460	51
	GC-AVW	1.289	0.771	0.385	-0.318	1.348	0.498	0.810	1.103	51
	GC-GSM	0.619	0.878	0.083	0.384	0.645	0.175	0.356	1.089	51

The OC-CCI dataset showed the highest correlation with MERIS (r=0.89) among single-sensor datasets, and GC-GSM among the merged datasets (r=0.87) during the mid-2002 to mid-2010. The spatial average value of Chl-a during this time period was 1.358±0.176 mg m-3, the 1st percentile 0.587 mg m-3, and 99th percentile 3.946 mg m-3. The average and percentile values were closer to the corresponding value of merged datasets rather than those found in single-sensor statistical values. The significant Correlations (p<0.05) between OC-CCI and merged and single-sensor datasets were not robust enough (0.73>r>0.89), and differences were relatively big, given by Δu,RMS>0.1 and δ<0.1 (Table 1). In general, the similarity and lowest differences between OC-CCI were observed with MERIS among single-sensor, and GC-GSM among merged datasets.

During the second common period (Apr-2016 to end of 2020), the highest correlation was observed between OC-CCI and GC-GSM (r=0.88). The results of the comparison during the second common period is very similar to the firs common period, and differences between OC-CCI and single-sensor datasets are relatively high (Table 1). The spatial average value of Chl-a during this time period was 1.031±0.158 mg m-3, the 1st percentile 0.627 mg m-3, and 99th percentile 3.416 mg m-3. In general, the similarity and lowest differences between OC-CCI were observed with VIIRS among single-sensor, and GC-GSM among merged datasets during the time period 2016-2020.

Tylor diagram suggests an obvious similarity between OC-CCI and GC-GSM and MERIS than the other datasets (Fig. 3a, b). Comparison of OC-CCI with VIIRS and OLCI show an analogous result, and the GC-AVW showed to be the least similar dataset with OC-CCI. This analysis revealed that MODIS and SeaWiFS as the most dissimilar datasets to OC-CCI products among single-sensor records (Fig. 3a). The OC-CCI showed negative bias (δ) in relation to all datasets except OLCI and GC-AVW. The GC-AVW shows the greatest positive bias value to the OC-CCI. The both merged datasets, GC-AVW and GC-GSM, show the greater values of unbiased difference RMS (Δu,RMS) value to the OC-CCI in relation to the single-sensor datasets (Fig. 3c, d).

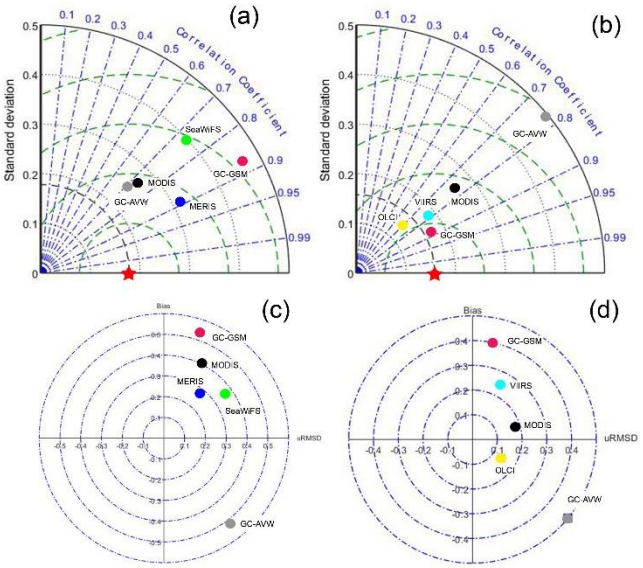

Figure 3. Taylor and Target diagram for common period observations from July-2002 to Nov-2010 (a, c), and from Apr-2016 to Dec-2020 (b, d) when comparing OC-CCI with single-sensor and merged monthly datasets.

Time-series of similarity metrics calculated using statistical correlation analysis between OC-CCI with the other datasets across the Persian Gulf at discrete time for each statistical metric. Time-series of all metrics showed strong interannual fluctuations during both proposed common periods (2002-2010 and 2016-2020). The timings of high and low peaks for each of the statistical metrics are not similar and depends on the target dataset (Fig. 4 and 5). Fig. 4 indicates that the

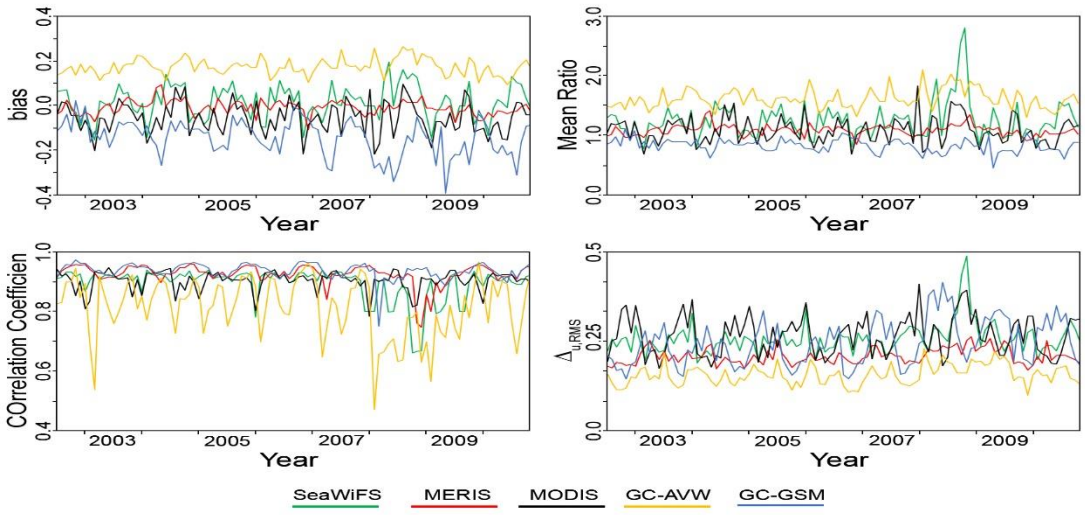

Figure 4. Time-series of statistical similarity metrics between OC-CCI, merged and single-sensor datasets during July-2002 to Nov-2010.

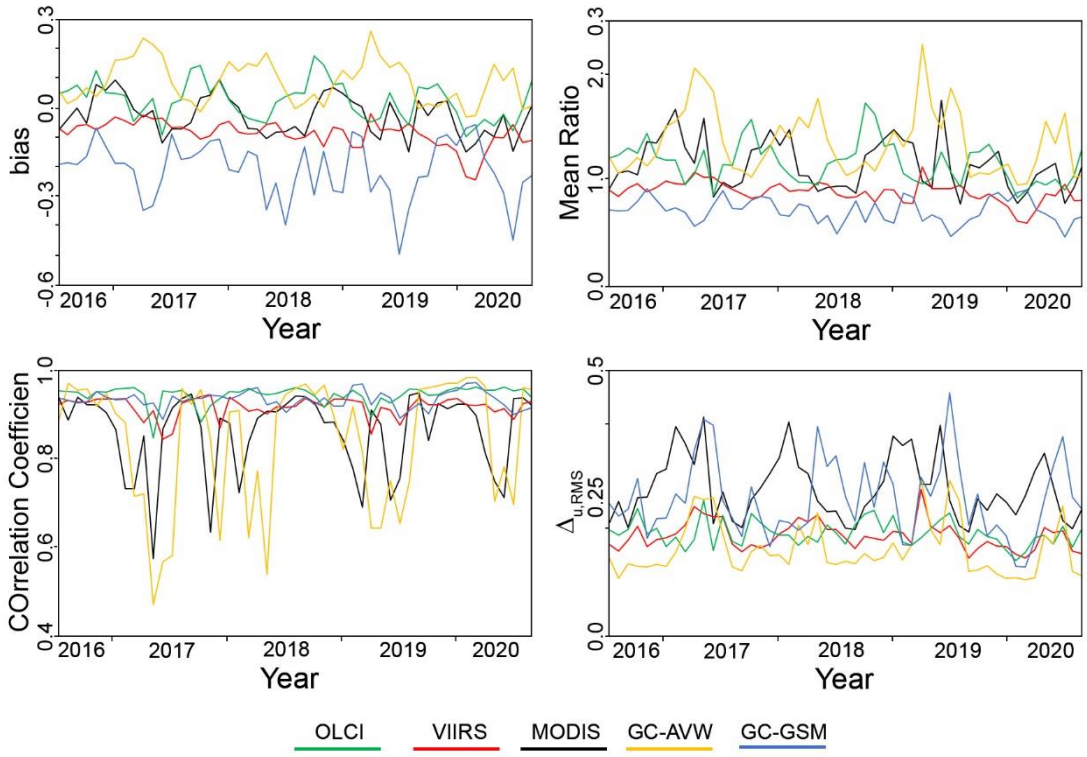

Figure 5. Time-series of statistical similarity metrics between OC-CCI, merged and single-sensor datasets during Apr-2016 to Dec-2020.

MERIS and GC-GSM datasets are the most similar datasets, and in contrast the GC-AVW and MODIS are the most different datasets when comparing with OC-CCI during 2002-2010. Similar results were obtained from time-series analysis of statistical metric during 2016-2020 (Fig. 5). During the summer, MODIS and GC-AVW showed higher values of Δu,RMS and bias (δ), and lower values of correlation coefficients relative to the other datasets during the both common periods (Fig. 4 and 5).

3.3. Comparison of Chl-a datasets in long-term period

Fig. 6 shows the spatially averaged time series of Chl-a values obtained from different single-sensor and merged datasets during the whole lifespan of all missions. All datasets show similar seasonal and interannual fluctuations, although the magnitude of peaks and troughs are not the same. A distinct peak is observed at late of 2008 which is correspond to the occurrence of a monstrous red tide in the Persian Gulf [23–25], and it has been detected in all merged and

single datasets. The results of statistical analysis of comparison between OC-CCI with the other datasets are shown in Table 2. The highest correlation was observed between OC-CCI and MERIS (r=0.87) among single-sensor datasets, and with GC-GSM (r=0.81) among merged datasets. The spatial average value of Chl-a from OC-CCI (1.119±0.176 mg m-3) and percentiles (0.587 mg m-3 for 1st, and 3.946 mg m-3 for 99th) (Table 2) are relatively equal to those found during the common periods (section 3.2). The worst correlation coefficient values and more differences between were observed between OC-CCI and MODIS (r=0.56, Δu,RMS=0.22) among single-sensor, and GC-AVW (r=0.33, Δu,RMS=0.30) among merged datasets (Table 2).

Temporal variability of Δu,RMS is a consistency metric of similarity between OC-CCI and the other merged and single-sensor datasets (section 2.2). Comparison between OC-CCI and the other datasets showed that temporal variations of Δu,RMS is strongly seasonal (Fig. 7), and it follows the interannual and trends of Chl-a time-series, which have been found previously over the Persian Gulf [26,27]. The GC-GSM among merged, and MERIS among single-sensor datasets showed the most stable and more consistent relationship with OC-CCI. There is a reasonable shift between Δu,RMS of GC-AVW and GC-GSM that suggests the similarity between merged datasets with OC-CCI are not stable among them and varies through time. The greatest shift of Δu,RMS between OC-CCI and merged datasets is observed concurrent to the lifespan of MERIS into the presented time-series. Before that both merged datasets use only SeaWiFS measurements, and therefore no notable shifts of Δu,RMS were observed. Introduction of more additional datasets into the merged datasets increase the number of observations (Fig. 2), and makes these datasets more robust. However, due to the different Chl-a blending algorithm of OC-AVW and GC-GSM, the stability of relationship with OC-CCI dataset are different and GC-GSM follows more robust and consistent trend with OC-CCI.

4. Discussion

In this study, we compared the merged multi-sensor and single-sensor datasets in the highly turbid and dusty environment of the Persian Gulf during 1997-2020. The OC-CCI dataset offers the most spatial/temporal coverage of Chl-a observations globally, given 22.9 billion in total and 127 million daily pixels. The accuracy of OC-CCI dataset across the world has been studied, and showed that it could be a best choice for ocean color data source among all of the available datasets [4,8,21]. In general, marginal seas and high turbid coastal waters show great inconsistency and uncertainties in both merged and single-sensor datasets. Furthermore, over the dusty shallow seas, such as Persian Gulf, the accuracy of ocean color data decreases significantly and it is necessary to evaluate the influence of atmospheric correction and Chl-a retrieval in these environments. We showed previously that the OC-CCI is more consistent then single-sensor datasets with in situ measurements, and also it is more similar than the other standard ocean color datasets with those produced by five band channels Chl-a retrieval algorithms customized for coastal complex waters [22]. Hence, the OC-CCI was selected as a baseline to evaluate the temporal consistency of the single-sensor and merged datasets across the dusty atmosphere and complex waters of the Persian Gulf. The finding of this study identifies indirectly the influence of atmospheric correction and retrieval algorithms on the accuracies of the available Chl-a data products. Thus, comparison between OC-CCI with the other available Chl-a datasets reveals the performance and applicability of ocean color datasets across the study area and similar marine environment.

The quality and robustness of Chl-a products may be depredated when data are merged. As an example, SeaWiFS, MERIS, and MODIS single-sensor datasets are consistent and robust over the open oceans, while OC-CCI products showed to be more similar to these products than OC-AVW dataset [18,21]. Therefore, merged ocean color datasets do not offer similar products, and their accuracies should be assessed. Here, we showed that OC-CCI datasets show more consistency with MERIS and GC-GSM datasets, and the week similarity was observed between SeaWiFS and GC-AVW datasets. While SeaWiFS is the reference sensor for OC-CCI data blending (see section 1), it does not show a notable similarity with OC-CCI across the Persian Gulf. In contrast, MERIS shows a significant and highest correlation and small value of unbiased difference, as well as the small bias value. Since SeaWiFS and OC-CCI perform the same Chl-a retrieval algorithm and similar wavebands to estimate Chl-a concentrations, the week similarity level shows the Chl-a retrieval algorithms are notable influenced by atmospheric and environmental factor. However, MERIS shows the highest level of similarity with OC-CCI, that indicate the performed atmospheric correction of MERIS datasets are highly significant over the dusty and hazy environment of Persian Gulf. Hence, the POLYMER atmospheric correction algorithm is significantly the most prominent criterion for this similarity among single-sensor datasets. The greatest differences were found between GC-AVW and OC-CCI (Fig. 3), and it could be likely due to the use of different algorithm for Chl-a estimation. Nevertheless, similarity between merged datasets (GC) are differ from each other more than expected, GC-AVW and GC-GSM show the worst and the best similarity, respectively. It is not surprising because the

Table 2. Statistical results of the spatially averaged between OC-CCI and selected single-sensor and all GC datasets during the common time period. All correlations have been calculated for p<0.05, N is the number of matched common monthly observations between data pairs. P1% and P99% are the 1st and 99th percentiles.

	SeaWiFS	MERIS	MODIS	VIIRS	OLCI	GC-AVW	GC-GSM	OC-CCI
φ	0.833	0.824	0.802	0.796	1.085	1.314	0.749	-
r	0.715	0.866	0.562	0.791	0.695	0.331	0.815	-
$\Delta_{u,RMS}$	0.219	0.162	0.221	0.099	0.116	0.297	0.294	-
δ	-0.087	-0.081	-0.105	-0.102	0.033	0.112	-0.049	-
mean	1.134	1.111	0.946	0.807	1.106	1.473	0.807	1.119
σ	0.393	0.290	0.242	0.161	0.136	0.469	0.248	0.261
$P_{1\%}$	0.752	0.725	0.557	0.581	0.851	0.773	0.381	0.587
$P_{99\%}$	3.350	2.554	1.785	1.304	1.460	3.029	3.511	3.946
N	97	121	216	102	51	274	274	-

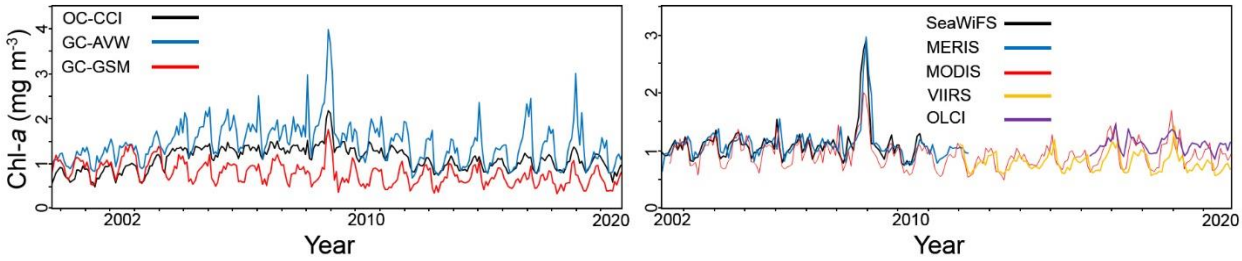

Figure 6. Time-series plot of spatially averaged of Chl-a across the Persian Gulf during the lifespan of merged (left) and single-sensor(right) datasets.

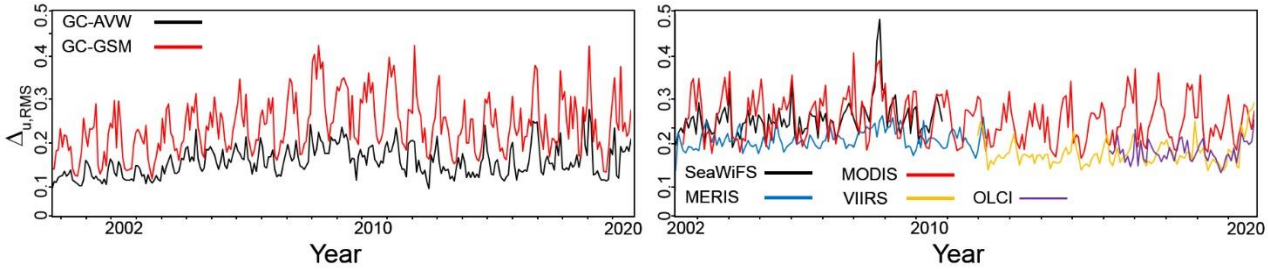

Figure 7. Time-series of Δu,RMS during the lifespan of merged and single-sensor datasets when comparing OC-CCI with merged (left) and single-sensor datasets (right).

two GC products are considerably different from each other in the atmospheric correction model, version of original data, and initial spatial resolution [4]. Therefore, it could be concluded that the proper atmospheric correction is more important than Chl-a retrieval algorithm in the dusty marginal seas such as Persian Gulf.

The merged datasets are produced using different blending algorithms to merge estimations of the different sources [8]. The presented results of this study suggests that the bias correction may increase the temporal consistency of the merged products, but our results do not recommend a distinct merging technique to enhance the long-term consistency. The comparison of two GC products yielded different results that could be due to the differences of both merging and flagging approaches [8,21]. However, all of the discrepancies between the single-sensor and merged products are expressed in the similarity between products and are reflected in the statistical metrics. Therefore, the results of this study present a rapid selection method for performing the available ocean color datasets, and it recommends the more accurate Chl-a datasets for the long-term studies across the Persian Gulf. Nevertheless, evaluating the performance of atmospheric correction and Chl-a retrieval algorithm across different climatic and environmental conditions in the dusty and complex marine environments remains a challenge.

5. Conclusions

This study addresses the inter-comparison of single-sensor and merged multi-sensor satellite-measured Chl-a over the optically complex and turbid waters under a dusty atmospheric condition of the Persian Gulf. The limited lifespan (10-year in average) of ocean color satellite sensors, beside the differences in their specifications, atmospheric correction and Chl-a retrieval algorithms make it difficult to create the long-term and consistent time-series ocean color datasets for climate change studies. Hence, creation of long-term datasets of near surface ocean color datasets is an essential task that achieved by merging the individual sensor missions to minimize the bias and uncertainties of single-sensor products. The OC-CCI dataset provides the most spatial and temporal coverages over the Persian Gulf during 1997 to 2020. Further, OC-CCI is the most prominent Chl-a record that matches the in situ measurements. Here, it was found that the OC-CCI dataset present a better performance in temporal robustness and consistency. The highest similarity and discrepancies between OC-CCI and the other Chl-a datasets were found with MERIS and GC-GSM, and SeaWiFS and GC-AVW, respectively. The results of this study showed that the single-sensor Chl-a datasets which performs the POLYMER atmospheric correction algorithm, and the merged multi-sensor products developed by GSM blending algorithm are the best choice of the Chl-a datasets over the Persian Gulf. However, further researches are recommended to assess the source and amount of uncertainties and discrepancies of atmospheric correction and Chl-a retrieval algorithms over the Persian Gulf.

Acknowledgment

This work has been supported by the Center for International Scientific Studies & Collaboration (CISSC), ministry of Science Research and Technology, Grant #990203. I express my gratitude to Dr. Masoud Sadreenasab, president of CISSC, for his kind cooperation.

6. References

[1] Platt T, Stuart V. (2008). *Why Ocean Colour? The Societal Benefits of Ocean-Colour Radiometry*. *vliz.be*. 1–8.

[2] Longhurst A, Sathyendranath S, Platt T, Caverhill C. (1995). *An estimate of global primary production in the ocean from satellite radiometer data*. Journal of Plankton Research. 17(6):1245–71.

[3] Muller-Karger FE, Kavanaugh MT, Montes E, Balch WM, Breitbart M, Chavez FP, et al. (2014). *A framework for a marine biodiversity observing network within changing continental shelf seascapes*. Vol. 27, Oceanography. p. 18–23.

[4] Sathyendranath S, Brewin RJ, Brockmann C, Brotas V, Calton B, Chuprin A, et al. (2019). *An ocean-colour time series for use in climate studies: The experience of the ocean-colour climate change initiative (OC-CCI)*. Sensors. 19(19):4285.

[5] Beaulieu C, Henson SA, Sarmiento JL, Dunne JP, Doney SC, Rykaczewski RR, et al. (2013). *Factors challenging our ability to detect long-term trends in ocean chlorophyll*. Biogeosciences. 10(4):2711–24.

[6] Racault MF, Le Quéré C, Buitenhuis E, Sathyendranath S, Platt T. (2012). *Phytoplankton phenology in the global ocean*. Ecological Indicators. 14(1):152–63.

[7] Steinmetz F, Deschamps P-Y, Ramon D. (2011). *Atmospheric correction in presence of sun glint: application to MERIS*. Optics Express. 19(10):9783.

[8] Garnesson P, Mangin A, D'Andon OF, Demaria J, Bretagnon M. (2019). *The CMEMS GlobColour chlorophyll a product based on satellite observation: Multi-sensor merging and flagging strategies*. Ocean Science. 15(3):819–30.

[9] Hu C, Lee Z, Franz B. (2012). *Chlorophyll a algorithms for oligotrophic oceans: A novel approach based on three-band reflectance difference.* Journal of Geophysical Research: Oceans. 117(1):1011.

[10] Gohin F, Druon JN, Lampert L. (2002). *A five channel chlorophyll concentration algorithm applied to Sea WiFS data processed by SeaDAS in coastal waters.* International Journal of Remote Sensing. 23(8):1639–61.

[11] Morel A, Huot Y, Gentili B, Werdell PJ, Hooker SB, Franz BA. (2007). *Examining the consistency of products derived from various ocean color sensors in open ocean (Case 1) waters in the perspective of a multi-sensor approach*. Remote Sensing of Environment. 111(1):69–88.

[12] Brewin RJW, Sathyendranath S, Müller D, Brockmann C, Deschamps PY, Devred E, et al. (2015). *The Ocean Colour Climate Change Initiative: III. A round-robin comparison on in-water bio-optical algorithms.* Remote Sensing of Environment. 162.

[13] Seegers BN, Stumpf RP, Schaeffer BA, Loftin KA, Werdell PJ. (2018). *Performance metrics for the assessment of satellite data products: an ocean color case study*. Optics Express. 26(6):7404.

[14] Campbell JW. (1995). *The lognormal distribution as a model for bio-optical variability in the sea*. Journal of Geophysical Research. 100(C7).

[15] Gregg WW, Casey NW, McClain CR. (2005). *Recent trends in global ocean chlorophyll*. Geophysical Research Letters. 32(3):1–5.

[16] Jolliff JK, Kindle JC, Shulman I, Penta B, Friedrichs MAM, Helber R, et al. (2009*). Summary diagrams for coupled hydrodynamic-ecosystem model skill assessment.* Journal of Marine Systems. 76(1–2):64–82.

[17] Saba VS, Friedrichs MAM, Antoine D, Armstrong RA, Asanuma I, Behrenfeld MJ, et al. (2011). *An evaluation of ocean color model estimates of marine primary productivity in coastal and pelagic regions across the globe*. Biogeosciences. 8(2):489–503.

[18] Djavidnia S, Mélin F, (2010). *Comparison of global ocean colour data records*. os.copernicus.org. 6:61–76.

[19] Werdell PJ, Franz BA, Bailey SW, Harding, Jr. LW, Feldman GC. (2007). *Approach for the long-term spatial and temporal evaluation of ocean color satellite data products in a coastal environment*. In: Coastal Ocean Remote Sensing. p. 66800G.

[20] Taylor KE. (2001). *Summarizing multiple aspects of model performance in a single diagram*. Journal of Geophysical Research Atmospheres. 106(D7):7183–92.

[21] Belo Couto A, Brotas V, Mélin F, Groom S, Sathyendranath S. (2016). *Inter-comparison of OC-CCI chlorophyll-a estimates with precursor data sets.* International Journal of Remote Sensing. 37(18):4337–55.

[22] Moradi M. (2021). *Evaluation of merged multi-sensor ocean-color chlorophyll products in the Northern Persian Gulf.* Continental Shelf Research. 221:104415.

[23] Al Shehhi MR, Gherboudj I, Ghedira H. (2014). *An overview of historical harmful algae blooms outbreaks in the Arabian Seas*. Marine Pollution Bulletin. 86(1–2):314–24.

[24] Moradi M, Kabiri K. (2012). *Red tide detection in the Strait of Hormuz (east of the Persian Gulf) using MODIS fluorescence data*. International Journal of Remote Sensing. 33(4):1015–28.

[25] Richlen ML, Morton SL, Jamali EA, Rajan A, Anderson DM. (2010). *The catastrophic 2008-2009 red tide in the Arabian gulf region, with observations on the identification and phylogeny of the fish-killing dinoflagellate Cochlodinium polykrikoides*. Harmful Algae. 9(2):163–72.

[26] Moradi M. (2020). *Trend analysis and variations of sea surface temperature and chlorophyll-a in the Persian Gulf.* Marine Pollution Bulletin. 156.

[27] Moradi M, Moradi N. (2021). *Correlation between concentrations of chlorophyll-a and satellite derived climatic factors in the Persian Gulf*. Marine Pollution *Bulletin*. 16

INTERNATIONAL JOURNAL OF
COASTAL, OFFSHORE & ENVIRONMENTAL ENGINEERING IJCOE Vol.7/No. 2/Spring 2022 (11-23)

Available online at: www. Ijcoe.org

Science behind global sea level and sea level rise for global warming and polar ice-melt: myths and reality

Aftab Alam Khan

[1] *Professor & Head, Oceanography and Hydrography, BSMR Maritime University, Dhaka, Bangladesh, khan.aftab13@gmail.com*

ARTICLE INFO

Article History:
Received: 06 Jan. 2022
Accepted: 10 May. 2022

Keywords:
Sea level rise
Global warming;
Thermal expansion
Ice-melt
Centrifugal force

ABSTRACT

Global sea level rise of 1.5 meter by 2100 AD due to global warming and polar ice-melt has emerged as a concept and not a science. Ocean thermal expansion responsible for sea level rise has also emerged as a myth. Warming of ocean surface can produce water vapor by evaporation which is not the volumetric expansion of ocean water to raise sea level. More the thermal heating of the ocean surface water more will be the evaporation from the ocean that negates volumetric expansion of the ocean water. Global warming can alleviate ocean temperature not to expand ocean water. Global scale ocean temperature measures 28ºC upto the depth of 40 m only. Below this depth temperature drastically decreases almost to 6ºC at 1000 m depth trending further decrease. Science behind melting of the polar floating ice-blocks supports reoccupation of the same occupied volume of the floating ice without sea level rise. Ice-melting further reduces load from the crust of the Earth to elastically rebound for attaining isostatic equilibrium preventing sea level rise. Paleo-sea level markers in the sediment deposits occur due to the crustal subsidence and uplift for transgression and regression respectively. Prograding delta can result in apparent sea-level drop showing retreat of the sea. Geophysical spheroidal shape of the earth with equatorial bulge and polar flattening maintain a perfect hydrostatic equilibrium condition. Maximum centrifugal force and minimum gravity attraction can allow sea level to occur at about 21 km higher in the equatorial region than in the polar region preventing sea-level fluctuation.

1. Introduction

Fifth Assessment Report of the Intergovernmental Panel on Climate Change (IPCC) claims sea level rise by 2100 AD due to fossil fuel burning, global warming and polar ice melt (IPCC, 2013; Church et al., 2013)[1,2]. According to Church and White (2006)3 and Jevrejeva et al (2009)[4], greenhouse gas emission from fossil fuel burning is the main reason for sea level rise that links to the global warming concept. Graph that stormed the world about climate change goes to the publication by Mann, et al (1998)[5] published in the journal Nature (Fig. 1a). However, the graph is proved to be wrong and subsequent update by the authors came in 1999. The temperature graph of Mann, et al (1998)[5] very clear that did not account the record of the medieval warm period and the little ice age shown in the Figure 1b. Removal of medieval warm period and an adjustment of little ice age resulted in the construction of global temperature curve of the last 900 years that shows a distinct cooling trend and abrupt rise in temperature in the last 100 years resembling a 'hockey stick' (Fig. 1a). Three observations are very clear in the temperature anomaly curve (Fig. 1a), a) the 'hockey stick' shape graph of abrupt linear rise in temperature after 1980; b) the absence of global temperature record representing 'Medieval Warm Period' and 'Little Ice Age'; and, c) distinct difference in the pattern of the temperature anomaly curve between year-by-year data from tree rings, corals, ice cores, historical records and year-by-year data from thermometers. In reality, temperature of the present global warming shows lower than the temperature medieval warm period that proves no relation of fossil fuel burning, global warming, thermal expansion and sea level rise. Ocean thermal expansion hypothesis has also been brought out to induce an arbitrary volumetric expansion of the ocean water for global sea level rise (IPCC, 2013)[1]. But, Lombard et al (2005)[6] opined that thermal expansion of the ocean water has declined in recent

time due to increased melting of land ice. New ocean temperature data-sets suggests that out of 1.8 mm/year apparently observed sea level rise, thermal expansion contributes only about 0.4 mm/year (Lombard et al., 2006)[7]. The Paris climate conference (COP21) in December 2015 opined that the current global average temperature is 0.85ºC higher than the late 19th century. Paleo-temperature data of 1000 years before present suggest that present global temperature is not more than the temperature of "medieval warm period" (Fig. 1b).

warming, ice-melt and sea-level rise. According to IPCC, sea level is estimated to rise 1.5 metre by 2100, if the countries are not able to restrict CO_2 emission 2ºC "well below" pre-industrial levels as stated in the 2015 Paris climate agreement (according to a new report by the Intergovernmental Panel on Climate Change (IPCC) on September 25, 2019). Global mean sea level (GMSL) from tide gauges and altimeter observations increased from 1.4 mm/yr over the period 1901–1990 to 3.6 mm/yr over the period 2006–2015. Present study is aimed at to find out the science

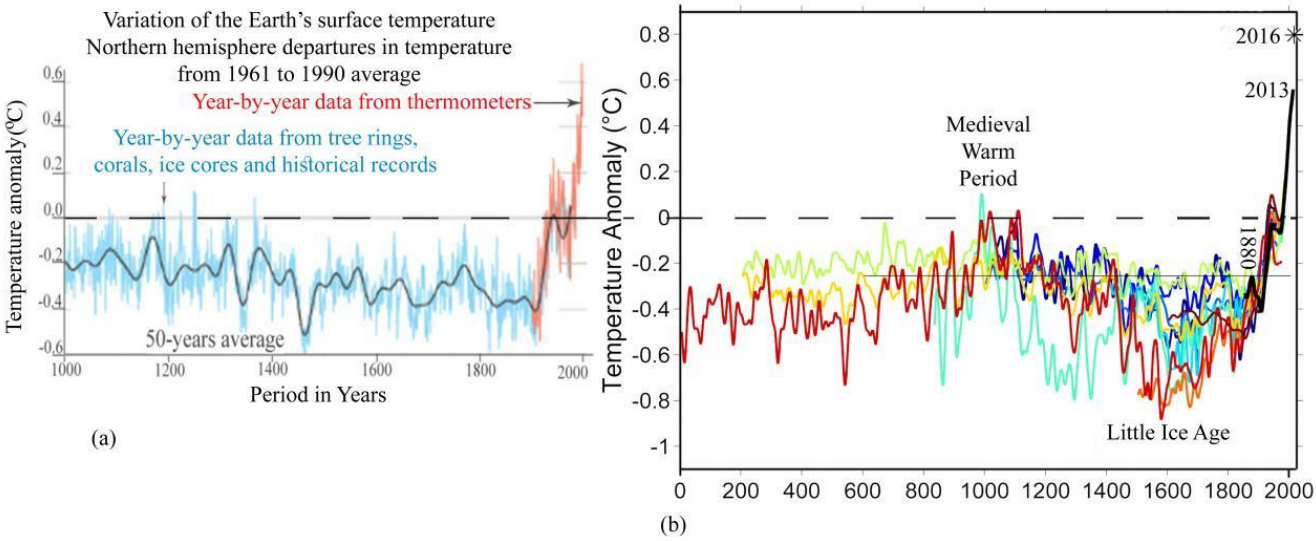

Figure 1. (a) The fake global temperature curve known as 'hockey stick' graph of proxy temperature data from tree rings, lake sediments and ice cores. (b) Global temperature curve that recorded medieval warm 900 years back and little ice age 400 years back. Graph in (a) is posted at the web site below: https://www.theguardian.com/environment/2010/feb/02/hockey-stick-graph-climate-change. Source of the graph in (b) is from the web site below prepared by Robert A. Rohde, the lead scientist for Berkeley Earth, from publicly available data and is incorporated into the Global Warming Art project. https://commons.wikimedia.org/wiki/File:Holocene_Temperature_Variations.png

Definition of sea-level change states a sea-level change observed with respect to a land-based reference frame. Since, high tide and low tide situation in every twelve hours also measures sea-level change with respect to the land-based reference frame cannot be defined as sea-level change. Hence, sea-level change by rise with respect to the land-based reference frame would occur when land-based reference frame will move downward, and/or sea-level change by fall when land-based reference frame will move upward. The upward or downward movement of the reference frame is possible only when continental crust and oceanic crust will move ups and down. According to Bindoff et al (2007)[8] decade-long satellite altimetry data show that since 1993 sea level has been rising at a rate of around 3 mm/yr. But this measurement has failed to correct data of slow progressive subsidence and uplift of the crust. Global warming phenomenon is linked to the sea-level rise due to polar ice-melting. Fossil fuel burning has been recognized as the culprit for global

behind the existing claim of global sea level rise. Further, it is intended to find out that the reality of the claims put forward in favor of rising sea level to issue an alarm of massive submergence of the coastal region of the littoral countries of the world in addition to the large volume of coastal population migration.

2. Materials and Methods

Present study is focused on the geophysical properties of the earth such as spheroidal shape, motion both spinning and rotation, centrifugal force, gravity field and hydrostatic level of the earth. Two third earth's surface is occupied by the ocean that maintains hydrostatic level uniquely coinciding with the spheroidal surface of the earth. Spheroidal mathematical surface is derived from the physical surface of the earth removing materials from elevated region above mean sea level and filling the same in the ocean basin. The spheroidal surface always coincides with the global mean sea level (Fig. 2a). Hence, sea-level rise and/or sea-level drop should be

expressed with respect to the spheroidal surface. This is possible when continental crust and oceanic crust moves with respect to each other and shows a measurable displacement (Fig. 2b).

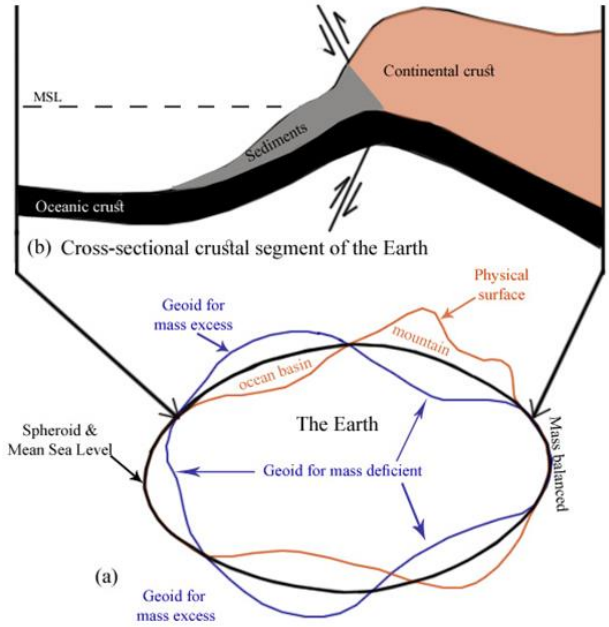

Figure 2. (a) Cartoon display shape of the earth wherein physical surface (brown line) represent ocean basin and mountain with respect to the mean sea level. Materials removed from mountain and filling ocean basin can form a mathematical spheroidal surface coinciding with the mean sea level (black line). Geoid (blue line) is an undulating surface depends on the distribution of mass in the ocean basin.
(b) Cross-sectional view of the crustal segment marked by arrow shows geological positions of the oceanic crust, basin and the continental crust. Sea level change is possible with the relative motion of the crust.

This is a geological process causing earth's crust to move continuously at a very slow rate to cause an apparent sea level change. In reality, sea level does not change rather maintains a hydrostatic equilibrium condition. Sea level observation by satellite altimetry of NASA measures sea surface height (SSH) at a given location, or sea level with respect to the surface of geoid, wherein sea surface always maintains a hydrostatic equilibrium coinciding with the spheroidal surface of the earth. In contrary, geoid is an undulating imaginary surface that occurs above the mean sea level where mass in the ocean basin is excess and occurs below the mean sea level where mass in the ocean basin is deficient (Fig. 2a). Hence, a fluctuating surface cannot be a reference level for the measurement of sea level change. Geoid surface fluctuates with respect to the equipotential surface (mean sea level) which coincides with the spheroidal surface. But for the SSH anomaly is the difference between a fixed satellite altitude and the 'range', which is an undulating sea surface. On the other hand, geoid moves up the mean sea level when internal mass of the ocean basin is excess, while, it goes below the mean sea level when internal mass of the ocean basin is deficient. Hence, under the above conditions determination of 'SSH anomaly' is an anomalous one. One of the most common methods is the tide gauge measurement for observing sea level changes. However, when tide gauges are linked with geographic positioning system (GPS) that records land movements simply cannot differentiate between sea level change and crustal motion. According to Rovere et al (2016)[9] tide gauge has three main disadvantages: (i) uneven distribution globally (Julia Pfeffer and Allemand, 2015)[10]; (ii) missing data associated with sea level signal (Hay et al., 2015)[11]; and (iii) double standard data sets accounting for ocean dynamic changes and land movements (Rovere et al., 2016)[9]. Spheroidal shape of the Earth is attained mainly due to the Earth's spinning on its own axis and the rotation around the Sun. Both the motions i.e., spinning and rotation, caused fluid surface of the ocean covering two third area of the earth to bulge out around the equatorial belt and to flatten around the pole due to the maximum centrifugal force and minimum gravitational attraction along the equator and zero centrifugal force and maximum gravitational attraction in the pole respectively (Fig. 3a). Distribution of centrifugal force and the gravitational attraction between equator and pole associated with angular momentum of the earth is shown in the Figure 3b that maintains an equilibrium position of the hydrostatic level. Because of the spinning, gravitational acceleration of the earth is less at the equator than at the poles. Difference of 0.0178 m/s^2 gravitational acceleration between the pole and the equator signify that the equator is about 21 km away from the center of gravity of the earth than at the poles. Equatorial and polar radius of the earth is 6378 km and 6357 km respectively measured based on the seismic velocity gives a difference of 21 km.

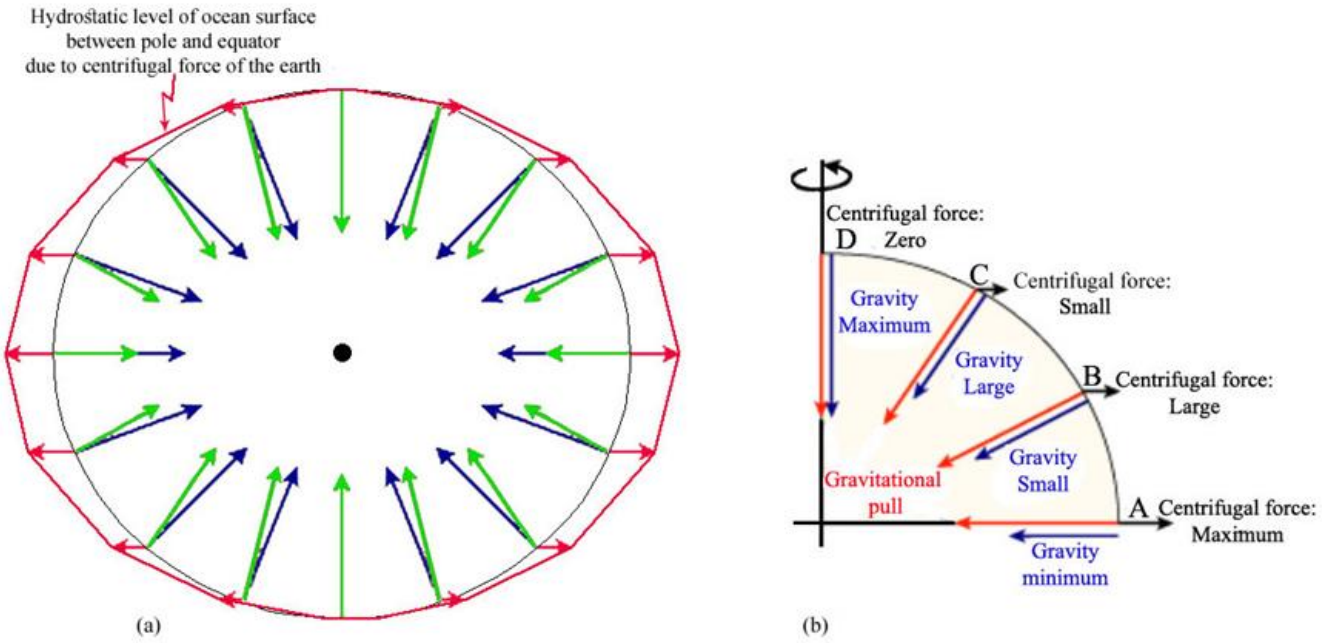

Figure 3. (a) The shape of a sphere by pulling the mass of the earth close to the center of gravity. Blue arrows point from Earth's surface toward its center. Their lengths represent local gravitational field strength. (b) Gravity is strongest at the poles because they are closest to the center of mass. This difference is enhanced by the increasing density toward the center. Red arrows show the direction and magnitude of the centrifugal force. At the equator, it is large and straight up. Near the poles, it is small and nearly horizontal. Vector addition of the blue and red arrows gives the net result of gravity plus centrifugal effect. This is shown by the green arrows in (a). Rotation of the earth produces more centrifugal force at the equator, less as latitude increases, and zero at pole shown in (b).

Difference in equatorial and polar radii signify that the earth is of spheroidal shape having equatorial bulging and polar flatting. Fluid mass of a disc under spinning and rotation can form a shape of an oblate due to maximum outward vector along its major axis and zero outward vector along its minor axis. Earth's equatorial plane where centrifugal force is maximum and gravity attraction minimum can bulge the ocean surface such that its external form is an equipotential of its own attraction and the potential of the centripetal acceleration. Further, water in volume from the polar region in all time cannot flow towards equatorial region since the surface of the equatorial region is 21 km more elevated than the polar region and horizontal gravity gradient is directed to both the poles. The average water surface level of high tide and low tide in a coastal belt is defined as the mean sea level and zero reference surface. Mean sea surface conforms to the earth's spheroidal surface. Since geoid surface fluctuates in accordance with the distribution of the earth's internal mass distribution, the measurement of sea level change with respect to the geoid surface is erroneous.

Water level in the oceans can rise and fall not due to the addition and removal of water rather due to the uplift and subsidence of the crustal block in the continental margin. Formation of the oceans can initiate the formation of the continental margin both as the converging and the diverging plate margins. The continental margin is the junction between the continental crust and the oceanic crust (Fig. 4). Since, continental break and continental drift away from each other is responsible for the opening and the formation of the oceans, zero elevation sea-level occur on to the continental margin. With the progressive sedimentation the continental margin is covered by the influx of sediments developing continental shelf and slope.

There are four different scenario of fault movements two in the converging and two in the diverging plate margin those control the status of sea-level.
Case 1 and 4 exhibit an uplift of the continent and subsidence of the ocean basin resulting in sea-level drop.
Case 2 and 3 exhibit a subsidence of the continent and uplift of the ocean basin resulting in sea-level rise.

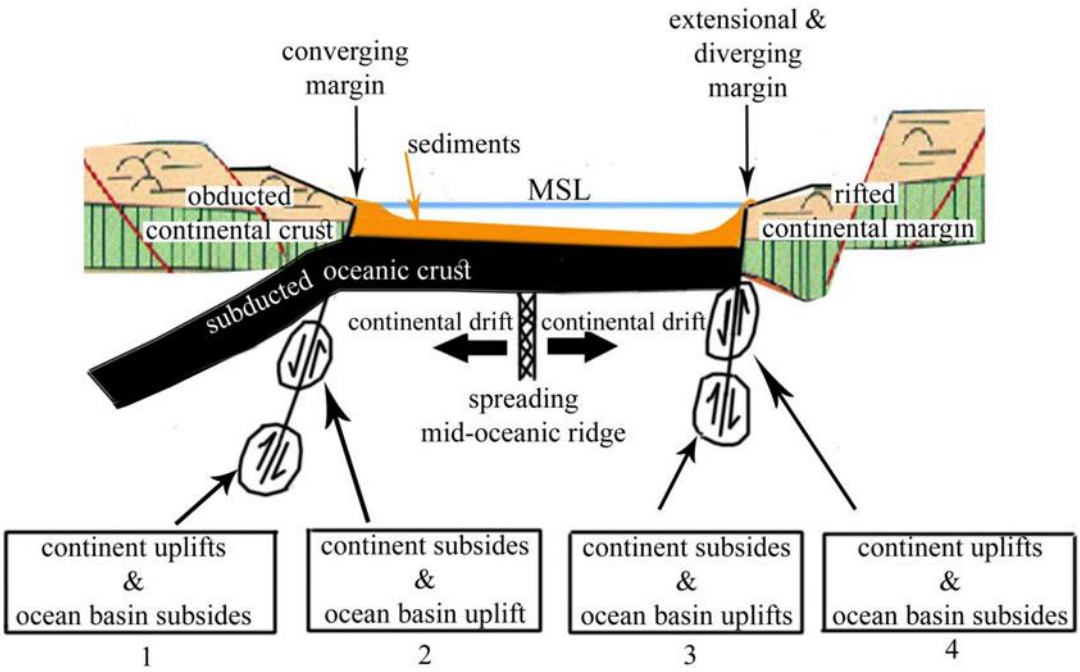

Figure 4. Model representing drifted continents, formation of an ocean by sea floor spreading from mid-oceanic ridge underlain by oceanic crust, and plate margins associated with various types of faults for crustal movement in order to signify apparent sea-level rise and fall.

On the other hand, global sea-level always maintains a hydrostatic equilibrium condition of equipotential surface. So, we call sea-level rise when sea enters the coastal belt and sea-level fall when sea moves away from the coastal belt. The entrance and exit of sea is directly linked to the fault movement of the continental and oceanic crust. Figure 4 explains very clearly the fault mechanism for determining the status of sea-level. There exists a definite fault margin between the continental crust and newly formed ocean basin underlain by the oceanic crust. These faults can occur in the both converging and diverging plate margins. In both the margins, sea-level can either enter inside the continental block or it can retreat from the continental block without causing sea level rise or sea level drop, and maintains an unique hydrostatic equilibrium level. When continental crust moves down (subsidence) with respect to the oceanic crust, sea-level can enter inside the continent, in contrary, when oceanic crust moves down with respect to the continental crust, sea-level can retreat from the continent. When both continental and oceanic crust move simultaneously (geologically non-existence) either by subsidence or by uplift, sea (level) may enter inside the continental block or retreat from the continental block without causing actual sea level rise or sea level drop respectively. It is essential to consider: a) crustal movement as above may occur in a very small coastal region of the earth surface measuring only few square kilometers, b) ocean occupies more than 170 million square kilometers surface area of the earth. So volumetric displacement of ocean water either for subsidence or by uplift will not cause any detectable sea level change. Similarly, neither sea transgression is a sea level rise, nor sea regression is a sea level drop.

3. Science behind Mean Sea Level

In view of the fact that the spheroidal surface of the earth is a mathematical surface, while, global mean sea level is a physical surface of the earth that always coincides. Further, the mathematical surface is calculated based on the theoretical gravity values of the earth at all points is known as the reference spheroid. It is related to the mean sea-level (MSL) determined from the average values of high tide and low tide conditions equivalent to a surface made by removing excess mass of the land to fill the ocean depressions. The force of gravity (g_z) or the plumb line on an equipotential surface is everywhere normal directed to the center of the earth. Based on the calculations of gravity using formula (equation 1 below) of the International Association of Geodesy, the mathematical spheroidal surface of the earth is determined (Telford et al., 1976)[12]. The formula expresses 'g' value at any point on the latitude as:

$$g = g_o(1 + \alpha \sin 2\phi + \beta \sin 2 2\phi) \qquad (1)$$

where g_o = equatorial gravity = 978.0318 Gals, ϕ = latitude, and the constants α and β are equals 0.005324 and -0.0000058 respectively.

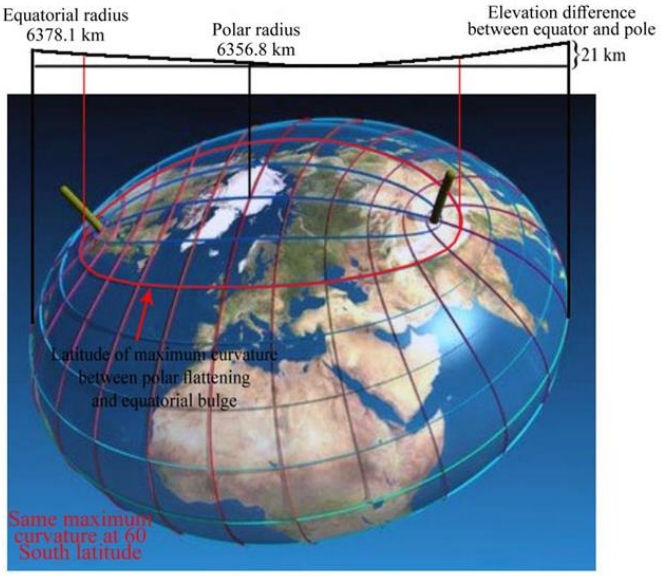

Figure 5. Projection of polar and equatorial radius on to the horizontal plane shows elevation difference 21 km between equator and pole with higher at the equator. Maximum curvature of the spheroidal surface of the Earth coincides approximately with 60°N latitude preventing bulk water movement across 60°N latitude from Arctic. Similarly, floating ice from Antarctica can freely move upto 60°S latitude where spheroidal surface has maximum curvature.

The value of gravity thus determined by this relation is the measure of the values at the sea level that coincides with spheroidal surface of the earth. The spheroidal surface is characterized by the gravity attraction at the equator equal 978.0318 Gals and at the poles equal 983.3318 Gals. The difference of gravity between the poles and the equator is 5.3 Gals (5300 milliGals) more at the poles. Thus, the gravity field around the earth can represent an equatorial bulge of minimum gravity attraction and polar flattening of maximum gravity attraction. Equatorial bulge is attributed to the volumetric expansion due to lower density and and lower gravity attraction at the equator, while, polar flattening is attributed to the volumetric contraction at the poles due to higher density and maximum gravity at the poles.

Horizontal gravity gradient (component of g_z) is also significantly less in the equatorial region which can prevent sea water to move to the equatorial region from the higher latitudes. On the otherhand maximum curvature of the earth at around 60°N and 60°S latitudes and the occurrence of equatorial surface at about 21 km higher elevation than the polar region can definitely prevent ocean water movement and circulation (Fig. 5). The spheroidal shape of the earth depends on: (i) greater gravity attraction of the polar region for polar flattening and lesser gravity attraction of the equatorial region for equatorial bulging, and, (ii) the centrifugal force of earth's spinning and rotation. The centrifugal force causes the mass (ocean water) to move away from the earth located at the equatorial region. The outward normal of the centrifugal force acts on the surface of the ocean-fluid surface is maximum at the equator and zero at the poles (Fig. 3b). It is the centrifugal force due to the Earth's spin and rotation cause polar flattening and equatorial bulge. The polar flattening ratio (eccentricity) of 1/298 implies that sea-level at the equator occurs about 21 km higher than at the poles. Ocean water surface would occur in equilibrium hydrostatic level which is curvilinear, and this level is influenced by the gravity as well as centrifugal force of the earth. Centrifugal force acts on water of the oceans more than it does on the solid Earth. Any addition of water to the ocean water cannot flow up the hill towards equator from the poles to cause global sea level rise. Hence, although ocean water at the equator makes a level difference of 21 km higher than at the poles, it is the centrifugal force maximum at the equator and zero at the poles restricts ocean water to move down-hill toward poles. Shape of the earth established from geodetic measurements and more recently by satellite tracking, is practically spheroidal, bulging at the equator and flattened at the poles, such that the difference between equatorial 'a' and polar 'b' radii, divided by the former 'a', is 1/298. This ratio is known as the polar flattening ratio. The surface of the theoretical shape is the surface of the centripetal acceleration which is equivalent to an equipotential surface of gravity field. Centripetal acceleration is the rate of change of tangential velocity. The direction of the centripetal acceleration is always inwards of an object along the radius vector of the circular motion. The magnitude of the centripetal acceleration is related to the tangential speed and angular velocity. In general, a particle moving in a circle experiences accelerations both angular and centripetal velocity. The circumference of the Earth along the equator (equatorial circumference) is 40,075 km and along longitude (polar circumference) is 40,008 km. Difference of 67 km also larger at the equator than at the pole which poses an upward gradient 1 in 149.28 (equivalent 0.602°) towards equator. Hence, an upward slope directed to the equatorial region and downward slope directed to polar region makes conditions very clear for volumetric water circulation of the oceans. Inflection point of the curvature in the slope coincides with the spheroidal surface at around 60° latitudes. This makes higher level at the equator and lower level at the poles that prevents ocean-waters flowing to lower level from higher level.

4. Polar Ice Melt and the Sea Level Rise

Scenario of ice melting and ice growth alongwith ocean water response are different in two polar regions. Arctic Ocean in the north is surrounded by the land mass thus can restrict the movement of the

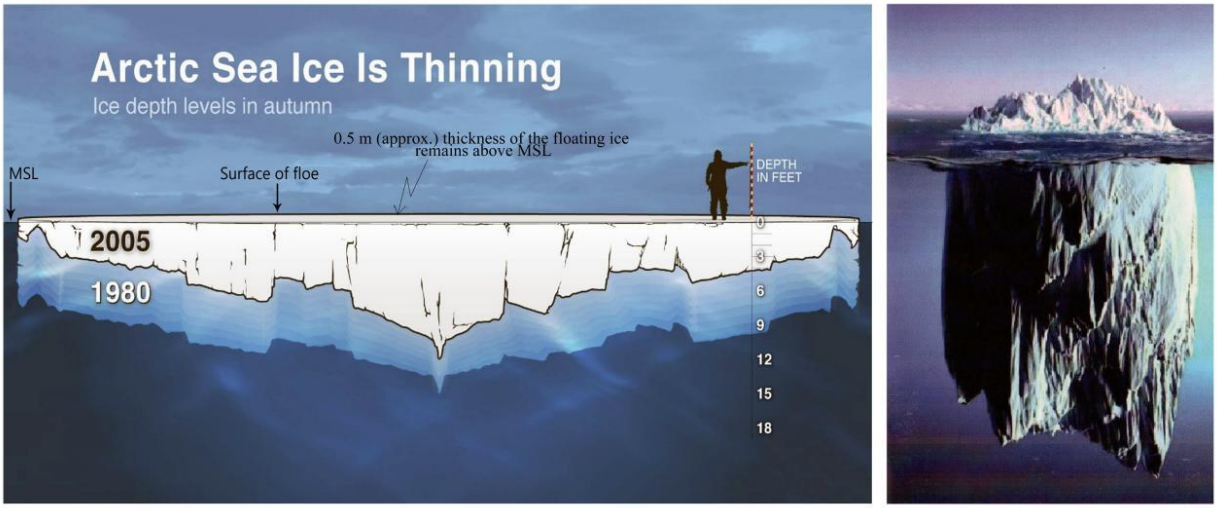

(a) (b)

Figure 6. (a) Profile shown here depict roughly what fraction of sea ice fell within different thickness ranges for the years shown, within the area of the Arctic Ocean where the Navy has declassified its soundings. Data provided by NASA scientist Ron Kwok, based on research Kwok, R. and Rothrock, D. A., (2009)[13]. Decline in Arctic sea ice thickness from submarine and ICESat records: 1958 - 2008. Geophysical Research Letters 36, L15501.
http://www.climatecentral.org/gallery/graphics/arctic_sea_ice_thinning_fall.
(b) Cartoon depict floating ice submerged in the ocean displacing more than 95% of water volume. On melting the same volume of ice would re-occupy the displaced volume of water without adding water to the surrounding ocean justifying no-sea level rise on ice melting.

floating ice, while, Antarctic in the south is surrounded by the open oceans thus can allow floating ice to move freely. Nonetheless, the movement of the floating ice is likely to be maximum up to 60ºS latitude where maximum curvature occurs (Fig. 5). Further, the attraction of gravity can play an important role to the flow of water which is always to the downward gravity. Similarly, water cannot flow from higher gravity to lower gravity wherein higher gravity of the polar region would attract water from moving towards equatorial region. This condition would necessarily make ocean water static at every 'g_z' position directed to the centre of gravity of the earth. Since, greater horizontal gravity gradient is toward poles that would also help melt-water to remain attracted towards polar region. Polar flattening and equatorial bulge both are intrinsically related to the maximum curvature of the Earth's spheroidal surface that occur between 45ºN and 60ºN latitudes in the northern hemisphere and, 45ºS and 60ºS latitudes in the southern hemisphere. In reference to the mapping of geoid height between 60ºN and 60ºS it is inferred that the maximum curvature of the spheroidal surface occurs between 60ºN and 60ºS (Dobrin, 1976)[14]. Hence, ice-melt water from polar region cannot flow beyond 60ºN and 60ºS. Sea-level can rise due to ice melting if the melt water is added to the ocean water. But in reality, ice-melt water does not add to the ocean water rather only replaces the entire volume of the submerged ice on melting. Further, freezing volume generally is larger than the volume of the same quantity of water on melting. So, floating and submerged ice blocks when melt, it can reoccupy more volume than the volume it does. Hence, on melting the ice block can easily replace the occupied volume without adding extra melt to the ocean water. Simple scientific analogy confirms that floating ice-blocks that occupy volume of the displaced water will re-occupy same volume on melting without adding water to the surrounding oceans (Fig. 6).

According to an article "Third dimension: new tools for sea ice thickness", it is revealed that the average thickness of sea-ice in the Arctic Ocean is about 3 m. This measurement was performed between March 29, 2015 to April 25, 2015 by the Center for Polar Observation and Modeling, UCL London (Lindsay and Schweiger, 2015)[15]. http://nsidc.ogr/arcticseaicenews/2015/05/newtools-for-sea-ice-thickness. The month of April ice extent for 1979 to 2015 shows a decline of 2. 4% per decade relative to the 1981 to 2010 average. A decline in the ice extent between 1979 and 2015 is about 1,208,000 km2 in its areal extent. But, overall ice extent decreased to about 862,000 km^2. Lindsay and Schweiger (2015)[15] found that ice thickness over the central Arctic Ocean has declined. Reduction of ice thickness in the central Arctic Ocean from an average of 3.59 m to 1.25 m during 1975 to 2012, a reduction of 65%, is observed.

In April 2015, Arctic sea-ice covered about 14,000,000 km^2. An average of 3m thickness of the floating ice and the maximum areal extent of Arctic floating-ice about 14,500,000 km^2 can occupy volume equivalent to 43,500 km^3. Areal extent of the floating ice is reduced to 7,000,000 km^2 equivalent to 17,500 km3 volumetric space at the end of summer-melt

season. Hence, out of total 39,000 km^3 of floating ice in the Arctic Ocean, about 31000 km^3 ice-melt would occupy same volume of the displaced water by the submerged ice-sheets and no-sea-level rise occurred. Khan (2019)[16] calculated an equivalent volumetric quantity of 65% thickness reduction of ice sheets in the Arctic Sea over the period 1975 to 2012 and opined that more than 2,500,000 km^3 in volume of ice-melt water must have been added to the ocean water by now over an area more than 14,500,000 km^2 in the central Arctic Ocean. The added water, by now, should have raised sea level in the Arctic Sea more than 178 mm which is much much greater than what IPCC has claimed. However, until now (as of April 2021) there is no record of such sea level rise, not even 66 mm at the rate of 3 mm/yr predicted by IPCC 22 years ago.

5. Isostasy and the Sea Level

Ice melting from oceanic heat flux decreases faster than the ice growth in the weakly stratified Southern Ocean, leading to an increase in the net ice production and hence an increase in ice mass.

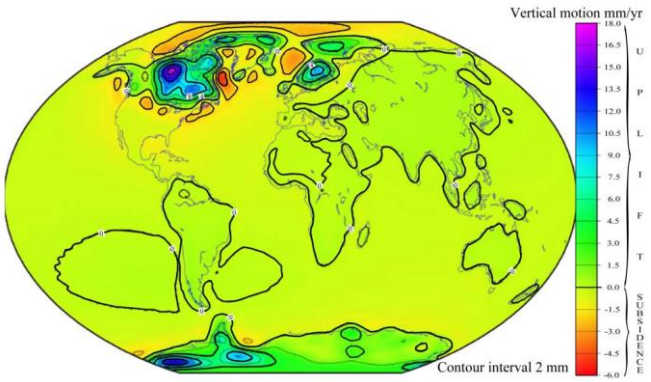

Figure 7. Crustal isostatic balancing (modified from https://commons.wikimedia.org/wiki/File:PGR_Paulson2007_Rate_of_Lithospheric_Uplift_due_to_PGR.png . Both Arctic and Antarctic polar region exhibit significant vertical motion in terms of uplift and subsidence. Uplift term is much greater than subsidence represented by color code. Because of the greater uplift than subsidence polar region never shows sea level rise. Both Arctic and Antarctic polar region are isostatically unbalanced while all the lower latitudes areas are relatively balanced isostatically (source: Erik Ivins, 2010 of NASA's Jet Propulsion Laboratory in Pasadena, California USA alongwith his article entitled "Rate of lithospheric uplift due to Postglacial Rebound", posted in the website https://en.wikipedia.org/wiki/ Post-glacial_rebound.

Both the polar region exhibit reduction in ice-load in the crust due to melting and removal of ice-cover from the continental blocks every year. Reduction in weight of the continent can activate isostatic mechanism and continent uplifts to maintain isostatic equilibrium and prevents sea level rise. Figure 7 exhibits vertical motion of the crust in the two polar region applying glacial isostatic adjustment (GIA) theory prepared by Erik Ivins, 2010 of NASA's Jet Propulsion Laboratory in Pasadena, California USA alongwith his article entitled "Rate of lithospheric uplift due to Postglacial Rebound", posted in the website https://en.wikipedia.org/wiki/Post-glacial_rebound. The map (Fig. 7) showing vertical motion of the crust is based on the work by Paulson et al (2007)[17].

According to Khan (2019)[16], quote "both the polar region exhibit noticeable uplift and subsidence of the crust in order to attain its isostatic equilibrium. In the north polar region, crust is characterized by the maximum 18 mm/yr uplift surrounded by the region of maximum 6mm/yr subsidence. Difference of 12 mm/yr is attributed for the uplift that should result in an apparent sea-level drop. In reality, it is not a sea level drop rather sea moves away from the continent exposing the land, while sea will move inside the continent submerging land when continent will subside due to the over-burden load of the the growing ice cover in yearly basis. In the south polar region, Antarctica shows maximum uplift 12 mm/yr and maximum subsidence 2 mm/yr with a difference of 10 mm/yr assigned to uplift that would also result in an apparent sea-level drop means regression of sea from the continent. Reverse would occur due to the overburden load for ice growth over the continent. There are good number of publications about the post glacial isostatic rebound of the polar region", unquote.

6. Thermal Expansion and the Sea Level Rise

During the winter, area up to 18,000,000 km^2 of ocean is covered by sea-ice, but by the end of summer it is reduced to about 3,000,000 km^2. Hence, about 23,000 km^3 sea-ice of Antarctica can freely float northward into the warmer water where it eventually melts every year without showing any sea level rise in the lower latitudes. Further, melting of such a huge volume of floating sea-ice of Antarctica not only can reoccupy volume of the displaced water but also can cool ocean-water in the lower latitudes of the southern oceans preventing so-called sea level rise due to thermal expansion. Further, thermal expansion of the ocean surface water is never a volumetric expansion of the ocean water which is suggested for sea level rise. According to Zhang (2007)[18] thermal expansion in the lower latitude is unlikely because of the reduced salt rejection and upper-ocean density. Enhanced thermohaline stratification tend to suppress convective

overturning leading to decrease ocean heat transport in the upward ocean. Ocean temperature measures 28ºC upto only 40 m depth. Below this depth temperature drastically decreases almost to 6ºC at 1000 m depth trending further decrease. Atmospheric temperature rise may heat the surface of the ocean water that only develops ocean water circulation and evaporation not a thermal / volumetric expansion of the ocean water. Due to warming of surface water of the ocean density may decrease and the cold water from below is up-welled and a surface circulation can start. According to the IPCC executive summary of sea level rise in chapter 09 it is admitted that the observational data are scant, both in time and space (Barnett, 1985)[19]. Further, the inter-annual variability creates too much noise to cause error in the estimation.

The ocean currents are generated from the forces acting upon the water such as earth's rotation, wind, temperature, salinity difference and gravitation. Depth contours, shoreline configurations, and interactions with other currents influence a current's direction, amplitude and strength. Ocean currents are primarily horizontal water movements known as 'wind wave'. At Calm Ocean with no or little wind wave amplitude of the current is much less than at the condition of storm generated 'wind wave'. Sea surface height (SSH) measurements would be different at two conditions. This may lead to wrong estimate of sea level condition. Sea level does not rise due to thermal expansion of the ocean water as there is no real thermal expansion due to global warming. Temperature of sea water has no direct impact on sea-level. According to Hegerl, et al (2007)[20] of IPCC Fourth Assessment Report, it is clearly expressed quote, "*consistency with surface air temperature alone does not guarantee a realistic simulation of thermal expansion, as there may be compensating errors among climate sensitivity, ocean heat uptake and radiative forcing*", unquote.

7. Geological Factors and the Sea level

Geologically, global (eustatic) sea level change is not possible. In order to have eustatic sea level change the entire oceanic crust that makes the floor of all the oceans need to subside or uplift uniformly at the same time. According to Kemp et al (2015)[21] "land uplift or subsidence" can result in, respectively, a fall or rise in sea level that cannot be considered eustatic as the volume or mass of water does not change. There are numerous geological factors and processes that can change ocean floor configuration nonetheless tectonism, volcanism, visco-elastic deformation, trench-slope deposits, sub-marine fan deposits and prograding delta system are the most important. However, these factors and processes do not occur simultaneously everywhere around the earth and hence no impact on the volume change of the ocean basin occur for sea level change. In case of prograding delta with high sedimentation rate, an overlap condition on to the contact margin of the continental and oceanic crust, the scenario of sea level change is different. A variety of processes drive configuration-change of the ocean floor, and not the ocean surface, resulting in distinct spatial patterns at local to regional scale by transgressions and regressions of the sea but the hydrostatic level of the ocean water remains unchanged. Palaeo-sea level changes have been identified from the geological records wherein data from the Late Triassic (≈227 Ma) until the present time are reasonably well documented but not the amplitude of the eustatic changes of the sea level. Eustatic change may occur when the sea level changes due to an alteration in the volume of water in the entire oceans or, alternatively, a change in the shape of the entire ocean basins and hence a change in the amount of water the entire oceans can hold. Eustatic change is always a global effect and only approximations (Vail et al., 1977)[22].

The Phanerozoic history of North America from the Late Triassic or Early Jurassic, corresponds to the Pangea breakup phase, during which North America drifted westwards. The eastern continental margin became the modern extensional Atlantic margin basins, while the western margin underwent tectonism and accretionary prism development leading to the assembly of the Cordilleran orogen. Similar extensional basins and sedimentary accretionary prism leading to orogens developed along the eastern margin of the Atlantic Ocean in Africa and Europe, and in some region of Asia. These mega events of the earth led to major sea-level rise and fall in terms of tens to hundreds of meters as oceans have undergone regional transgressions and regressions. Hence, transgressions occur when a region undergoes major subsidence of the continental crust or uplift of the oceanic crust can cause sea to enter inside the continent showing relative sea level (RSL) rise with respect to the existing sea level. Example of mid-Holocene (about 8000 years ago) subsidence in the Bengal Basin floor of continental crust caused a major marine transgression to signify sea level rise to the tune of more than 10m (Khan et al., 2000)[23]. Similarly, regressions can occur when continental crust uplifts and oceanic crust subsides. Geological processes are responsible of two types of major crustal movements viz., uplift and subsidence. Relation of such crustal movement with respect to the global and regional sea level is explained in the Figure 4. Mörner (2020)[24] recorded relative sea level drop from Holocene until the Recent at Ouvéa Island in New Caledonia and documented distinct two terraces representing paleo-shores at +22m high and +4m high respectively (Fig. 8).

Figure 8. The spectacular Lekiny sea cliff on Ouvéa Island including 3 distinct sea levels: an upper +22 m shore, a huge under-cut shore with rock-cut platform at +4 m, and Holocene to present under-cut shore. Picture taken at high-tide level on November 2018 (Source: Mörner, 2020)[24].

Both the paleo-shores show distinct tidal under-cut terraces representing the Holocene Interglacial period terraces graded to present sea level. This documentation could be a unique example of land uplift and sea subsidence for relative sea level drop. Oceans maintain hydrostatic equilibrium level without truly sea level change in every geological events. Prograding delta system in the coastal region and other geological events may cause local/relative sea-level fall as new sedimentary deposition advances as accretion pushing sea further down the coast irrespective of global warming and polar ice-melt. Hence, both regional and local apparent sea-level rise and fall is related to the geological events and not related to global warming and polar ice melt.

8. Examples of Sea Level of the Littoral Countries

Mörner (2019a)[25] observed geomorphological facts from Maldives, Goa and Bangladesh in the Indian Ocean and from Fiji and New Caledonia in the Pacific Ocean to record sea level condition and found it to be stable since the last 50-70 years. He further observed a very clear and distinct rock-cut platform on Ouvéa Island leveled at +70 cm above the present high tide level (HTL). The platform is fresh and un-weathered and cut into the older strongly weathered reef masses that evident definite relative sea level drop (Fig. 9a). In the coast north of Saint Joseph on Ouvéa Island of New Caledonia it is found that the tidal washing limit has moved 2m seaward and about 5 cm down. The new coastal zone is now in the process of becoming over-grown. This lends support that sea level is not rising on Ouvéa Island (Fig. 9b; Mörner, 2018)[26]. Bangladesh coast to the west at Kotka, trees reveal that the tree trunks have horizontal root systems hanging some 80 cm above the shore surface. Such root systems are found just below the mud surface indicating stable sea level despite strong erosion (Fig. 9c; Mörner, 2010)[27]. Landsat image of 1990 and 2019 depict the emerging of new islands of about 1500 sq km area in the coastal belt of Bangladesh proving major sea regression and extensive land accretion (Fig. 9d; present study). A common view of the shores of the atoll islands of the Maldives has been documented by Mörner (2019b)[28]. Figure 9e exhibits three distinct features: (a) a prominent notch from the sea level position prior to the 20 cm fall at about 1970, (b) the abandoned shore segment in the process of being overgrown by creepers, and (c) post-1970 at present, washing limit (Mörner, 2019b)[28]. Coastal morphology data of the last 400 years in the beach in Goa, India show three shore-lines representing three successive sea-level positions such as the present shore at +10.0 cm (red line), the pre-1960 shore at +20 cm (blue line), and the 17th century +60-cm shore (yellow line)(Fig. 9f). The dead cliff and double rock-cut platform is marked by white line. Loveson et al. (2014)[29] noted that the subsequent shoreline growth from 1957 to 2012 fits the present sea-level reconstruction perfectly well just before the 20-cm sea level fall at about 1960 (Mörner, 2017)[30]. The tide gauges in Mumbai, India as well as in Visakhapatnam, India show a sudden fall in the sea level from 1955 to 1962, followed by virtually stable sea-level conditions in the last 50 years. Coral mortality induced by the 2015–2016 El-Niño in Indonesia: the effect of rapid

sea level fall is shown in the Figure 9g (Ampou et al., 2017)[31]. In the late 20th century sea level fell killing many corals (the centre in the image) and forcing corals to grow as microatolls (Fig. 9h).

The coral died due to sea level drop dated younger than 1955 (red dot gives position of dated sample) and since then the coral has not been able to grow upwards due to stable sea level conditions forcing the coral to grow laterally into a microatoll. The limit for coral growth seems to be 40 cm below low tide level as measured at the site (Mörner, 2019b)[28]. Some of the most dramatic uplift is found in Iceland. Much of modern Finland is former seabed or archipelago that shows sea level immediately after the last ice age. Massive coral (Pavona clavus) exposed in 1954 by tectonic uplift in the Galapagos Islands, Ecuador. Beach ridges on the coast of Novaya Zemlya in arctic Russia. Such ridges are formed by pushing of sea ice as a result of Holocene glacio-isostatic rebound. A

9. Conclusions

Global sea level is continuously being maintained its hydrostatic level due to the Earth's angular momentum, spinning and rotation. Dominance of oceans and the maximum centrifugal force at the equatorial region between 30°N and 30°S caused the spheroidal shape of the Earth characterizing equatorial bulge and polar flatten along which global sea level is maintained hydrostatic equilibrium condition. Global mean sea level is an equipotential surface that fits uniquely with the spheroidal surface of the Earth. Hydrostatic equilibrium condition of the mean sea level is continuously being maintained by the centrifugal force and the orbital angular momentum of the Earth. Under such physical law, mean sea level will not change unless a change in the centrifugal force and orbital angular momentum occurs.

Global warming and the subsequent thermal expansion due to increased sea surface temperature shall not enhance sea level because thermal expansion

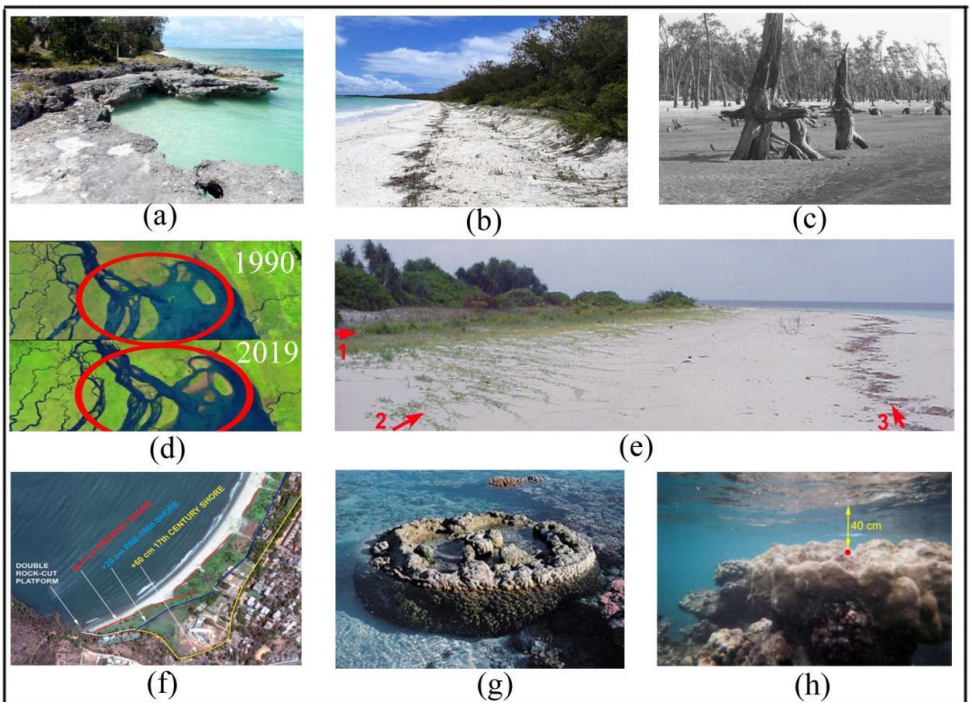

Figure 9. Examples of sea levels at different littoral countries. Explanation of each example is available in the text.

8000-year old-well off the coast of Israel now submerged is a land mark of crustal subsidence giving relative measure of sea level rise. The "City beneath the Sea" near the Port Alexandria on the Nile delta fits with the drowned well off the coast of Israel. Both subsided due to subduction-pull of the downgoing African crustal slab as it enters the Hellenic trench in the Mediterranean. Apparent sea level rise in Venice lagoon is due to the tectonic subsidence of the basin floor caused by subduction rollback of Adriatic slab wherein down-going crust causing subsidence of Venice rather than sea level rise.

does not apply to the entire water volume of the ocean and volumetric expansion of the ocean water is not possible by the rise in sea surface temperature (SST) except increased evaporation of the sea surface. An increased evaporation add more water vapor to the atmosphere that helps heat trapping to enhance global warming in turn forming intense rainfall, cyclone, storm surge, coastal flooding.

Polar ice melting due to global warming shall not contribute to the ocean water for sea level rise rather the entire submerged ice sheets on melting shall reoccupy the same displaced volume by the submerged ice sheets. Polar ice cover of Greenland and Scandinavia in the northern hemisphere and

Antarctica in the southern hemisphere on melting shall not cause sea level rise rather an apparent drop because of the isostatic rebound of the Earth's crust to attain isostatic equilibrium wherein the residual uplift is more than the residual subsidence. Higher gravity attraction of the poles and lower gravity attraction at the equator also play an important role in preventing bulk volume displacement of the ocean water.

Crustal uplift and subsidence shall allow sea water to enter inside the continent or retreat from the continent without showing an actual sea level rise or drop. Sea level marker are preserved in the deposited sediments that have undergone sedimentation in the marine environment of deposition in the ocean basin. Instead of sea level rise and fall, the terms such as "sea transgression for rise" and "sea regression for fall" should be used. All the littoral countries of the world are safe from sea level rise phantasy except the countries are situated in the active tectonic regime, especially in the active plate collision margin where continuous crustal deformation is progressing due to the plate subduction and obduction. Study revealed that no "sea-level rise" will occur to the littoral countries of the earth due to global warming and polar ice-melt.

10. Acknowledgement

Entire study is done by the sole author of this article. The work is not supported by any institute or organization. There is no conflict of interest since no organization or institute sponsored this study. I do acknowledge all the authors of all the published and unpublished papers used in this study and those have enlightened my ideas and views, and helped to enrich this article.

11. References

[1] IPCC Climate Change, 2013. The physical science basis. In: Stocker, T.F., Qin, D., Plattner, G.K., Tignor, M., Allen, S.K., Boschung, J., Nauels, A., Xia, Y., Bex, V., Midgley, P.M. (Eds.), Contribution of Working Group I to the Fifth Assessment Report of the IPCC. Cambridge University Press, Cambridge, United Kingdom and New York, NY, USA, 1535 pp.

[2] Church, J.A., Clark, P.U., Cazenave, A., Gregory, J., Jevrejeva, S., Levermann, A., Merrifield, M., Milne, G., Nerem, R., Nunn, P., Payne, A., Pfeffer, W., Stammer, D., Unnikrishnan, A., 2013. Sea level change. Climate change 2013: the physical science basis. In: Stocker, T.F., Qin, D., Plattner, G.K., Tignor, M., Allen, S.K., Boschung, J., Nauels, A., Xia, Y., Bex, V., Midgley, P.M. (Eds.), Contribution of Working Group I to the Fifth Assessment Report of the IPCC. Cambr. Univ. Press, Cambridge, pp. 1137-1216. https://doi.org/10.1017/CBO9781107415324.026.

[3] Church, J.A., White, N.J., 2006. A 20th century acceleration in global sea-level rise. Geophy. Res. Lets., 33 (1). https://doi.org/10.1029/2005GL024826. L01602.

[4] Jevrejeva, S., Grinsted, A., Moore, J.C., 2009. Anthropogenic forcing dominates sea level rise since 1850. Geophy. Res. Lets., 36, L20706.

[5] https://doi.org/10.1029/2009GL040216.

[6] Mann, M.E., Bradley, R.S., Hughes, M.K., 1998. Global-scale temperature patterns and climate forcing over the past six centuries. NATURE 392, 779-787.

[7] Lombard, A., Cazenave, A., Le Traon, P.Y., Ishii, M., 2005. Contribution of thermal expansion to present-day sea level rise revisited. Glob. Plane. Chan., 47, 1-16.

[8] Lombard, A., Cazenave, A., Le Traon, P.Y., Guinehut, S., Cabanes, C., 2006. Perspectives on present-day sea level change: a tribute to Christian le Provost. Ocean Dynamics 56 (5-6), 445-451. https://doi.org/10.1007/s10236-005-0046-x

[9] Bindoff, N.L., J. Willebrand, V. Artale, A, Cazenave, J. Gregory, S. Gulev, K. Hanawa, C. Le Quéré, S. Levitus, Y. Nojiri, C.K. Shum, L.D.Talley and A. Unnikrishnan, 2007: Observations: Oceanic Climate Change and Sea Level. In: Climate Change 2007: The Physical Science Basis. Contribution of Working Group I to the Fourth Assessment Report of the Intergovernmental Panel on Climate Change [Solomon, S., D. Qin, M. Manning, Z. Chen, M. Marquis, K.B. Averyt, M. Tignor and H.L. Miller (eds.)]. Cambridge Univ Press, Cambridge, United Kingdom and New York, NY, USA.

[10] Rovere, A., Stocchi, P., Vacchi, M., 2016. Eustatic and Relative Sea Level Changes. Cur. Clim. Change Rep. https://doi.org/10.1007/s40641-016-0045-7.

[11] Julia Pfeffer, J., Allemand, P., 2015. Contribution of vertical land motions to relative sea level variations: a global synthesis of multisatellite altimetry, tide gauge data and GPS measurements. Eart. Plane. Sci. Lets. 439, 39-47.

[12] Hay, C.C., Morrow, E., Kopp, R.E., Mitrovica, J.X., 2015. Probabilistic reanalysis of twentieth-century sea-level rise. NATURE 517, 481-484.

[13] Telford, W.M., Geldart, L.P., Sheriff, R.E., Keys, D.A., 1976. Applied Geophysics. Camb. Univ. Press, 860 pp

[14] Kwok, R. and Rothrock, D. A., 2009. Decline in Arctic sea ice thickness from submarine and ICESat records: 1958–2008. Geophys. Res. Lett., v. 36, L15501, doi:10.1029/2009GL039035

[15] Dobrin, M.B., 1976. Intro. Geophy. Pros., 3rd ed. McGraw-Hill, New York. 630pp.

[16] Lindsay, R., Schweiger, A., 2015. Arctic sea ice thickness loss determined using subsurface, aircraft, and satellite observations. The

Cryosphere 9, 269-283. https://doi.org/10.5194/tc-9-269-2015.

[17] Khan, A.A., 2019. Why would sea-level rise for global warming and polar ice-melt?. Geoscience Frontiers 10, 481- 494.

[18] Paulson, A., Zhong, S., Wahr, J., 2007. Inference of mantle viscosity from GRACE and relative sea level data. Geophy. J. Int., 171, 497-508. https://doi.org/10.1111/j.1365-246X.2007.03556.x.

[19] Zhang, J., 2007. Increasing Antarctic sea ice under warming atmospheric and oceanic conditions. Am. Met. Soc., 20, 2515-2529.

[20] Barnett, T. P., 1985. Long term climatic change in observed physical properties of the oceans In Detecting the Climatic Effects of Increasing Carbon Dioxide (Eds. MC MacCracken and FM Luther) US DOE/ER 0235 pp 91-107

[21] Hegerl, G.C., F. W. Zwiers, P. Braconnot, N.P. Gillett, Y. Luo, J.A. Marengo Orsini, N. Nicholls, J.E. Penner and P.A. Stott, 2007: Understanding and Attributing Climate Change. In: Climate Change 2007: The Physical Science Basis. Contribution of Working Group I to the FAR of the IPCC [Solomon, S., D. Qin, M. Manning, Z. Chen, M. Marquis, K.B. Averyt, M. Tignor and H.L. Miller (eds.)]. Cambr. Univ. Press, Cambridge, United Kingdom and New York, NY, USA.

[22] Kemp, A.C., Dutton, A., Raymo, M.E., 2015. Paleo constraints on future sea level rise. Curr. Clim. Chan. Rep., 1, 205-215.

[23] Vail, P.R., Mitchum Jr., R.M., Thompson III, S., 1977. Seismic Stratigraphy and Global Changes of Sea Level: Part 4. Global Cycles of Relative Changes of Sea Level: Section 2. Application of Seismic Reflection Configuration to Stratigraphy Interpretation. AAPG Mem. Spec. Vol., p. 83-97.

[24] Khan, A.A., Akhter, S.H., Alam, S.M.M., 2000. In: Hosani, Mohamed and Al (Ed.), Evidence of Holocene Transgression, Dolomitization and the Source of Arsenic in the Bengal Delta. Geoengineering in Arid Lands. Balkema, Rotterdam, pp. 351-355.

[25] Mörner, N.-A., 2020. Sea Level Records on Ouvéa Island in New Caledonia. Nat. Sci., 2020, Vol. 12, (No. 6), pp: 329-359. https://www.scirp.org/journal/ns

[26] Mörner, N.-A., 2019a. Rotational Eustasy as Observed in Nature. Int. J. Geos., 10, 745-757. https://doi.org/10.4236/ijg.2019.107042

[27] Mörner, N.-A., 2018. Absolute Evidence of the Absence of an on-Going Sea Level Rise on Ouvéa Island of New Caledonia. SSRG Int. J. Geoinf. Geol. Sci. (SSRG – IJGGS) – Volume 5, Issue 3, p. 30-33

[28] Mörner, N.-A., 2010. Sea level changes in Bangladesh: New observational facts. Ener. Env., 21(3), 235–249.

[29] Mörner, N.-A., 2019b. Biology and Shore Morphology: Keys to proper reconstruction of sea level changes, J. Marn. Biol. Aquas. Doi: http://dx.doi.org/ 10.31579/ 26415143/JMBA.2019 /020

[30] Loveson, V.J.; Gujar, A.R.; Iyer, S.D.; Udayaganesan, P.; Luis, R.A.A.; Gaonkar, S.S.; Chithrabhanu, P.; Torodkar, G.M., and Singhvi, A.K., 2014. Beach dynamics and oscillations of shoreline position in recent years at Miramar Beach, Goa, India: A study from GPR survey. Nat. Haz., 73(3), 2089–2106. doi:10.1007/s11069-014-1175-7.

[31] Mörner, N.-A., 2017. Coastal morphology and sea-level changes in Goa, India during the last 500 years. J. Coastal Res., 33(2), 421–434. Coconut Creek (Florida), ISSN 0749-0208.

[32] Ampou, E.E., Johan, O., Menkes, C.E., Niño, F., Birol, F., Ouillon, S., and Andréfouët, S., 2017. Coral mortality induced by the 2015–2016 El-Niño in Indonesia: the effect of rapid sea level fall. Biogeosciences, 14, 817-826.

Internet sources:
https://en.wikipedia.org/wiki/ Post-glacial_rebound.
https://commons.wikimedia.org/wiki/File:PGR_Paulson2007_Rate_of_Lithospheric_Uplift_due_to_PGR.png.
http://nsidc.org/arcticseaicenews/2015/05/
http://www.climatecentral.org/gallery/graphics/arctic_sea_ice_thinning_fall.
https://commons.wikimedia.org/wiki/File:Holocene_Temperature_Variations.png
https://www.theguardian.com/environment/2010/feb/02/hockey-stick-graph-climate-change.

INTERNATIONAL JOURNAL OF
COASTAL, OFFSHORE & ENVIRONMENTAL ENGINEERING IJCOE Vol.7/No. 2/Spring 2022 (24-30)

Available online at: www. Ijcoe.org

Risk Assessment of Fixed Offshore Jacket Platforms: A Persian Gulf Case Study

Abdolrahim Taheri[1], Behrooz Tadayon[2*], Cyrus Ershadi[3]

[1] Assistant Professor, Abadan Faculty of Petroleum, Petroleum University of Technology, Abadan, Iran; rahim.taheri@put.ac.ir*
[2] M.Sc Graduate, Civil Engineering Department, Faculty of Engineering, University of Hormozgan, Hormozgan, Iran, (Corresponding Author); behrooztadayon@yahoo.com
[3] Assistant Professor, Civil Engineering Department, Faculty of Engineering, University of Hormozgan, Hormozgan, Iran; cyrusershadi@hormozgan.ac.ir

ARTICLE INFO

Article History:
Received: 29 Dec. 2021
Accepted: 25 May. 2022

Keywords:
Risk Assessment
Structural Integrity Management
Fixed Offshore Jacket Platform
Vulnerability
Consequence of Failure

ABSTRACT

Offshore platforms are among important structures whose performance during their life-time and beyond is of significant importance. One of the approaches for ensuring a platform's fitness-for-purpose condition is the structural integrity management system. In this process, a wide range of risk assessment approaches can be carried out to investigate the platforms' performance. These assessments are divided into qualitative, semi-quantitative and quantitative methods, whose outcome is the risk level of the structure under investigation. By obtaining the risk level, the condition of the platform can be surveyed and certain actions can be defined to ensure that the platform remains fit-for-purpose. In this study, a fixed offshore jacket platform located in the phase 19 of the South Pars gas field in the Persian Gulf is investigated using a semi-quantitative risk assessment method. Based on certain assumptions, the risk level obtained for this platform can be categorized as intermediate. By knowing the risk level, risk mitigation actions can be carried out and inspection intervals can be defined.

1. Introduction

The oil and gas industry is among the important industries that has always faced significant challenges. This industry provides a huge amount of energy needed in the world and a significant part of it is in offshore areas. Therefore, this industry has always been accompanied by continuous developments in technology and related advances in dealing with hazards such as explosions, fire, hurricanes, etc., along with facing other issues such as modern exploitation needs.

Offshore platforms are considered as important structures in the oil and gas industry, which are divided into different types; including fixed and floating [1]. Due to the significant importance of these structures, extensive research has been done on their various aspects. These include examining their behavior [2, 3], analyzing their response and the dynamic behavior of their components [4], and investigating different aspects of reliability analysis applied to them [5, 6].

Fixed jacket platforms have been considered as one of the most common offshore platforms in the oil and gas industry around the world since the mid-19th century. Since the maintenance of existing platforms is economically more cost-effective than establishing a new platform in the region, it is tried to extend the operational life of these platforms even beyond their original design life. Therefore, the use of appropriate methods for continuous evaluation and inspection of these platforms during their lifetime and even beyond that is of particular importance [7].

In recent decades, several researchers have reviewed and evaluated fixed jacket platforms in different regions according to methods based on platform reliability and risk level. In 2002, Stacey et al. [8] reviewed and evaluated fixed offshore platforms in the waters around the UK and surrounding areas. Connor et al. in 2005 and 2006 [7, 9, 10] reviewed the risk-based structural integrity management of offshore oil rigs and performed some case studies on structures in the Gulf of Mexico and elsewhere. In addition, they mentioned factors such as structural ultimate limit state (ULS) analysis and reserve strength ratio (*RSR*), along with explanations of the first version of the API

(American petroleum institute) code for managing the integrity of structures. It should be noted that the structural integrity management system is a complete process to ensure that a structure is fit-for-purpose during its operational life, which consists of four main elements called data collection, evaluation, strategy and planning, and finally, execution of the program [11]. In another study, Aeran et al. [12] examined a jacket platform in the Gulf of Suez in the Red Sea. In Guede's research in 2019 [13], a comprehensive explanation of various qualitative and quantitative methods was provided to assess the level of risk of fixed platforms and apply structural integrity management system on them. In addition, a group of ten platforms with different specifications and functions were selected in this article, and after the relevant studies and analyses, the platform that was in the most critical condition was selected to continue the study and assess the relevant risk.

Petropars Iranian Company was established in 1997 and since then, various phases in the huge South Pars gas field, located 100 km off the coast of Iran in the Persian Gulf, have been established by this company and its reputable partner internationally established companies. This company is now one of the most reputable exploration and production companies in Iran [14]. The development plan for phase 19 of the South Pars gas field was handed over to Petropars Company in 2010. Drilling in this phase began in 2012 and was completed in 2015. The official inauguration of the South Pars Phase 19 development project also took place in 2017. This phase includes a total of 4 offshore platforms and 21 wells.

Due to the significant importance of the Persian Gulf region and its resources, the use of appropriate management systems to control and monitor various operations such as drilling, production, etc., should be dealt with special care. One of the important issues in this field is the evaluation of existing platforms and one of the primary methods to do so is to determine the risk of a platform's collapse. For this purpose, it is necessary to consider the vulnerability of the structure and the consequence of its failure.

One of the useful sources used in this area is the guideline provided for the evaluation of offshore jacket platforms in the North Sea; the TPM guideline [15]. According to this manual and the framework proposed therein, the vulnerability and the consequence of failure of structures are calculated using semi-quantitative methods and based on them, the risk level of the desired platform is determined. In this paper, the mentioned instructions have been applied on one of the platforms in phase 19 of the South Pars gas field and based on this approach, the risk level of the platform is determined.

2. Materials and methods

The history of the structural integrity management system dates back to the 1940s. At this time, in order to design fixed offshore platforms in shallow water, the member-based design approach was used, which also had a good performance. In fact, operating experience has shown that well-maintained platforms were durable and stable, even beyond what the member-based design approach showed. However, after the lifespan of the platforms ended, it was required to use and exploit them even beyond the specified lifespan. Therefore, the need to use appropriate approaches to this goal became more apparent [16].

For this reason, in the early 1970s, it became necessary for engineers to develop a new approach as an alternative to the member-based design controls to ensure that their intended platform continued to function in accordance with its purpose while it was safe to use. As a result, new maintenance guidelines and evaluation processes have been put in place to make better use of the full capacity of offshore structures [16].

The assessment guidelines developed in this field used a risk-based approach. This approach considers the likelihood of platform failure along with the consequence of failure, which includes three main components; namely, environmental, economic, and life safety consequences. Then, the platforms are categorized according to their risk level (e.g. high, intermediate, and low). Over time, considerable progress has been made in the capabilities of the oil and gas industry in general, and the technologies needed to achieve sufficient confidence in the reliability of various valuation methods have been developed. This led to a better and more appropriate understanding of platforms' behavior in severe offshore environmental conditions and a better ability to describe performance during structural service [16].

As more advanced technologies and methods have emerged, the need to use the structural integrity management system for offshore structures became more and more obvious, and several instructions and regulations were created for this purpose. Examples of these regulations include the US Petroleum Institute Structural Integrity Management Regulations [11], the International Standard ISO 19902 [17] and the Norwegian Regulations [18]. According to these guidelines, the structural integrity management system is divided into 4 main stages called data collection, structural evaluation, strategy and planning, and finally, program implementation. It should be noted that this process is basically a cycle and after the final stage, which is implementation of the program, new data is entered into the system and this process is repeated to ensure the fitness-for-purpose of a platform.

One of the main elements of the structural integrity management system is the calculation of the level of risk of a structure. Knowing this, it is possible to take the necessary measures to reduce this level, if

necessary, or, to determine the required inspection period as well as defining its scope and details. In general, there are several methods for calculating the level of risk, which are divided into qualitative, semi-quantitative, and fully quantitative methods. In this research, the general process of calculating the level of structural risk based on the TPM guideline [15], which is based on semi-quantitative methods, is described.
According to the TPM guideline, a risk matrix, which is a 5×5 matrix, can be used to achieve a relative rather than absolute risk level. A general example of this matrix is shown in Figure 1.

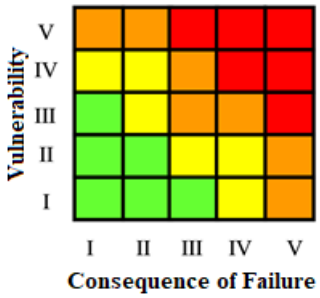

Figure 1. A sample 5×5 risk matrix

As shown in Figure 1, the formation of the risk matrix requires two main components, which are the vulnerability of the structure and the consequence of its failure. The latter one is divided into safety, environmental and economic consequences. In order to determine the level of these components, platform's characteristics such as number of legs, bracing system, and function of the structure are required. In the following, both components of risk matrix are described separately.
In the assessment of the vulnerability of the structure, the specific and generic characteristics of the structure are considered. Specific features of the structure include its position, the number of braces, and its reserve strength ratio (*RSR*). This quantity actually represents the ratio of the base shear of an undamaged structure at the time of collapse ($BS_{ult\_undamaged}$) to the design base shear (BS_{design}). In other words,

$$RSR = \frac{BS_{ult\_undamaged}}{BS_{design}} \quad (1)$$

The generic characteristics of a structure are basically the degree of redundancy provided by different bracing systems and how they affect the reliability of the structure. The degree of redundancy can be expressed using the residual resistance factor (*RRF*) obtained for generic bracing systems based on their type. This factor is actually the ratio of the base shear of the damaged structure at the time of collapse to the base shear of the undamaged structure at the time of collapse. In other words,

$$RRF = \frac{DSR}{RSR} \quad (2)$$

in which, *DSR* indicates the ratio of reserved strength in the damaged state. It is actually the ratio of the base shear of the damaged structure at the time of collapse ($BS_{ult\_damaged}$) to the design base shear. It means,

$$DSR = \frac{BS_{ult\_damaged}}{BS_{design}} \quad (3)$$

As mentioned, the *RRF* value actually indicates the degree of redundancy of a structure, and by using the *RRF* distribution of different generic bracing systems (shown in Figure 2), the degree of redundancy and robustness of the bracing system can be determined. Of course, it should be noted that the *DSR* and *RSR* values are related to the specific characteristics of each structure and the use of the obtained distributions for a generic structure cannot fully and realistically indicate the state of a particular structure. However, this method can be used for initial evaluation and assessment purposes.
As shown in Figure 2, 5 types of generic bracing systems are considered in the TPM guideline; namely, single diagonal, inversed K, K, X, and diamond shapes. It should be noted that a structure can have a combination of the mentioned bracing systems, thus making the use of engineering judgment to determine the governing bracing system behavior of the structure an important matter.
In the vulnerability assessment, after determining the type of structural bracing system, the corresponding *RRF* values can be obtained using log-normal distributions and the corresponding $RRF_{limiting}$ value is calculated. This value actually represents an estimate of the amount of *RRF* that indicates damage to the most critical member, i.e. the member whose damaged condition would have the greatest effect on the strength of the structure. The *RSR* of the structure is calculated by performing nonlinear static (pushover) analysis using the SACS software, which is based on finite element formulation for structural analysis. Now, given the two values of *RSR* and $RRF_{limiting}$, the value of $DSR_{limiting}$ is obtained using Eq. (2). Then, using the long-term load distribution (LTLD), the storm return period associated with the $DSR_{limiting}$ value is obtained. In fact, LTLD represents a linear-logarithmic relationship between the ratio of the storm wave return period to the design wave return period. This distribution basically represents the annual probability of a storm event beyond a given load *E*, which in this case is equal to the $DSR_{limiting}$ value. This probability is indicated by $P_{damaged}$ and is equal to:

$$P_{damaged} = A\exp\left(\frac{-E}{E_0}\right) \quad (4)$$

where the coefficients *A* and E_0 represent constants that are determined depending on the region under study. It should be noted that Eq. (4) is only valid when $E > 0.8$

. After calculating the value of $P_{damaged}$ and determining the probability of the critical member failure (P_{sever}), which is obtained based on the previous data from the damaged members on different platforms over previous decades, the vulnerability of the structure (P_f) can be calculated:

$$P_f = P_{damaged} . P_{sever} \quad (5)$$

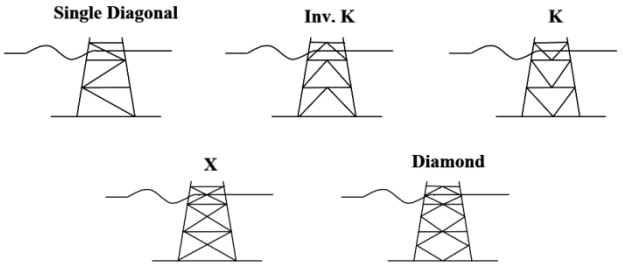

Figure 2. Generic bracing systems

The second component required for the structural risk assessment, according to the TPM guideline, is the consequence of structural failure. In general, this component is examined according to three aspects; namely, the life safety, the environment and the economic consequences. In the developed model, a scoring process is used to evaluate the overall consequence of failure rating. In this approach, which is in fact a semi-quantitative method, using the score assigned to each of the factors affecting the consequence of failure, as well as the weight assigned to each of these factors, according to the intensity of their impact and assigned importance, a value that indicates the rating of the consequence is obtained:

$$CR = 0.6SR + 0.3ER + 0.1BR \quad (6)$$

In Eq. (6), the *CR* parameter represents the overall score of the consequence of failure, and each of the parameters *SR*, *ER*, and *BR*, represent the scores of life safety, environmental, and economic factors, respectively. Since the life safety factor is more important than the other two factors, the weight considered for the effect of this factor is also higher. Each of these factors is essentially equal to the sum of its related indices listed in the relevant tables in the TPM guideline [15]. Depending on the use of the platform, whether it is manned or unmanned, and whether it is a satellite platform or it belongs to a group of structures (i.e. hub), the values of these indices are different for each factor.

The other two influential parameters in these factors are the type of hydrocarbon product extracted (i.e. oil or gas) and the percentage of personnel on board on the manned platforms. Obviously, if the platform is permanently manned, this percentage is 100%, but if the considered platform is actually part of a group of facilities connected by several bridges, then an overall estimate is needed to determine the percentage of personnel on board on each of the platforms and equipment in this complex.

Finally, after determining each of the indices in addition to considering all of the effective parameters, the value of each of the relevant factors is obtained. Then, by using them in Eq. (5) and applying the relevant weights, the rating of the consequence of failure is obtained.

After assessing the two components of the risk matrix; namely, the vulnerability and the consequence of failure, according to the risk matrix shown in Figure 1 and the classifications presented in Table 1 for both components, the risk level of the considered structure can be determined.

Table 1. Categorization of vulnerability and consequence of failure based on TPM guideline [15]

Vulnerability		**Consequence of failure**	
Value	**Group**	**Value**	**Group**
$\leq 1\times10^{-10}$	I	≤ 10	I
$\leq 1\times10^{-8}$	II	≤ 20	II
$\leq 1\times10^{-6}$	III	≤ 30	III
$\leq 1\times10^{-4}$	IV	≤ 40	IV
$> 1\times10^{-4}$	V	> 40	V

In the risk matrix, the lowest left corner represents the lowest risk level and by moving higher to the right side of the matrix, higher risk levels are determined, which represent more critical conditions.

The fixed jacket platform considered in this research belongs to phase 19 of the South Pars gas field, which has four legs and grouted piles. This platform is located at a water depth of approximately 65.7 meters. The total height of the platform is equal to 91.95 meters. The upper part of this platform, with approximate dimensions equal to 32.5 by 27.516 square meters, consists of an upper deck, an upper mezzanine deck, a lower mezzanine deck, a lower deck and a drain deck. This wellhead platform is not manned and its appurtenances include bumpers on all four legs and a boat landing on one of its rows. This platform is basically one of the three platforms in phase 19, which is equipped with minimal production equipment and is connected to other equipment by bridges and therefore, it is not a satellite platform. The general shape of this platform is shown in Figure 3.

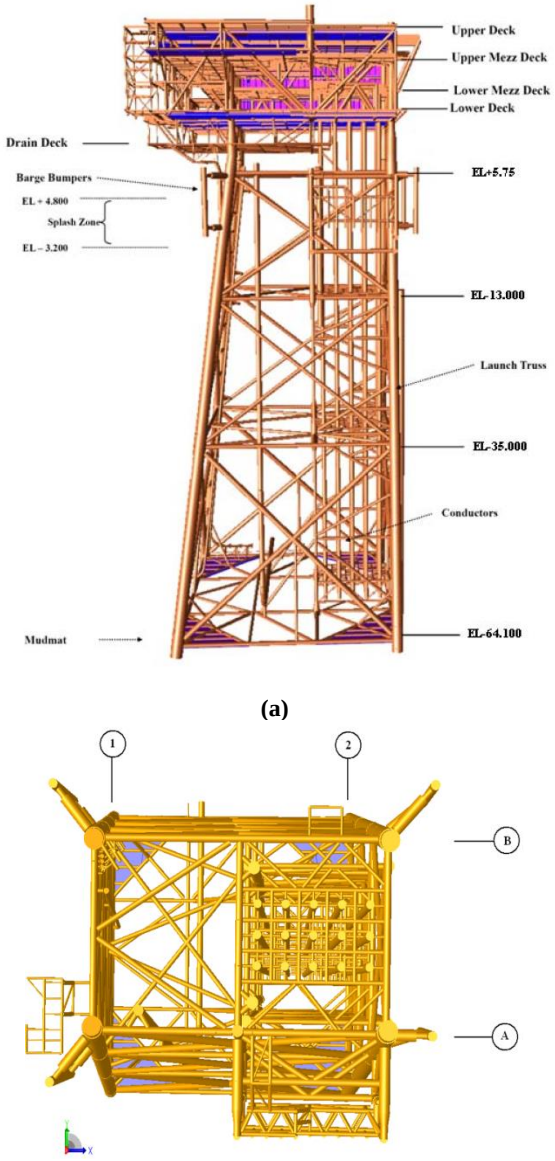

(a)

(b)

Figure 3. The fixed jacket platform under study (a) side view (b) top view

3. Results and discussions

The pushover analysis is performed using the SACS software and the *RSR* values of the platform in eight directions, as shown in Figure 4, are calculated under the extreme environmental load condition. The platform's *RSR* is actually equal to the minimum value calculated in the eight directions (most critical state), which is equal to 1.6 according to Table 2.

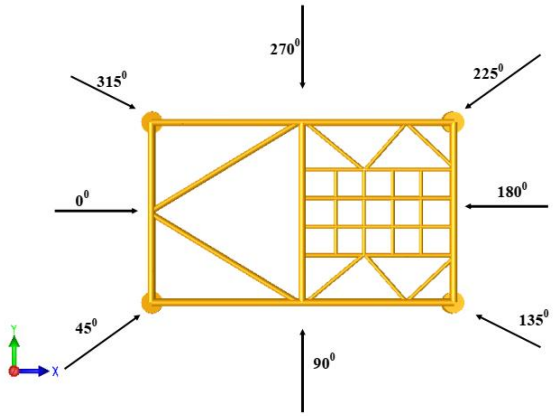

Figure 4. The eight directions for the calculation of *RSR*

Table. 2. The *RSR* values obtained in eight directions

Direction	*RSR*
0°	1.7
45°	1.7
90°	2.2
135°	2.3
180°	1.7
225°	1.6
270°	1.8
315°	2.4

According to the TPM guideline and the value of the *RRF* calculated in this guideline for sample platforms, and by matching the platform studied in this research to the most similar sample platform in terms of its specifications, its *RRF* value is estimated to be 0.9084. After obtaining the values of *RSR* and *RRF*, using Eq. (2), the *DSR* value of the structure, which is equal to the parameter *E* in Eq. (4), is calculated to be 1.4534. It should be mentioned that due to the lack of available data and proper investigation, the constant coefficients *A* and E_0 have been assumed to be equal to what is considered for the northern part of the North Sea, i.e. the values of 13.09 and 0.139, respectively. It's clear that finding the appropriate values of these parameters for the Persian Gulf region would lead to more accurate results. Finally, the value of $P_{damaged}$ according to Eq. (4) for the desired platform is equal to 3.766×10^{-4}.

To determine the value of P_{sever} in accordance with what is stated in the TPM guideline, the inspection programs are assumed to be performed every 3 years, and since the platform under study was designed after 1991, the annual probability of member failure per platform year, which is the price coefficient, is estimated to be 0.004. Therefore, P_{sever} is equal to 0.012.

Now, having $P_{damaged}$ and P_{sever}, the value of P_f, according to Eq. (5), is equal to 4.519×10^{-6}. Thus, based on Table 1, the vulnerability level of this platform belongs to group IV.

To calculate the other component of the risk matrix, which is the rating of the consequence of failure, the relevant scores for each of the life safety, environmental and economic factors are extracted according to the tables in the TPM guideline and finally, using Eq. (6), the final score of the consequence of failure is calculated. Table 3 provides the information required for this process and in Table 4, the calculation of this score and its final value is given.

Table 3. The required information about the platform under study for obtaining the score of consequence of failure

Description	
Wellhead	✓
Drilling	✓
Utilities	✓
Quarters	×
Compression / Production	✓
Export	✓
Function	×
Manned	×
Personnel on Board	-
Satellite	✓
Hub	×

Table 4. The calculation of the score of the consequence of failure of the platform under investigation

Factor	Value
Life safety (*SR*)	12
Environment (*ER*)	14
Economy (*BR*)	31
Consequence of failure (*CR*)	14

As seen in Table 4, the score of the consequence of failure of the platform under study is 14. Therefore, based on Table 1, this platform belongs to group II in terms of the consequence of failure.

By knowing the group of both components of the risk matrix, the risk level of the structure is determined. Figure 5 shows the risk level of the platform under study in this paper.

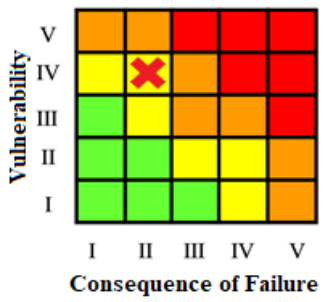

Fig. 5. The risk level of the platform under investigation

By knowing the level of risk of the structure, it is possible to define the required inspection scope and risk mitigation actions to ensure that the platform remains fit-for-purpose.

4. Conclusions

In this study, a semi-quantitative risk-based assessment method, which is one of the main elements of the structural integrity management system to assess the fitness-for-purpose condition of a structure during its life of operation, was applied on one of the fixed offshore jacket platforms in the Persian Gulf. The platform under study belongs to phase 19 of the South Pars gas field, which has four legs and grouted piles.

The method of calculating the risk level was based on the TPM guideline, according to which, using a 5×5 risk matrix that has two main components of vulnerability and consequence of failure, the structural risk level could be determined. Based on the assumptions and calculations, the risk level of the platform was obtained as moderate level, which can be used to take the necessary measures to reduce the risk level or, to determine the required inspection scope and intervals.

As mentioned throughout the text, the results of this study have been obtained using a series of assumptions due to the lack of a series of necessary information, and the purpose of this study was simply to apply the method in the TPM guideline to the platform under study. Obviously, more accurate results can be deduced by using more detailed studies and reducing these assumptions.

5. References

[1] Wilson, J.F., (2003), *Dynamics of offshore structures*. John Wiley & Sons.

[2] Sadian, R. and A. Taheri, (2016), *In-Place Strength Evaluation of Existing Fixed Offshore Platform Located in Persian Gulf with Consideration of Soil-Pile Interactions*, International Journal of Coastal and Offshore Engineering, Vol. 2(0), p. 35-42.

[3] Erfani, M.H., M.R. Tabeshpour, and H. Sayyaadi, (2019), *Capacity Evaluation of Ressalat Jacket of Persian Gulf Considering Proper Finite Element Modeling of Tubular Members*, International Journal of Coastal and Offshore Engineering, Vol. 3(2), p. 55-63.

[4] Ghasemi, M.R., N. Shabakhty, and M.H. Enferadi, (2019), *Optimized SMA Dampers in Vibration Control of Jacket-type Offshore Structures (Regular Waves)*, International Journal of Coastal and Offshore Engineering, Vol. 2(4), p. 25-35.

[5] Zeinoddini, M., H. Golpour, H. Khalili, H. Matin Nikoo, and I. Ahmadi, (2017), *Sensitivity Analysis of Selected Random Variables of Existing Offshore Jacket Structures in Persian Gulf*, International Journal of Coastal and Offshore Engineering, Vol. 5(0), p. 7-16.

[6] Taheri, A. and Jahangir. M, (2017), *Reliability Assessment of a Fixed Jacket Platform by Monte*

Carlo Simulation Using Neural Network, International Journal of Coastal and Offshore Engineering, Vol. 1(3), p. 57-64.

[7] Westlake, H., F. Puskar, P. O'Connor, and J. Bucknell, (2006), *The role of ultimate strength assessments in the Structural Integrity Management (SIM) of Offshore Structures*, Offshore Technology Conference, Offshore Technology Conference.

[8] Stacey, A., M. Birkinshaw, and J. Sharp, (2002), *Reassessment issues in life cycle structural integrity management of fixed steel installations*, International Conference on Offshore Mechanics and Arctic Engineering.

[9] O'Connor, P., J. Bucknell, S. DeFrance, H. Westlake, and F. Westlake, (2005), *Structural integrity management (SIM) of offshore facilities*, Offshore Technology Conference, Offshore Technology Conference.

[10] Westlake, H., F. Puskar, P. O'Connor, and J. Bucknell, (2006), *The development of a recommended practice for structural integrity management (SIM) of fixed offshore platforms*, Offshore Technology Conference, Offshore Technology Conference.

[11] API, R.S., (2014), *Structural integrity management of fixed offshore structures*.

[12] Aeran, A., S.C. Siriwardane, O. Mikkelsen, and I. Langen, (2017), *A framework to assess structural integrity of ageing offshore jacket structures for life extension*, Marine Structures, Vol. 56, p. 237-259.

[13] Guédé, F., (2019), *Risk-based structural integrity management for offshore jacket platforms*, Marine Structures, Vol. 63, p. 444-461.

[14] Petropars. *Petropars at a glance*. Available from: http://www.petropars.com/petropars-at-a-glance.

[15] Nelson, A., (2003), *Technical performance measures for North Sea jacket structures*. 2003: HSE Research report.

[16] Potty, N.S. and M. Akram, (2009), *Structural integrity management for fixed offshore platforms in Malaysia*, Vol. 7(2), JULY-DECEMBER 2009, ISSN 1511-6794, p. 8.

[17] ISO, E., (2007), *Petroleum and natural gas industries—Fixed steel offshore structures*. 2007, ISO Geneva.

[18] Norsok, N., (2009), *006, Assessment of Structural Integrity for Existing Offshore Load-Bearing Structures*. 2009, Draft.

INTERNATIONAL JOURNAL OF
COASTAL, OFFSHORE & ENVIRONMENTAL ENGINEERING IJCOE Vol.7/No. 2/Spring 2022 (31-38)

Available online at: www. Ijcoe.org

Fast Reverse converter Design for three moduli set $\{2^n.2^n-1.2^{n-1}-1\}$ Using CRTF

Javad Ahsan[1]. Mohammad Esmaeildoust[2*]. Amer Kaabi[3]. Vahid Zarei[4]

[1] *Faculty of Marine Engineering. Khorramshahr University of Marine Science and Technology. Khorramshahr. Iran; javad.ahsan@kmsu.ac.ir*
[2*] *Faculty of Marine Engineering. Khorramshahr University of Marine Science and Technology. Khorramshahr. Iran; m_doust@kmsu.ac.ir*
[3] *Department of Basic Sciences. Abadan Faculty of Petroleum Engineering. Petroleum University of Technology. Abadan. Iran; Kaabi_amer@put.ac.ir*
[4] *Faculty of Marine Engineering. Khorramshahr University of Marine Science and Technology. Khorramshahr. Iran; v.zarei@kmsu.ac.ir*

ARTICLE INFO

Article History:
Received: 13 Oct. 2021
Accepted: 12 Apr. 2022

Keywords:
Marine secure communication
Residue number system
CRTF
Reverse converter

ABSTRACT

Security is necessary for marine communication systems such as marine wireless sensor networks and automatic identification system which is the emerging system for automatic traffic control and collision avoidance services in the maritime transportation sector. Public key cryptography algorithms have an important role in these systems to realize secure communication systems. Public key cryptography algorithms such as RSA and Elliptic curve cryptography (ECC) have high computation costs and many works are done by researcher in order to speed up the operation. Residue number system which is a carry free system is widely used to speed up the operation in public key cryptography algorithm. In this paper. an improved RNS reverse converter for three-module set $\{2^n.2^n-1.2^{n-1}-1\}$ using chinese reminder theorem with fractional is presented. Unit gate delay and area comparison of the proposed reverse converter with literature have confirmed that the proposed reverse conversion takes fewer hardware costs and higher speed.

1. Introduction

Maritime communication systems such as Radio frequency port communication system [1]. Automatic Identification System (AIS) which is the emerging system for automatic traffic control and collision avoidance services in the maritime transportation sector [2] and marine wireless sensor networks [3] have security vulnerability and many works are done by researcher in order to provide security. Public key cryptography algorithms such as RSA [4] and ECC [5]. [6] are widely used in these systems in order to provide security. Digital signature algorithms [7] which are employed for authentication and integrity in these application [3] are also realized using public key cryptography algorithms. Public key cryptography algorithms have high computation costs and many works are done by researcher in order to speed up the operation [8]. [9]. [10]. Residue number system (RNS) [11] is a carry free number system which provides operation on parallel channel. This property led to fast arithmetic operation. Residue number system is widely used in public key cryptography algorithms in order to realize fast implementation [12]. [13].

RNS has three main parts includes forward conversion. arithmetic unit and reverse conversion. In the RNS system. the weighted numbers are converted into corresponding residues by a forward converter. The arithmetic unit consists of a modulus adder. subtractor. and a modulus multiplier for each modulus of the moduli set. This part performed on RNS numbers in parallel without carry propagation between residue channels. In order to use the result of arithmetic unit of RNS. the residues should be converted into its equivalent weighted binary number

by using a reverse converter [11]. Efficiency of the RNS system is related to form and the number of moduli. The dynamic range. the speed. and the hardware implementation of RNS systems are directly influenced by the form and the number of chosen moduli [14].

The most challenging parts of designing a RNS system is the design of reverse converter. Design of the reverse converter is critical step in terms of computational speed. Algorithms such as Chinese Remainder Theorem (CRT) and mixed-radix conversion (MRC). are used to design a reverse converter. Many works are done by researcher on different moduli set and efficient reverse converter are designed. The RNS bases has been selected with the aim of achieving optimal reverse converter. high dynamic range and simple computational architecture for implementation with the minimum hardware resources. time delay. and low power consumption. In [15]. three moduli set $\{2^n.\ 2^n\text{-}1.\ 2^n\text{+}1\}$ is presented. This moduli set is well-formed and led to simple hardware implementation for RNS design. However arithmetic operation in moduli 2^n+1 is more complex. to accelerate the speed of the RNS arithmetic unit. in [16] modulus 2^{n+1}-1 is used instead. and the RNS is designed with the moduli set $\{2^n.\ 2^n\text{-}1.\ 2^{n+1}\text{-}1\}$. In [17] the moduli set $\{2^{n+k}.\ 2^n\text{-}1.\ 2^{n+1}\text{-}1\}$is employed to design an efficient RNS arithmetic unit.

In [18]. efficient reverse converter is designed for moduli set $\{2^n.\ 2^n\text{-}1.\ 2^{n-1}\text{-}1\}$ using Chinese Reminder Theorem with fractional (CRTF). In order to have fast and efficient implementation of the converter. in this paper an improvement over converter reported in [18] is presented. The improved version has spare one 4*n*-bit Kogge-stone's prefix adder [19] from the critical path. Therefore. faster reverse converter design is resulted.

This paper is organized as follows: Section 2 presents the basic RNS mathematics. The reverse converter for moduli set $\{2^n.\ 2^n\text{-}1.\ 2^{n-1}\text{-}1\}$ proposed in [18] is detailed in section 3. Section 4 presents the proposed reverse converter. The implementation and performance evaluation results are presented in Section 5. Finally. Section 6 concludes the paper.

2. Related Background

2.1. RNS Background

The RNS is defined in terms of relatively prime moduli set $\{m_1.m_2\ldots..m_n\}$ that is $\gcd(m_i.m_j) = 1$ for $\neq j$. A weighted number *X* can be represented as $X = (x_1.\ x_2\ldots..x_n)$. Where

$$X = X\ mod\ m_i = |X|_{m_i}.\quad 0 \le m_i < x_i. \tag{1}$$

Such a representation is unique for any integer X in the range $[0.M-1]$. where M is the dynamic range of the moduli set $\{m_1.m_2\ldots..m_n\}$. which is equal to the product of m_i terms $(M = m_1.m_2\ldots..m_n)$ [11].

2.2. Chinese Remainder Theorem

The Chinese Remainder Theorem (CRT) may rightly be viewed as one of the most important fundamental results in the theory of residue number systems. Computing weighted number X form its RNS representation. i.e.. $(x_1.\ x_2\ldots..x_n)$. based on the moduli set $\{m_1.m_2\ldots..m_n\}$ is as follows:

$$X = \left|\sum_{i=1}^{n}\left|M_i^{-1}\right|_{m_i}M_i x_i\right|_M. \tag{2}$$

where $M_i = M/m_i$. $\left|M_i^{-1}\right|_{m_i}$is the multiplicative inverse of $M_i\ \ i\ =\ 1.2\ldots..n$ [20].

2.3. Approximate CRT

The modification of the CRT using fractional values. namely approximate CRT. was introduced for the first time in [21] to perform sign detection and division in RNS. Considering a number X in RNS with the moduli set $\{m_1.m_2\ldots..m_n\}$. if it is divided by M. the following formula can be obtained:

$$\tilde{X} = \frac{X}{M} = \left|\sum_{i=1}^{n}\frac{\left|M_i^{-1}\right|_{m_i}}{m_i}x_i\right|_1 = \left|\sum_{i=1}^{n}k_i x_i\right|_1. \tag{3}$$

Where.

$$k_i = \frac{\left|M_i^{-1}\right|_{m_i}}{m_i}.\quad i = 1.2.\ldots..n. \tag{4}$$

The value $\tilde{X}$ can be considered as a positional characteristic of *X*. and the number *X* can be obtained by

$$X = \tilde{X}M. \tag{5}$$

Block diagram of CRTF for general reverse conversion is shown in figure 1.

2.4. Chinese Remainder Theorem with Fractions

In [22] presents a modified version of the approximate CRT. named CRTF to perform residue-to-binary conversion. First. number of the fractional bits required for an accurate residue-to-binary conversion as follows:

$$N = \lceil \log_2 M\mu - 1 \rceil. \tag{6}$$

Where

$$M = \prod_{i=1}^{n} m_i \,.\, \mu = \sum_{i=1}^{n} (m_i - 1). \tag{7}$$

Operations on real numbers in computing devices results in high hardware and delay. Hence. it is necessary to replace fraction computations with integer ones. This can be achieved by making some modifications in the algorithm. To have integer calculations. each number k_i should be multiplied by 2^N. The integer part of each of the resulting numbers plays the role of fractional part in the original method. while bits exceeding order N. should be discarded and not considered in calculations. In other words. calculations must be performed in modulus 2^N.

$$k_i^* = \left\lceil \frac{\left|M_i^{-1}\right|_{m_i}}{m_i} . 2^N \right\rceil .\ i = 1.2. \ldots . n. \tag{8}$$

The value of X^* obtained as follows:

$$X^* = \left| \sum_{i=1}^{n} k_i^* x_i \right|_{2^N} . \tag{9}$$

The X^*can be used to perform residue-to-binary conversion of X by the following relation where $\lfloor A \rfloor$ means the floor of A.

$$X = \left\lfloor \frac{X^* M}{2^N} \right\rfloor. \tag{10}$$

Block diagram of the general reverse converter suing CRTF is shown in Figure 1.

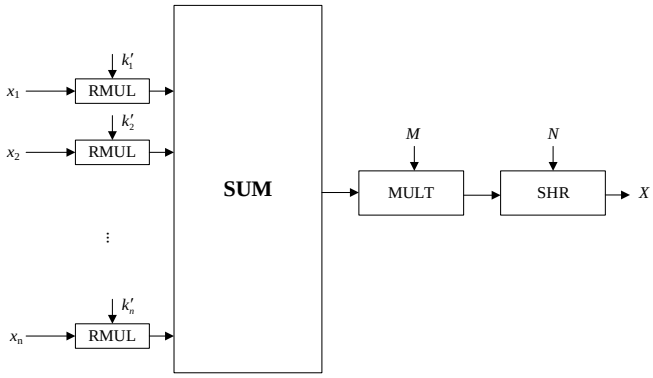

Figure 1. Block diagram of general reverse converter using CRTF [21]

3. Reverse converter for moduli set $\{2^n . 2^n - 1 . 2^{n-1} - 1\}$ proposed in [18]

In [18]. efficient reverse converter has been proposed for the moduli set $\{2^n . 2^n - 1 . 2^{n-1} - 1\}$ using CRTF. In the following the reverse converter reported in [18] is detailed.

Consider three moduli $\{m_1. m_2. m_3\} = \{2^n . 2^n - 1 . 2^{n-1} - 1\}$ with dynamic range M = $2^n(2^n\text{-}1)(2^{n\text{-}1}\text{-}1)$.

The values of the multiplicative inverse M_i^{-1} are:

$$M_1^{-1} \equiv 1 + 2^{n-1} (mod\ 2^n) \tag{11}$$

$$M_2^{-1} \equiv 2^n - 3 (mod\ 2^n - 1) \tag{12}$$

$$M_3^{-1} \equiv 2^{n-2} (mod\ 2^{n-1} - 1) \tag{13}$$

Consider the cases where $N = 4n$. i.e.. where $n > 4$. The coefficients $k_1 . k_2 . k_3$ in Eq. 4 are presented in [18] as follows:

$$k_1 = \frac{\left|M_1^{-1}\right|_{m_1}}{m_1} = \frac{2^{n-1} + 1}{2^n} = \frac{1}{2} + \frac{1}{2^n} \tag{14}$$

$$k_2 = \frac{\left|M_2^{-1}\right|_{m_2}}{m_2} = \frac{2^n - 3}{2^n - 1} \tag{15}$$

$$k_3 = \frac{\left|M_3^{-1}\right|_{m_3}}{m_3} = \frac{2^{n-2}}{2^{n-1} - 1} \tag{16}$$

The coefficients $k_1^* . k_2^* . k_3^*$ in Eq. 8 are calculated as follows:

$$k_1^* = \left\lceil \frac{\left|M_1^{-1}\right|_{m_1}}{m_1} . 2^N \right\rceil = \lceil 2^N . k_1 \rceil \tag{17}$$

$$k_1^* = \lceil 2^N . k_1 \rceil = \left\lceil 2^N . \left(\frac{1}{2} + \frac{1}{2^n}\right)\right\rceil = \left\lceil 2^{4n} . \left(\frac{1}{2} + \frac{1}{2^n}\right)\right\rceil =$$

$$= \lceil 2^{4n} . (2^{-1} + 2^{-n}) \rceil = \lceil 2^{4n-1} + 2^{3n} \rceil = 2^{4n-1} + 2^{3n}$$

The numerical value of k_1^* is:

$$k_1^* = \underbrace{010 \dots 001}_{n-bits}\underbrace{00 \dots 000}_{n-bits}\underbrace{00 \dots 000}_{n-bits}\underbrace{00 \dots 000}_{n-bits} \quad (18)$$

For simplicity the zero bits in the most significant bits can be removed:

$$k_1^* = \underbrace{10 \dots 001}_{(n-1)-bits}\underbrace{00 \dots 000}_{n-bits}\underbrace{00 \dots 000}_{n-bits}\underbrace{00 \dots 000}_{n-bits} \quad (19)$$

The number k_1^* has a $(4n-1)$-bits width.
Find the value k_2^*:

$$k_2^* = \lceil 2^N . k_2 \rceil = \left\lceil 2^{4n} . \left(\frac{2^n - 3}{2^n - 1}\right)\right\rceil \quad (20)$$

Since the number k_2^* is taken rounded up. therefore k_2^* can be rewritten as:

$$k_2^* = \underbrace{11 \dots 101}_{n-bits}\underbrace{11 \dots 101}_{n-bits}\underbrace{11 \dots 101}_{n-bits}\underbrace{11 \dots 101}_{n-bits} \quad (21)$$

Since this number contains more ones than zeros. in [18] the technique which introduced in [23] is employed in order to simplified the required operation:

$$|(-X).(-C)|_{2^\alpha} = \left|\bar{X}.\left(\bar{C} + 1 - 2^f\right) + \Delta_{COR}\right|_{2^\alpha} \quad (22)$$

The correction factor is calculated by the formula:

$$\Delta_{COR} = \left|(1 - 2^g).\left(\bar{C} + 1 - 2^f\right)\right|_{2^\alpha} \quad (23)$$

where g is the bit width of the number X. f is the bit width k_i^* . and α is the bit width N. Let us find the correction factor by the formula (23):

$$\Delta_{COR} = \left|(1 - 2^n).\left(\overline{k_2^*} + 1 - 2^{4n}\right)\right|_{2^{4n}} = |2|_{2^{4n}} \quad (24)$$

After inversion the value k_2^*. we have:

$$\overline{k_2^*} = \underbrace{00 \dots 010}_{n-bits}\underbrace{00 \dots 010}_{n-bits}\underbrace{00 \dots 010}_{n-bits}\underbrace{00 \dots 010}_{n-bits} \quad (25)$$

Remove the zero bits in the most significant bits results:

$$\overline{k_2^*} = \underbrace{10}_{2bits}\underbrace{00 \dots 010}_{n-bits}\underbrace{00 \dots 010}_{n-bits}\underbrace{00 \dots 010}_{n-bits} \quad (26)$$

We get that the number $\overline{k_2^*}$ has a bit width $(3n+2)$-bits and $\Delta_{COR} = 2_{10} = 10_2$ is 2 bits.
Find the value k_3^*:

$$k_3^* = \lceil 2^N . k_3 \rceil = \left\lceil 2^{4n} . \left(\frac{2^{n-2}}{2^{n-1} - 1}\right)\right\rceil \quad (27)$$

Since the number k_3^* s taken rounded up. We get:

$$k_3^* = \underbrace{10 \dots 000}_{(n-1)-bits}\underbrace{10 \dots 000}_{(n-1)-bits}\underbrace{10 \dots 000}_{(n-1)-bits}\underbrace{10 \dots 000}_{(n-1)-bits}\underbrace{1001}_{4bits} \quad (28)$$

We get that the number k_3^* has a bit width 4*n*-bit.

4. Improved Reverse converter for moduli set $\{2^n . 2^n - 1 . 2^{n-1} - 1\}$

In order to realize the fast implementation of the reverse converter. some part of the reverse converter for the moduli set $\{2^n . 2^n - 1 . 2^{n-1} - 1\}$ proposed in [18] are redesigned which is detailed as follows.
The first step will be the calculation of value X^*. which obtained by taking modulo N (4*n*-bit) as

$$X^* = \left|\sum_{i=1}^{n} x_i k_i^*\right|_{2^N} \quad (29)$$

After applying the compression technique reported in [18]. four terms are resulted which is shown in figure 2. The last term x_{30}occupies 1 bit - the most significant bit of the number. Let's discard it for further summation. Let the first three terms be equal to $v_1 . v_2$ and v_3. In [18]. in order to realize the hardware implementation of summation of partial product shown in figure 2. one 4n-bit CSA and XOR followed by one KSA adder are employed. In order to achieve faster implementation. in the improved version. KSA adder is eliminated and two 4n-bit variable named X_1^* and X_2^* will send to next level of the design. It should be noted that one KSA adder are spare from the critical path. Therefore. in the next step. the value of $(X_1^* + X_2^*) \times M$ should be calculated. Since M the dynamic range is equal to $2^n(2^n - 1)(2^{n-1} - 1) = 2^{3n-1} - 2^{2n} - 2^{2n-1} + 2^n$. we have

$$X_1^* \times M = X_1^* \times \left(2^{3n-1} - 2^{2n} - 2^{2n-1} + 2^n\right) \quad (30)$$

$$= X_1^* 2^{3n-1} - X_1^* 2^{2n} - X_1^* 2^{2n-1} + X_1^* 2^n$$

$$= X_{11}^* + X_{12}^* + X_{13}^* + X_{14}^*$$

	4n-1	4n-2	...	3n+1	3n	3n-1	...	n+3	n+2	n+1	n	n-1	n-2	...	5	4	3	2	1	0
$V_1 =$	$x_{1(n-1)}$	$x_{1(n-2)}$	...	x_{11}	x_{10}	$\overline{x_{2(n-2)}}$	...	$\overline{x_{22}}$	$\overline{x_{21}}$	$\overline{x_{20}}$	$\overline{x_{2(n-1)}}$	$\overline{x_{2(n-2)}}$	$\overline{x_{2(n-3)}}$	...	$\overline{x_{24}}$	$\overline{x_{23}}$	$\overline{x_{22}}$	$\overline{x_{21}}$	$\overline{x_{20}}$	x_{30}
$V_2 =$	x_{10}	$\overline{x_{2(n-3)}}$	...	$\overline{x_{20}}$	$\overline{x_{2(n-1)}}$	$x_{3(n-2)}$	...	x_{31}	x_{30}	$x_{3(n-2)}$	$x_{3(n-3)}$	$x_{3(n-4)}$	$x_{3(n-2)}$	...	x_{35}	x_{34}	x_{33}	x_{32}	1	
$V_3 =$	$\overline{x_{2(n-2)}}$	$x_{3(n-2)}$	...	x_{31}	x_{30}								$x_{3(n-5)}$	...	x_{32}	x_{31}	x_{30}		x_{31}	
	x_{30}																			

Figure 2. Partial product for calculation of $X^* = |\sum_{i=1}^{n} x_i k_i^*|_{2^N}$ [18]

Where

$$X_{11}^* = \overline{X_1^*}\,\underbrace{11\ldots1}_{2n}$$
$$X_{12}^* = \overline{X_1^*}\,\underbrace{11\ldots1}_{2n-1}$$
$$X_{13}^* = X_1^*\,\underbrace{00\ldots0}_{n-2}\,10$$
$$X_{14}^* = X_1^*\,\underbrace{00\ldots0}_{3n-1}$$

$$X_2^* \times M = X_2^* \times \left(2^{3n-1} - 2^{2n} - 2^{2n-1} + 2^n\right)$$

$$= X_2^* 2^{3n-1} - X_2^* 2^{2n} - X_2^* 2^{2n-1} + X_2^* 2^n \quad (31)$$

$$= X_{21}^* + X_{22}^* + X_{23}^* + X_{24}^*$$

Where

$$X_{21}^* = \overline{X_2^*}\,\underbrace{11\ldots1}_{2n}$$
$$X_{22}^* = \overline{X_2^*}\,\underbrace{11\ldots1}_{2n-1}$$
$$X_{23}^* = X_2^*\,\underbrace{00\ldots0}_{n-2}\,10$$
$$X_{24}^* = X_2^*\,\underbrace{00\ldots0}_{3n-1}$$

Hardware implementation of the improved reverse converter is shown in Figure 3. In order to realize Eq. (30) and (31). four sage CSA followed by one KSA adder is employed. Hardware details of the proposed reverse converter included in Table 1.

Table 1. Detailed of each component for the first level design of the reverse converter

Component	FA	XOR	AND	OR
CSA (1)	4*n*	-	-	-
CSA (2)	6*n*	-	-	-
CSA (3)	6*n*-2	-	-	-
CSA (4)	6*n*	-	-	-
CSA (5)	7*n*-1	-	-	-
CSA (6)	7*n*-1	-	-	-
CSA (7)	7*n*-1	-	-	-
KSA	-	14*n*-2	21*n*-3	7*n*-1

5. Performance Evaluation

In this section. the performance of the proposed reverse converter has been compared with other converters for the moduli set $\{2^n.2^n-1.2^{n-1}-1\}$ introduced in [18]. The conversion delay and hardware cost of the proposed converters and converter [18] are illustrated in Table 2.

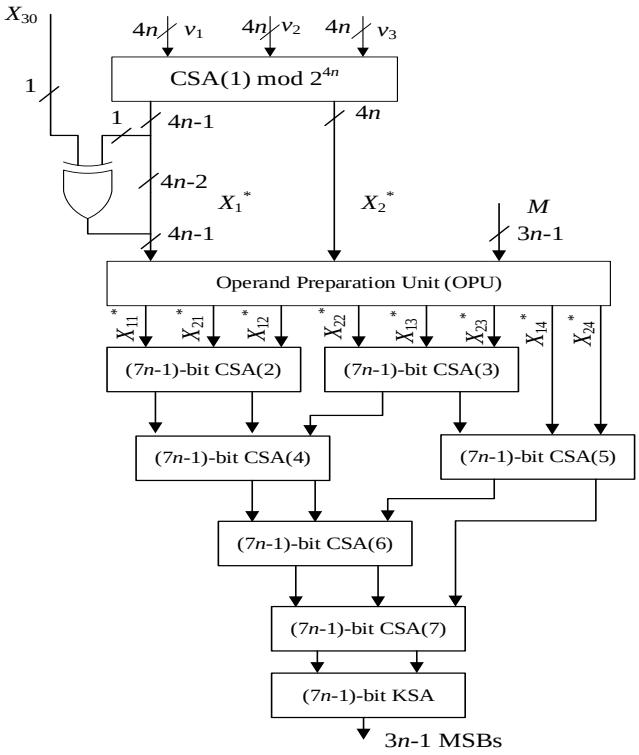

Figure 3. Hardware implementation of the proposed reverse converter

Table 2. Hardware costs and conversion delay comparison

Converter	Hardware requirement	Delay

P. Lyakhov [18]	$(3.5n^2+3n)A_{FA}$ $+(22n-4)A_{XOR}$ $+(2\alpha+\beta+n)A_{AND}$ $+(\alpha+\beta)A_{OR}$	$(n/2+1)D_{FA}$ $+2D_{KSA}$
Proposed	$(43n-5)A_{FA}$ $+(14n-2)A_{XOR}$ $+(2\gamma+n)A_{AND}$ $+(\gamma)A_{OR}$	$5D_{FA}+1D_{KSA}$

$\alpha = (7n-2)\log(7n-2)-7n+3.$
$\beta = 4nlog(4n)-4n+1.$
$\gamma = (7n-1)\log(7n-1)-7n+2.$

The Kogge-Stone structure delay is given by $[\log_2 n]$ and the computational nodes is given by $[n\log_2 n - n + 1]$ where *n* is the number of input bits [24].
To have a better comparison and deriving area and delay estimations. the unit gate model [25] is used. According to this model. each FA. half adder (HA). 2×1 MUX. XOR. XNOR. AND. OR gates considered as 7. 3. 3. 2. 2. 1. 1 gates in area and 4. 2. 2. 2. 2. 1. 1 gates in delay. respectively. Table 3 shows the unit gate delay and area comparison. According to the calculated phrase for the amount of hardware required in the converter reported in [18]. by growth of *n* the amount of hardware required will increase with a large slope compared to the proposed converter. To provide more accurate analysis. for different values of *n* the unit gate delay. area and AT are calculated and illustrated in Figure 4. It can be seen that compared to the converter reported in [18]. the proposed converters have achieved a better delay and needs less hardware. Low hardware requirements of the proposed converters. led to efficient and simple implementation on real hardware with the growth of *n*. the proposed converter has achieved 87.5% less delay and 37.6% less hardware requirements compared to converter reported in [18] for 16-bits design.

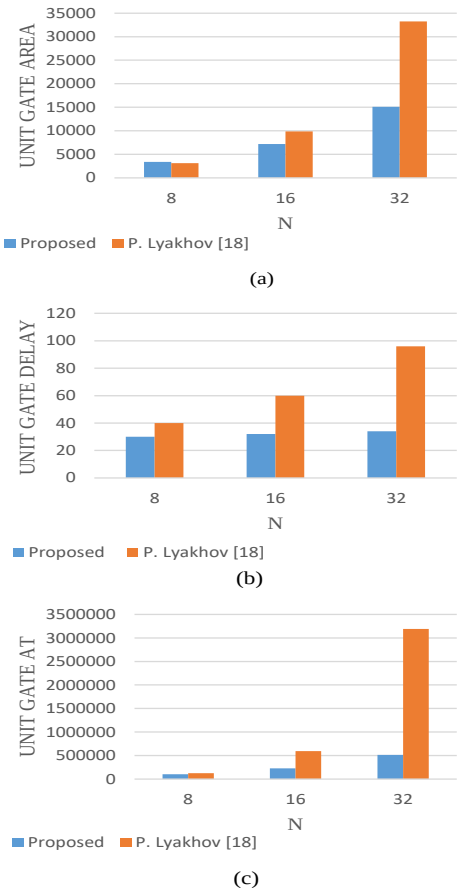

Figure 4. Unit Gate Comparison: (a) Unit gate Area. (b) Unit Gate Delay and (c) Unit Gate AT

Table 3. Unit gate delay and area evaluation

Converter	Unit Gate Area	Unit Gate Delay
P. Lyakhov [18]	$24.5n^2+66n-8$ $+3\alpha+2\beta$	$(2n+4)$ $+4(\log_2 n)+8$
Proposed	$330n-39+3\gamma$	$20+2(\log_2 n)+4$

$\alpha = (7n-2)\log(7n-2)-7n+3.$
$\beta = 4nlog(4n)-4n+1.$
$\gamma = (7n-1)\log(7n-1)-7n+2.$

6. Conclusions

Public key cryptography algorithms have an important role in marine communication systems which secure communication is needed such as marine wireless sensor networks and Automatic identification systems. Carry free property of residue number system makes it suitable to be applied in public key cryptography algorithm in order to achieve higher speed. In this paper. an improved reverse converter for three-module set $\{2^n.2^{n-1}.2^{n-1}-1\}$ using CRTF is presented. The proposed converter has achieved less hardware requirement as well as less delay. Unit gate delay and area comparison of the proposed reverse converter with literature have confirmed that the proposed reverse converter has achieved noticeable

improvements in hardware costs. conversion delay and AT metric.

8. Reference

[1] Y. J. Kim and K. Kyung. "Secured radio communication based on fusion of cryptography algorithms." in *2015 IEEE International Conference on Consumer Electronics (ICCE)*. 2015. pp. 388–389. doi: 10.1109/ICCE.2015.7066457.

[2] A. Goudossis and S. K. Katsikas. "Towards a secure automatic identification system (AIS)." *J. Mar. Sci. Technol.*. vol. 24. no. 2. pp. 410–423. 2019. doi: 10.1007/s00773-018-0561-3.

[3] L. Wei. L. Zhang. D. Huang. and K. Zhang. "Efficient and provably secure identity-based multi-signature schemes for data aggregation in marine wireless sensor networks." in *2017 IEEE 14th International Conference on Networking. Sensing and Control (ICNSC)*. 2017. pp. 593–598. doi: 10.1109/ICNSC.2017.8000158.

[4] R. L. Rivest. A. Shamir. and L. M. Adleman. "A method for obtaining digital signatures and public key cryptosystems." *Secur. Commun. Asymmetric Cryptosystems*. vol. 21. no. 2. pp. 217–239. 2019.

[5] B. N. Koblitz. "Elliptic Curve Cryptosystems." vol. 4. no. 177. pp. 203–209. 1987.

[6] V. S. Miller. "Use of Elliptic Curves in Cryptography." *Lect. Notes Comput. Sci. (including Subser. Lect. Notes Artif. Intell. Lect. Notes Bioinformatics)*. vol. 218 LNCS. pp. 417–426. 1986. doi: 10.1007/3-540-39799-X_31.

[7] S. Goldwasser. S. Micali. and R. L. Rivest. "Digital signature scheme secure against adaptive chosen-message attacks." *S[1] S. Goldwasser. S. Micali. R. L. Rivest. "Digital Signat. scheme Secur. against Adapt. chosen-message attacks." SIAM J. Comput. vol. 17. no. 2. pp. 281–308. 1988. doi 10.1137/0217017.IAM J. Comput.*. vol. 17. no. 2. pp. 281–308. 1988. doi: 10.1137/0217017.

[8] M. Esmaeildoust. D. Schinianakis. H. Javashi. T. Stouraitis. and K. Navi. "Efficient RNS implementation of elliptic curve point multiplication over GF(p)." *IEEE Trans. Very Large Scale Integr. Syst.*. vol. 21. no. 8. pp. 1545–1549. 2013. doi: 10.1109/TVLSI.2012.2210916.

[9] D. M. Schinianakis. A. P. Fournaris. H. E. Michail. A. P. Kakarountas. and T. Stouraitis. "An RNS implementation of an Fp elliptic curve point multiplier." *IEEE Trans. Circuits Syst. I Regul. Pap.*. vol. 56. no. 6. pp. 1202–1213. 2009. doi: 10.1109/TCSI.2008.2008507.

[10] L. Imbert. J. Bajard. L. Imbert. J. B. A. Full. and R. N. S. Implementation. "A Full RNS Implementation of RSA To cite this version : HAL Id : lirmm-00090366 A Full RNS Implementation of RSA." 2006.

[11] K. Navi. A. S. Molahosseini. and M. Esmaeildoust. "How to teach residue number system to computer scientists and engineers." *IEEE Trans. Educ.*. vol. 54. no. 1. pp. 156–163. 2011. doi: 10.1109/TE.2010.2048329.

[12] S. Asif. M. S. Hossain. Y. Kong. and W. Abdul. "A Fully RNS based ECC Processor." *Integration*. vol. 61. pp. 138–149. 2018. doi: https://doi.org/10.1016/j.vlsi.2017.11.010.

[13] S. Asif and Y. Kong. "Highly Parallel Modular Multiplier for Elliptic Curve Cryptography in Residue Number System." *Circuits. Syst. Signal Process.*. vol. 36. no. 3. pp. 1027–1051. 2017. doi: 10.1007/s00034-016-0336-1.

[14] W. Wang. M. N. S. Swamy. and M. O. Ahmad. "Moduli selection in RNS for efficient VLSI implementation." in *Proceedings of the 2003 International Symposium on Circuits and Systems. 2003. ISCAS '03.*. 2003. vol. 4. pp. IV–IV. doi: 10.1109/ISCAS.2003.1205945.

[15] Y. Wang. X. Song. M. Aboulhamid. and H. Shen. "Adder based residue to binary number converters for (2/sup n/-1. 2/sup n/. 2/sup n/+1)." *IEEE Trans. Signal Process.*. vol. 50. no. 7. pp. 1772–1779. 2002. doi: 10.1109/TSP.2002.1011216.

[16] A. Hiasat. "An Efficient Reverse Converter for the Three-Moduli Set ($2^{n+ 1}-1. 2^{n}. 2^{n}-1$)." *IEEE Trans. Circuits Syst. II Express Briefs*. vol. 64. no. 8. pp. 962–966. 2016.

[17] A. Hiasat and L. Sousa. "On the Design of RNS Inter-Modulo Processing Units for the Arithmetic-Friendly Moduli Sets {2 n+ k. 2 n− 1. 2 n+ 1− 1}." *Comput. J.*. vol. 62. no. 2. pp. 292–300. 2019.

[18] P. Lyakhov. M. Bergerman. N. Semyonova. D. Kaplun. and A. Voznesensky. "Design Reverse Converter for Balanced RNS with Three Low-cost Modules." no. 3. pp. 1–7. 2021. doi: 10.1109/meco52532.2021.9460200.

[19] P. M. Kogge and H. S. Stone. "A parallel algorithm for the efficient solution of a general class of recurrence equations." *IEEE Trans. Comput.*. vol. 100. no. 8. pp. 786–793. 1973.

[20] A. Omondi and B. Premkumar. *Residue Number Residue Number*. 1951.

[21] C. Y. Hung and B. Parhami. "An approximate sign detection method for residue numbers and its application to RNS division." *Comput. Math. with Appl.*. vol. 27. no. 4. pp. 23–35. 1994. doi: 10.1016/0898-1221(94)90052-3.

[22] N. I. Chervyakov. A. S. Molahosseini. P. A. Lyakhov. M. G. Babenko. and M. A. Deryabin. "Residue-to-binary conversion for general moduli sets based on approximate Chinese remainder theorem." *Int. J. Comput. Math.*. vol. 94. no. 9. pp. 1833–1849. 2017. doi: 10.1080/00207160.2016.1247439.

[23] H. Nakahara and T. Sasao. "A High-speed Low-power Deep Neural Network on an FPGA based on the Nested RNS: Applied to an Object Detector."

in *2018 IEEE International Symposium on Circuits and Systems (ISCAS)*. 2018. pp. 1–5.

[24] S. G. R and R. Kalaimathi. “Design and Analysis of Kogge-Stone and Han-Carlson Adders in 130nm CMOS Technology.” no. March 2018. 2020.

[25] M. Obeidi Daghlavi. M. R. Noorimehr. and M. Esmaeildoust. “Efficient two-level reverse converters for the four-moduli set {2n−1. 2n–1. 2n−1–1. 2n+1–1}.” *Analog Integr. Circuits Signal Process.*. vol. 0123456789. 2020. doi: 10.1007/s10470-020-01749-z.

INTERNATIONAL JOURNAL OF
COASTAL, OFFSHORE & ENVIRONMENTAL ENGINEERING IJCOE Vol.7/No. 2/Spring 2022 (39-48)

Available online at: www. Ijcoe.org

Experimental Analysis of the Effect of a Submerged obstacle and Floating Wave Barrier in front of a Rubble Mound Breakwater on Diminishing the Damage Parameter

Ramin Vafaeipour Sorkhabi [1*], Mohammad Taghi Alami [2], Alireza Naseri[3], Alireza Mojtahedi[4]

[1] Assistant professor, Department of Civil Engineering, Tabriz Branch, Islamic Azad University, Tabriz, Iran, raminvafaei@yahoo.com*

[2] Professor, Department of Water Resources Management, Faculty of Civil Engineering, University of Tabriz, Tabriz, Iran, mtaalami@tabrizu.ac.ir

[3] Ph.D. Candidate, Water Engineering and Hydraulic Structures, University of Tabriz, Tabriz, Iran, naseri@gmx.com

[4] Associate professor, Department of Water Resources Management, Faculty of Civil Engineering, University of Tabriz, Tabriz, Iran, a.mojtahed@tabrizu.ac.ir

ARTICLE INFO

Article History:
Received: 18 Feb. 2020
Accepted: 22 May. 2022

Keywords:
Rubble mound breakwater
Random wave
Damage parameter
Submerged obstacle
Floating wave barrier

ABSTRACT

The aim of this research was to compare the performance of a submerged obstacle and floating wave barrier in the stability of rubble mound breakwaters based on the damage parameter. The submerged obstacle was attached to the toe, and the floating wave barrier was installed 50 cm from a reshaping breakwater. We carried out tests in a 35 m flume at SCWMRI. Random waves with the JONSWAP spectrum influenced the breakwater. We then analyzed the structure's reshaping using close-range photogrammetric imaging by constructing the DEM and DSM to record the displacement of rocks. Furthermore, we obtained the eroded area and the damage parameter from the integrated model at eight cross-sections at equal distances. We showed that the damage parameter increased by 39.12 and 44.44%, respectively, by increasing the relative wave height from 0.36 to 0.48 and 0.6. Also, the damage parameter increased by 22.94 and 28.26%, respectively, by increasing the relative wave period from 0.6 to 0.8 and 1. In addition, regarding different modes, we obtained the damage parameter in the breakwater without the submerged obstacle and the floating barrier 1.116 under random waves. The damage parameter decreased to 0.701 (i.e., 37.19%) by using the submerged obstacle, while the wave barrier reduced this parameter to 0.735 (i.e., 34.14%); thus, the obstacle has outperformed the wave barrier. Using the obstacle simultaneously with the wave barrier reduced the damage parameter by 51.79%, confirming the highest efficiency and performance among models. Consequently and based on the experiments and findings in this study, this model was suggested for adoption.

1. Introduction

Rubble mound breakwaters (RMBs) are used to dissipate sea wave's energy and prevent damages to facilities and shoreline areas. These structures generally involve three main layers: core, filter, and armor [1]. It has been tried to minimize the hydrodynamic forces from the waves by reshaping and launching RMBs to create a stable structure profile [2]. At present, researchers are performing numerous tests on the stability of the armor layer and the dimensions of the reshaping RMBs. Sayao & Da Silva (2016) studied the relationship between structural features such as wall slope, crest width, and breakwater height with the performance of the attacking wave [3]. In modeling, Lamberti et al. (1994) emphasized the importance of water depth at the structure's base and shallow water conditions. They showed that the final profile deformation coefficients were related to reflection depth, wave sharpness, and floor slope in addition to wave height [4]. In the design and construction of breakwaters, it is vital to reduce the waves' energy and not be destroyed by the waves. RMB

damage indicates demolition of the structure and hydraulic instability against the waves [5]. Thus, modeling the damage progression and investigating the representative parameters of this process for boosting the performance and lifespan of the breakwater seems essential. Campos et al.(2020), noting the complexity of the progression of damage in the Armor layer due to the random nature of the impact of the waves, considered it very useful and essential to monitor the structure's performance by accurate imaging techniques [6]. By examining the stability of RMBs in terms of breaking similarity parameter, Sayao (1998) evaluated the permeability of the structure as an essential factor in the hydraulic stability of the structure [7]. Dimensions of the rocks used in breakwater are related to the armor damage level in the face of the waves. In experiments, Rao and Pramod (2003) showed that as the size of the rocks decreases, the amount of damage to them increases [8]. In another study, Panagiota et al. (2018) also assessed that the leading cause of failure of conventional RMBs was mainly due to damage to the armor layer or scouring of the structural toe or upward and overflow of waves [9]. Researchers have considered selecting crucial variables to reduce the number of experiments without affecting the results in estimating breakwater damage levels. Researchers such as Janardhan et al. (2015) have used various methods, such as Principal Components Regression (PCR) [10].

The use of submerged breakwaters is also one of the new solutions against coastal erosion. Wave breaking by submerged breakwaters brings about turbulence at the toe of the RMB. Friction resistance and turbulence increase the energy dissipation due to decreasing wave reflection and bed scouring, thus adjusting the sediments [1]. Also, Twu et al. (2001) considered wave transmission, wave run-up, and wave motion changes in submerged breakwaters [11]. Neves et al. (2007) observed that the permeability of submerged breakwaters affects the flow characteristics caused by the waves and reduces the horizontal flow velocity [12]. It is also possible to reduce the wave energy by applying submerged obstacles. In a laboratory study, Bungin (2021) used a set of 5 cm cubes with a distance of 1.1 cm in a 100 and 200 cm path as a submerged breakwater and observed that the wave height decreased by 60 to 80% [13]. In addition to protecting the existing breakwater, submerged breakwaters protect shorelines and the facilities. These structures are used for reconstructing the damaged or destroyed RMBs [14]. In a study, Tulsi and Phelp (2009) examined the effect of a submerged breakwater on protecting the crown of a damaged RMB. They found that the submerged structure could break and debilitate the storm waves, save the damaged part of the RMB, and ultimately repair the main RMB [15]. Given the behavior of the submerged obstacle, its application as a structure alongside the RMB seems appropriate. Constructors use precise and essential information such as wave characteristics and structural properties to design this composite structure. It is believed that boosting the breakwaters' optimal performance is viable by modifying the dimensions, wall slope, and position of the submerged structure [16]. In a project, the Stefanutti Stocks (2015) reduced the weight characteristics of the breakwater armor layer by designing a set of the submerged breakwaters to decrease the waves and protect the RMB near the coast [17].

Researchers have always considered innovative methods. For example, He et al. (2012) investigated the combination of pneumatic and submerged breakwaters by considering multiple slope front breakwater based on experimental and numerical models to find the optimal slope [18]. The numerical modeling results by Jian Xu et al. (2020) to analyze the combined effect of submerged and pneumatic breakwaters in reducing the energy of the waves showed a significant increase in energy dissipation capacity by up to 35% compared to the single breakwater [19]. In another study, Qin et al. (2019) numerically modeled submerged breakwaters in one and two rows in the face of regular waves using the fluid-structure interaction (FSI) algorithm and evaluated the second row of breakwaters' use effective [20]. We should know that even in critical situations, using a submerged structure idea next to a RMB is considered. In a project, Quiroga et al. (2018) investigated the effect of using RMB to deal with tsunami waves. Their experiments determined the values of the damage parameter used to describe the damage (onset of damage, onset of destruction, and complete demolition) during a tsunami [21].

This paper is an experimental study highlighting the impacts of a submerged obstacle and a floating wave barrier in front of a RMB using the damage parameter. Therefore, we connected the submerged obstacle to the structure and placed the floating wave barrier at a distance of 50 cm. Under the influence of random waves, we obtained and compared the damage number.

2. Materials and methods

The submerged obstacle in front of the toe prevents rocks from falling, and it acts as a support. The rock fall and the dependence on the submerged obstacle reduce the demolition process, contributing to the RMB stabilization in a smaller area, consequently diminishing the damage parameter. The wave force is the main factor on the RMB, making the breakwater reshape and collapse; decreasing the wave force would reduce its destructive energy by the second power of the wave height. Consequently, the floating wave barrier that resists the waves and reduces their height would be capable of downgrading its destructive power leading to decreased damage parameter. Therefore, comparing the submerged obstacle and the floating wave barrier or their combined effect is of tremendous importance.

2.1. Test procedure

The present experimental study explores the influence of a submerged obstacle attached to the toe and a floating wave barrier at a distance of 50 cm from it on the wave stability of the RMB. In this paper, the toe-connected submerged obstacle is referred to as an obstacle, the floating wave barrier laid at a distance of 50 cm from the RMB, called the wave barrier. Literature review shows that RBM stability has been studied primarily in the lateral or middle sections of the structure. However, the current study applied close-range photogrammetric imaging for providing dense cloud and a combined integrated 3D model of various height elevations to develop a detailed RMB model before and following the wave attacks. In the close-range photogrammetric imaging, the images taken from a close distance were put to analysis for obtaining a reshaped RMB model that could pinpoint the displacement at any point accurately. Since the RMB profile upon encounter with waves did not follow a regular change trend along with the structure, and it constantly changed, some unpredicted changes occur. This issue complicates studies. Well-documented and accurate data leads to better research results contributing to precise measurement of the RMB displacement of armor rocks upon encounter with waves. This method is not destructive and has no adverse effects, and it offers real-time 3D measurements with higher accuracy and speed. In addition, the waves produced by the wave maker were based on the JONSWAP spectrum, which was selected because of its high spectral energy, and in the absence of a field spectrum for laboratory studies can be one of the most appropriate spectra.

2.2. Environmental and structural governing variables

A range of governing variables and non-dimensional characteristics used in this study are listed in Tables 1 and 2. It is believed that wave steepness is the crucial issue to consider for choosing the height and period of the wave. It is essential to take the wave height and period into account to be placed the wave steepness generated by combining the two parameters to stand in the 0.015 to 0.07 range [22]. A combination of wave height and period at a steepness range of 0.01 to 0.054 has been suggested in some studies [23, 24]. The wave height was set to range from 4 to 15 cm based on the laboratory facilities, depth, and the type of wave maker conditions because it is viable to observe scale effects in waves having less than 4 cm height. However, turbulence at the surface of generated waves is expected by the waves with a higher height level at the paddle-generated wave due to large displacements, thus perplexing the accuracy of the data collected. This paper only examined the non-breaking waves. It showed that when the significant wave height surpassed 15 cm during the experiment, the wave could break before striking the breakwater.

Table 1. Range of governing variables

Variable	Expression	Range
Wave height [*cm*]	H_s	9, 12, 15
Wave period [*s*]	T_p	0.9, 1.2, 1.5
Storm duration (Zero up-crossing method)	N	3000
Nominal diameter [*cm*]	D_{n50}	1.7
Mass density [gr/cm^3]	ρ	2.55
Water depth [*cm*]	d_i	25
Slope of breakwater	cot α	1.25
Slope of submerged	cot α_1	1.25

Table 2. Non-dimensional characteristics

Variable	Expression	Range
Ratio of the thickness of armor layer to the nominal diameter	t_A/ D_{n50}	15
Armor material gradation	D_{n85A}/ D_{n15A}	1.82
Wave steepness	s_{om}	0.01 to 0.07
Relative crest width of submerged	B/d	0.4
Relative height of submerged	h/d	0.32

2.3. Wave flume

The tests were done in a 35 m long, 5 m wide, and 1 m deep flume at Soil Conservation and Watershed Management Research Institute (SCWMRI); its features are illustrated in Figures 1 and 2. The wave flume was separated into three parts by two walls of 24.5 meters long and 1 meter high to avoid transverse waves. The waves were produced by a vertical piston generator arm of 5.5 m length and 1 m height positioned at the end of the flume. This wave maker could generate regular and random waves of different spectrums regular and randomly.

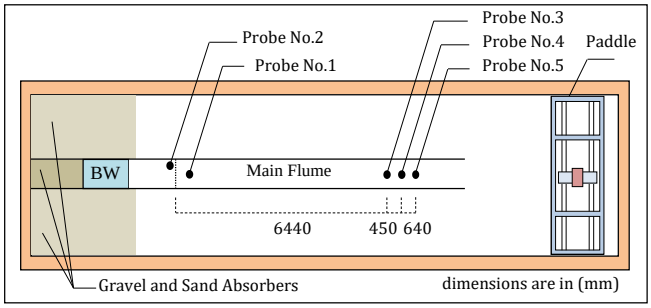

Figure 1. Sketch of wave flume and position of the RMB structure and wave probes

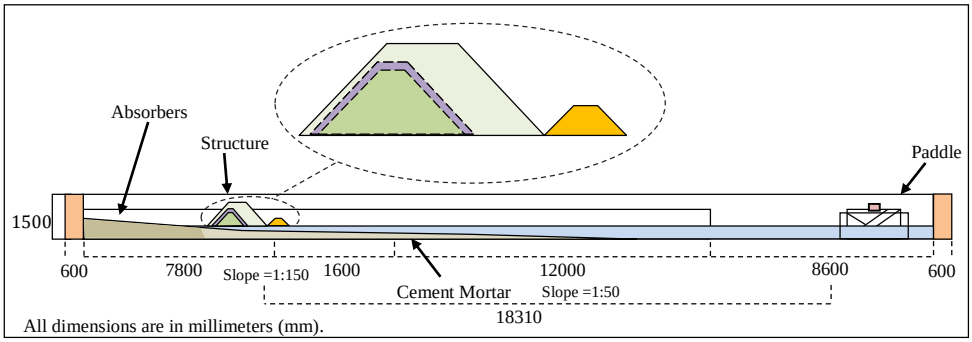

Figure 2. Transversal section of the wave flume and the position of the RMB and the obstacle

The waves generated and used in all experiments were random based on the JONSWAP spectrum. Five wave probes were applied in the flume to log variations of the water surface height with one-millimeter accuracy.

2.4. Breakwater model

The breakwater with a uniform slope of 1V:1.25H is constructed on the flatbed of the flume with primary stone armour of nominal diameter D_{n50} equal to 1.7 cm. A stable obstacle of 80 mm height is designed with plexiglass. The slope of the obstacle is 1V:1.25H, uniformly installed seaward of the RMB. The obstacle is filled with heavy material to submerge entirely and to behave steadier against the waves. Moreover, a wave barrier with dimensions of 100 mm is designed with plexiglass; the weight of this barrier is precisely adjusted to submerge in the water to half of its depth (with 50% immersion) while being held to the flume bed by a wired cable. The white anti-reflective fabric is applied to cover the obstacle to avoid light reflection and errors in imaging and capture the location of points and profiles. The features of RMB, obstacle, and

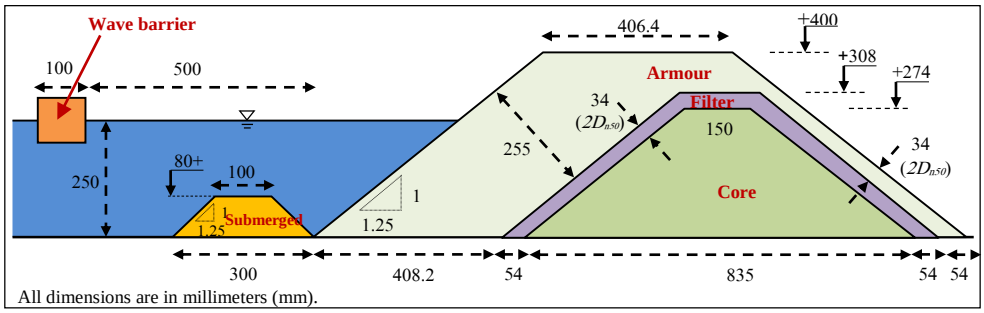

Figure 3. Dimensions and distances of the RMB, obstacle, and wave barrier

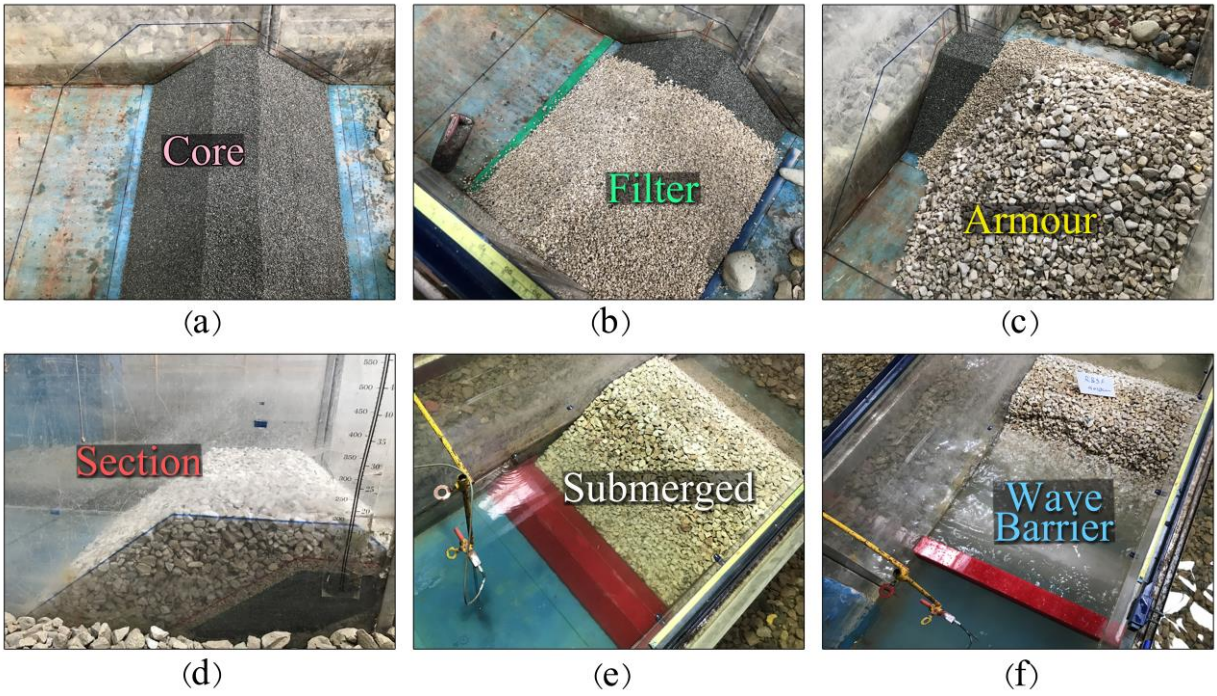

Figure 4. (a) core, (b) filter, (c) armour, (d) Transversal section of the RMB, (e) obstacle, (f) wave barrier

barrier, are shown in Figure 3 and their images in the fabrication and experiment phases in Figure 4.

2.5. Measurements and Data interpretation

Before performing tests, the experimental setup was calibrated and controlled. Some assumptions were also taken into account in tests, e.g., secondary waves in the wave generation process are not considered, flume bed is the horizontal, merely hydraulic performance of the model is considered, and Wave reflection from the breakwater does not encounter with newly generated waves [25]. For making the 3D model, 11 points were first marked on the flume by recording the coordinates of the breakwater range using a surveying camera. Then, before and following tests (or after a certain number of waves), the breakwater was photographed with a professional camera; afterward, images were transferred to software, processed, and digitized to produce photo blocks. Finally, the Digital Elevation Model (DEM) and Digital Surface Model (DSM) were prepared. Some properties of the integrated 3D model specified by the software listed in Table 3.

Table 3. Specifications of the 3D model

Aligned Cameras	GCP (Markers)	Dense Point Cloud	Tie Points	Flying Altitude (m)	Coverage Area (m^2)
27	11	2073622	20471	1.13	2.28

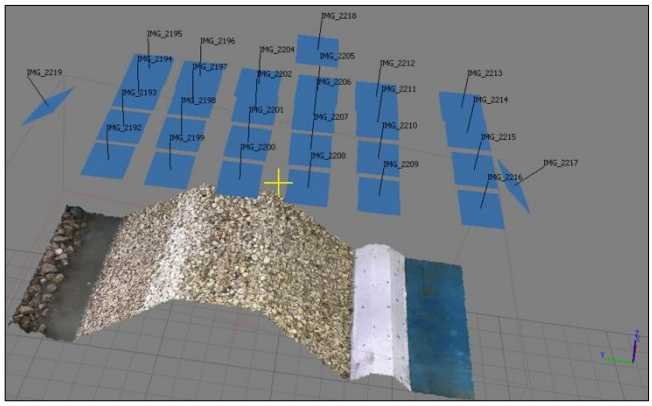

Figure 5. Position of markers and cameras from the RMB

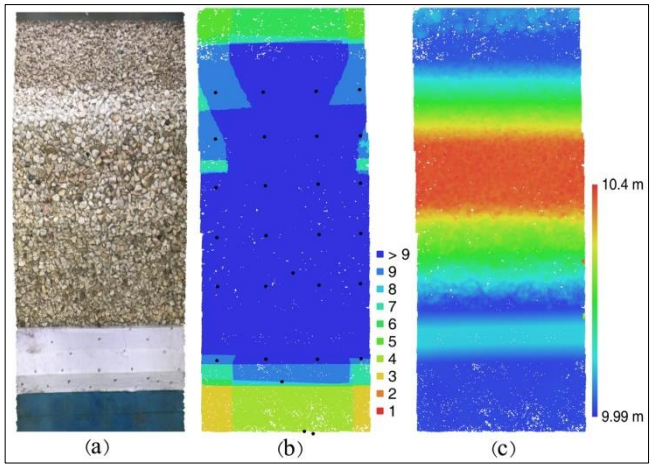

Figure 6. (a) Integrated images, (b) images overlaps, (c) DEM

Images of the structure surface were taken at regular intervals. Around 25 to 27 images were prepared for each test segment and transferred to the software to develop a 3D model. Sample of markers and pictures taken from the breakwater in the AGISOFT is clear from Figure 5. In addition, Figure 6(a) shows a set of images taken, and Figure 6(b) displays the image overlaps; Figure 6(c) demonstrates the DEM.

3. Results and Discussion

Analyzing the test results using the main parameters is an essential issue for studying RMB hydraulic stability.

3.1. Random wave

The wave paddle is of the piston type. The wave maker could produce regular and random waves under the Bretschneider, Pierson-Moskowitz, and JONSWAP spectrum, with the maximum height of generated wave standing at 20 cm. The wave probes are based on resistance detectors, and they could accurately measure the water surface fluctuations regarding the static water surface. The wave height was obtained for every solo wave using the time series harvested via the zero up-crossing methods. In this method, the wave intercepts with the reference line (water surface elevation) in two points. The wave height is the maximum difference of water surface elevation between two solid points and the wave period is the time interval from the first solid point to the second one [26]. Accordingly, a code was prepared in MATLAB and used water surface time series to differentiate the waves and provide the height and periods of the individual waves. The maximum height, significant wave height, average wave height, maximum period, significant wave period, average period, wavelength, and frequency were calculated from the resultant height and periods. The JONSWAP spectrum and the experimental spectra are shown in Figure 7. Based on the results, the wave height and period through the zero up-crossing results do not match the observed values. However, from among the three mean, significant, and max wave heights and periods, the significant mode was closer to the height and period of the wave maker. This case can also be observed in both the JONSWAP spectrum created by the wave maker at the water surface and the results of the wave separation code. For example, considering the wave height of 12 cm defined for the wave maker, the wave heights under mean, significant, and maximum mode were 5.3, 11.38, and 15.59 cm, respectively. All performed tests verified this finding.

Consequently, the height and period defined for the wave maker can be approximated as the significant height and period. The number of waves generated from the water surface was also lower than the expected figure. For example, at a wave height of 12 cm, a period of 1 second, and a duration of 5400 seconds (1.5 hours), 5400 single waves were expected to be generated, while the zero up-crossing method results would offer 5173 waves. This reduction happens because the water surface transfers to the next wave without cutting the

zero level in tiny waves. That wave is being practically eliminated in counting the waves. According to tests, the discrepancy between these two numbers regarding the effect of the number of waves on the RMB reshaping was not significant as it was controlled for experiments.

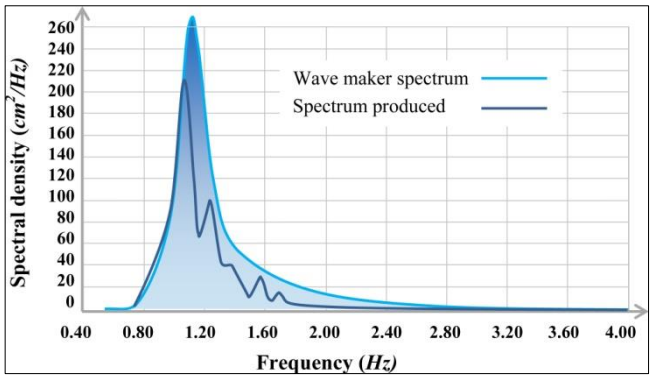

Figure 7. JONSWAP spectrum and experimental spectra

3.2. Reshaping profiles

At the beginning of the experiments, RMB (as the control test) was subjected to random waves for observing the performance of the obstacle and the wave barrier accurately. Moreover, the reshaping of armor in different heights and periods was studied so that the controlled structure against the waves would determine the damage to the RMB realistically and accurately. By the damage parameter, it is meant: ($S=\frac{Ae}{D_{n50}^2}$), Where A_e is the eroded area and D_{n50} the nominal diameter of the armor layer. The reshaping of the armor rocks and the final profile of the structure is depicted in Figure 8. The level of displaced material as the average value (average variations in 8 bands) is shown in Figure 9. Figure 10 shows a DEM of the breakwater and a transversal section through the middle of the structure. Also, a side view of the section before and after the test is shown in the figure. Since numerous images are available, the shapes were not repeated for all tests in

Figure 8. Top view, side view, and bird's-eye view before and after the test

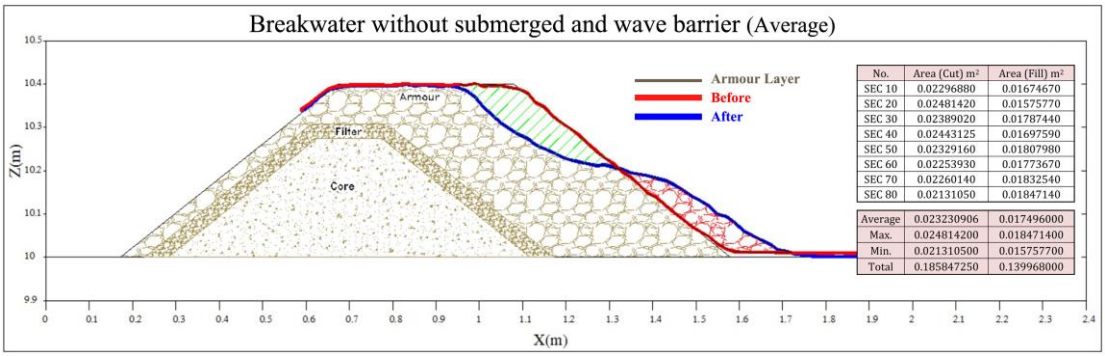

Figure 9. Average area of displaced rocks and profile reshaping

this study.

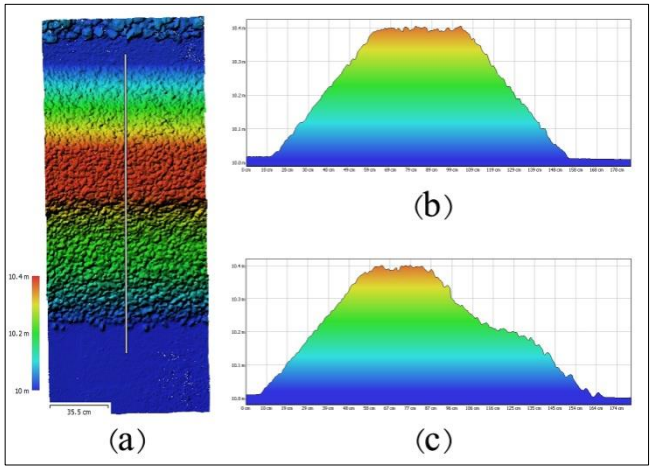

Figure 10. (a) DEM and transversal section (b) Selected section before the test (c) Selected section after test

3.3. The effect of wave characteristics on RMB reshaping

Following the tests, height, period, and the number of waves (storm duration) parameters were assessed as the primary characteristics influencing the structure's stability and monitoring the erosion when the obstacle was connected to the RMB. For studying the stability trend, the RMB was tested at the height of 12 cm and a period of 1 second with several incident waves ranging from 1000 to 6000. Results are demonstrated in Figure 11. The damage parameter was calculated by S ($S=\frac{Ae}{D_{n50}^2}$) for each test; as shown, the maximum profile change (over 50%) happened when the first 1000 waves hit, and the erosion of the armor layer followed an increasing trend up to 3000 waves; the erosion pace significantly decreasing between 3000 and 4000 waves. Note that erosion is considered practically insignificant from 4000 to 6000 waves. Therefore, since the erosion and reshaping of the RMB profile surpassed 90% of the absolute limit (6000 waves) when 3000 waves hit the structure section, the time at which 3000 waves were hit is considered as the equilibrium time, with the 3000 waves taken to be the constant value in physical models. After the stones of the armor layer started to fall and the breakwater section initially reshaped (1000 waves), the wall slope becomes milder upon encountering with remaining waves. Profile change and rock fall gradually led to more surface contact and erosion in the wave energy absorption process resulting in increased wave energy absorption and reduced reflection coefficient of the structure. As Figure 11 shows, the reshaped profiles are influenced by incident waves for a fixed combination of wave height and period. Figure 12 shows the variation of the damage parameter along with the number of waves radiated.

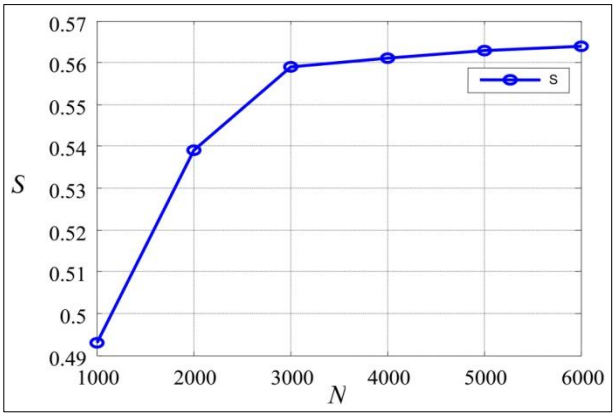

Figure 12. Damage parameter variations with different number of waves

Waves with 9, 12, and 15 cm height were generated by a paddle towards the RMB under a constant period (1 second) to study the effect of different wave heights on the erosion rate of the structure. The erosion rate and the profile reshaping were logged during the effective storm (3000 waves). Figure 13 plots the (non-dimensional) damage parameter against the non-dimensional wave height selected from among the numbers $\frac{H}{g.T^2}$, $\frac{H}{d}$ and $\frac{H}{H_{max}}$ (H: wave height, d: water depth, g: gravitational acceleration and T: wave period). This parameter was selected because the period is fixed due to the limited number of tests, so the choice of T could not be logical. Also, the number of wave chosen heights was 3; the maximum selection of the values could not generalize the height of multiple waves. The relationship between non-dimensional wave height and damage parameter was calculated from a linear fit with a regression coefficient of 0.99, as$S = 1.936(\frac{H}{d}) - 0.363$. Due to the low number of

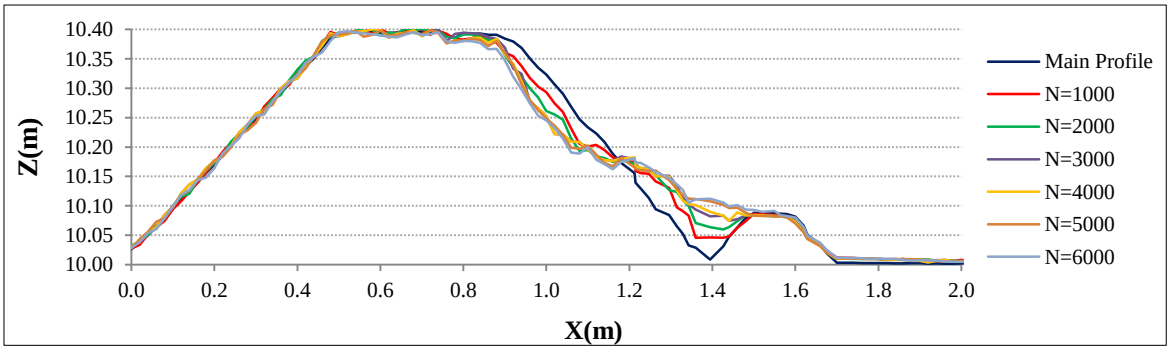

Figure 11. Comparison of the final profile reshaping of RMB under wave tests

points, this equation could not be generally used, as it was merely a preliminary estimation. Table 4 illustrates the numbers of relative wave height (wave height over water depth) and the damage parameter. As shown, the damage parameter increased by 39.12, and 44.44%, respectively, by increasing the relative wave height from 0.36 to 0.48 and 0.6. At a wave height of 15 cm, wave overflow from the breakwater was noticeable; thus, the wave height of 12 cm was used in physical models.

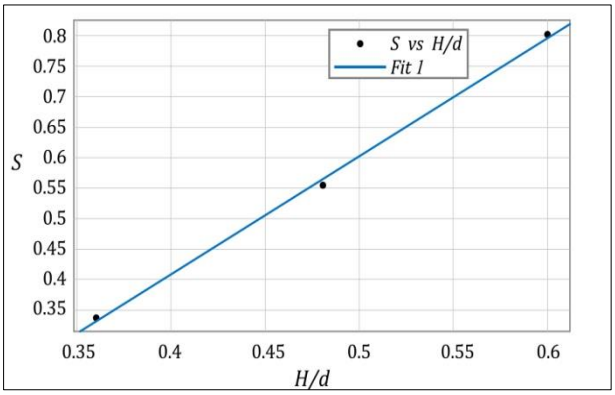

Figure 13. Variation of Damage parameter with wave height

Table 4. Relative wave height and damage parameter

H /d	0.36	0.48	0.60
S	0.3384	0.5560	0.8031

According to our analysis, as a parameter influencing the RMB stability, the wave period verified that erosion, at a constant wave height, increased by increasing wave period. Table 5 shows the relative wave period numbers (period over the maximum period) and damage parameters. These numbers indicate that as the relative wave period grows from 0.6 to 0.8 and 1, damage parameters increased by 22.94 and 28.26%. Thus, increasing the period would increase the damage parameter; nonetheless, increasing the wave height would have a more significant effect. In the wave period of 0.9 seconds, the wave steepness was high; it was sometimes noted that the wave would break before the wave strike the breakwater; whereas for the wave period of 1.5 seconds, the number of incident waves would decrease at a certain time. Consequently, the wave period of 1.2 cm was used in physical models.

Table 5. Relative wave period and damage parameter

T/ T_{max}	0.6	0.8	1
S	0.4284	0.5560	0.7131

3.4. Physical models

Tests performed in the research are shown in Table 6.

Table 6. Performed tests

Test	**RMB arrangement modes with obstacle and wave barrier**
RB	RMB without obstacle and wave barrier
RBS	RMB with connected obstacle without wave barrier
RBF	RMB with wave barrier at 50 cm without obstacle
RBSF	RMB with connected obstacle and wave barrier at 50 cm

Figure 14 shows the reshaped profile of the RMB at each transversal section for the RBSF experiment altogether. Imaging results provide a 3D reshaping; besides, by sectioning each image, the eroded area (A_e) and the damage parameter are determined. Figure 15 compares the reshaped RMB profile in all test conditions. Table 7 demonstrates damage parameters in sections, height, period, and the number of waves calculated based on the experiments. In this table, H_{wm} is the wave height defined for the wavemaker, H_s, significant wave height taken from the water surface, T_{wm}, wave period specified for the wave maker, T_s, significant wave period taken from the water surface, N, the number of waves expected and N_{pr} the number of waves taken from the water surface. As Table 7 shows, the damage parameter of the RMB under random waves is 1.116. As shown in the table, the highest damage parameter pertained to the 20-cm section of the wall due to the wave behavior's complexity when hitting the breakwater, and waves also causing lateral motion upon hitting the coarse armor layer rocks. Moreover, due to the flow turbulence in this area, irregular motions are noted in the armor layer; thus, the accurate estimation is not possible by simply selecting a breakwater section for studying the stability, and more sections should be considered for a better assessment.

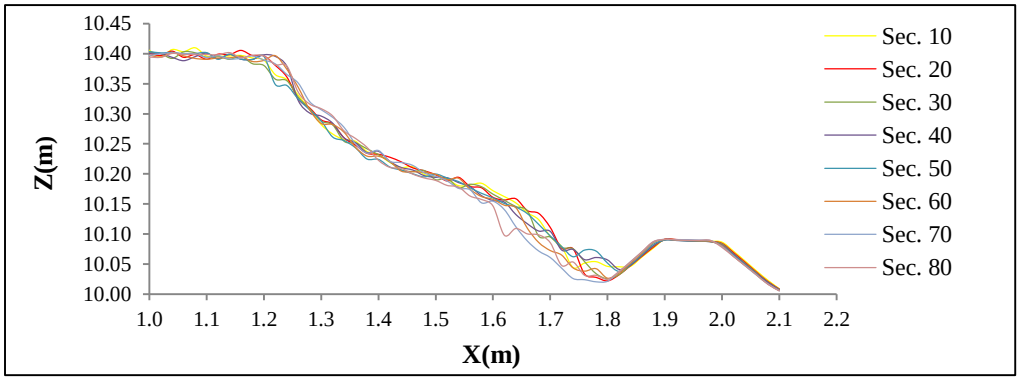

Figure 14. Reshaped RMB profile at each transversal section

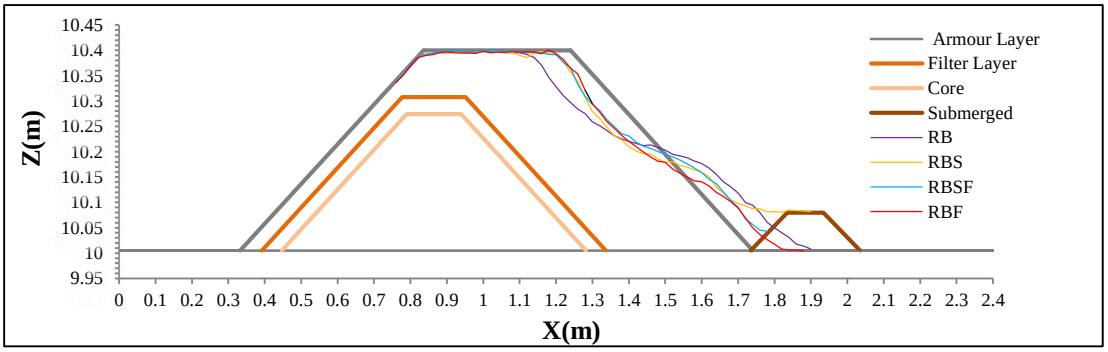

Figure 15. Reshaped RMB profiles in all tests

Table 7. Damage parameter in sections, height, period, and number of waves calculated in tests

	H (cm)		T (s)		N		S									
	H_{wm}	H_s	T_{wm}	T_s	N_0	N_{pr}	S_{10}	S_{20}	S_{30}	S_{40}	S_{50}	S_{60}	S_{70}	S_{80}	S_{max}	$S_{min(Final)}$
RB	12	11.52	1	0.95	3000	2783	1.033	**1.116**	1.075	1.099	1.048	1.014	1.017	0.959	**1.116**	
RBS	12	11.29	1	0.96	3000	2953	0.626	0.574	0.572	**0.701**	0.699	0.698	0.660	0.516	**0.701**	
RBF	12	11.29	1	0.94	3000	2709	0.549	0.629	0.667	0.628	0.601	0.576	**0.735**	0.503	**0.735**	**0.538**
RBSF	12	11.59	1	0.97	3000	2787	0.502	0.486	0.443	0.485	0.472	**0.538**	0.433	0.480	**0.538**	

As seen in table 7, the damage parameter was reduced by applying the obstacle to 0.701 (i.e., 37.19%), while the wave barrier reduced the damage parameter to 0.735 (i.e., 34.14%). Thus, the obstacle has outperformed the wave barrier. Using the obstacle with the wave barrier simultaneously reduced the damage parameter by 51.79%. Physically, it can be assumed that support was established for the breakwater when using the obstacle attached to the structure, which was effective against slides and overturning, with some of the eroded segments hitting it and stopping there. The simultaneous use of the obstacle and the wave barrier results in the highest efficiency, with the reduced-energy wave hitting the existing RMB with the obstacle. Seemingly, a reduced damage parameter by 51.79% would reduce RMB dimensions, significantly reducing the costs.

4. Conclusion

Based on the results of this study, the following conclusions have been drawn regarding the effect of a submerged obstacle and floating wave barrier in front of RMB diminishing the damage parameter:

- Using close-range photogrammetric imaging and developing 3D integrated models of breakwater profile changes has been an effective method for estimating the damage parameter in RMBs.
- Tests showed that the maximum profile change (over 50%) happened when the first 1000 waves hit. The erosion of the armor layer followed an increasing trend of up to 3000 waves, followed by the erosion pace between 3000 and 4000 waves decreasing. Besides, the erosion was found to be practically insignificant from 4000 to 6000 waves.
- Since the erosion and the breakwater profile change surpass over 90% of the absolute limit when 3000 waves hit the structure, increasing the wave height would increase the damage parameter. According to test results, damage parameters increase by 39.12 and 44.44%, respectively, by increasing the relative wave height from 0.36 to 0.48 and 0.6.
- In addition, increasing the period would increase the damage parameter; as the relative wave period expands from 0.6 to 0.8 and from 0.8 to 1, the damage parameter increase by 22.94 and 28.26%, respectively.
- Based on the results, the damage in transversal sections is different, and the middle band cannot be suggested for the stability study.
- Using the obstacle reduces the damage parameter to 0.701 (i.e., 37.19%), while the wave barrier reduces this parameter to 0.735 (i.e., 34.14%).
- The simultaneous use of the obstacle and the wave barrier results in the highest efficiency. Obviously, a reduced damage parameter by 51.79% would reduce RMB dimensions, significantly reducing the costs.
- Continuing studies of this research and future suggestions, changes in other parameters such as the RMB dimensions, the submerged obstacle dimensions, or the distance of the floating barrier can be examined.

5. References

[1] Khosravi Babadi, M., Golshani, A., Ghanei Ardakani, A. and Karami Matin, A., (2017), *Design principles of breakwaters*, Marine Industries Organization, p.17-23-42-111.

[2] Ghanbarian, M., (2010), *Rubble mound breakwaters (Vol.1: Types of breakwaters, principles, and overview*, Khatam al Anbiya Construction Headquarter, p.15-19. (In Persian)

[3] Sayao, O. and Da Silva R. F., (2016), *Analysis of rubble mound breakwater damage: Case study of existing breakwater rehabilitation*, IX Pinac Copedec Conference.

[4] Lamberti, A., Tomasicchio, G.R. and Guiducci, F., (1994), *Reshaping breakwaters in deep and shallow water conditions*, Proceeding of 24th International Conference on Coastal Engineering, Kobe, Japan. ASCE. p.1343-1358.

[5] Mousavi, Sh., (2010), *Rubble mound breakwaters (Vol.2: Design of rubble mound breakwaters*, Khatam al Anbiya Construction Headquarter, p.15-19-93-100-105. (In Persian)

[6] Campos, A., Castillo, C. and Sanchez, R.M., (2020), *Damage in rubble mound breakwaters. Part I: Historical review of damage models*, Journal of Marine Science and Engineering, Vol.8(5):317.

[7] Sayao, O., (1998), *On the profile reshaping of berm breakwaters*, Coastal structures, Vol.99, p.224-265.

[8] Rao, S. and Pramod, rao, B., (2003), *Stability of berm breakwater with reduced armour stone weight*, Ocean Engineering, Vol.31, p.1577-1589.

[9] Panagiota, G., Christos, M., and Panayotis, P., (2018), *Optimized reliability based upgrading of rubble mound breakwaters in a changing climate*, Journal of Marine Science and Engineering, 6(3):92.

[10] Janardhan, P., Harish, N., Rao, S. and Shirlal, K.G., (2015), *Performance of variable selection method for the damage level prediction of reshaped berm breakwater*, ICWRCOE 2015. Aquatic Procedia Vol.4, p.302- 307.

[11] Twu, S.W., Liu, C.C. and Hsu, W.H., (2001), *Wave damping characteristics of deeply submerged breakwaters*, ASCE Journal of Waterway, Port, Coastal, and Ocean Engineering Vol.127 (2), p.97–105.

[12] Neves, A.C., Veloso Gomes, F.and Taveira Pinto, F., (2007), *Analysis of the wave-flow interaction with submerged breakwaters*. WIT Transactions on Modelling and Simulation. Vol.46, p.147-154.

[13] Bungin, E.R., (2021), *The effect of square submerged breakwater on wave transmission in the coastal area*, AC2SET (2020), IOP Conference series: Materials Science and Engineering.

[14] Juhl, J. and Jensen, O. J., (1995), *Features of berm breakwaters and practical experience. Proceeding of the International Conference on Coastal and port engineering in developing countries*, R.J. Brazil. p.1307-1320.

[15] Tulsi, K., and Phelp, D., (2009), *Monitoring and maintenance of breakwaters which protect port entrances*, proceeding of the 28th South African transport conference, p.317 – 325.

[16] Smith, D.A.Y., Warner, P.S. and Sorensen, R.M., (1996), *Submerged-crest breakwater design, advances in coastal structures and breakwaters*, Thomas Telford, London, p.208–219.

[17] Stefanutti Stocks Marine, (2015), *Rubble mound breakwater vs. tandem breakwater cost estimation. Cape Town*, Stefanutti Stocks Marine.

[18] He, F., Huang, Z. and Law, A.W., (2012), *Hydrodynamic performance of a rectangular floating breakwater with and without pneumatic chambers: An experimental study*, Ocean Engineering, Vol.51 (1), p.16-27.

[19] Jian Xu, T., Wang, X.R., Guo, W.J., Dong, .H. and Hou, H.M, (2020), *Numerical simulation of combined effect of pneumatic breakwater and submerged breakwater on wave damping*, Taylor and Francis: Ships and offshore structures.

[20] Qin, H., Mu, L., Tang, W. and Hu, Z., (2019), *Numerical study of the interaction between peregrine breather based freak waves and twin-plate breakwater*, Journal of Fluids and Structures, Vol.87, p.206-227.

[21] Quiroga, I., Vidal, C., Lara, J., Gonzalez, M. and Sainz, A., (2018), *Stability of rubble-mound breakwaters under tsunami first impact and overflow based on laboratory experiments*, Coastal Engineering, Vol.135, p.39-54.

[22] Van der Meer, J.W., (1993), *Conceptual design of rubble mound breakwaters*, Delft Hydraulics, Report No. 483.

[23] Andersen, T.L., (2006). *Hydraulic response of rubble mound breakwaters (scale effects-berm breakwaters)*, University of Alborg, Denmark.

[24] Burcharth, H.F., (1993), *Design of breakwaters*, Department of Civil Engineering, Alborg University Denmark.

[25] Ataie Ashtiani, B., (2006), *Coastal engineering (Coastal hydrodynamics)*, ACECR, Amirkabir University of Technology Branch, p.214-215-218. (In Persian)

[26] Vafaeipour Sorkhabi R, Naseri A (2015) *Experimental investigation of the interaction between vertical flexible seawall and random sea waves.* Journal of Advanced Defense Science and Technology 6(3): 155-162. (In Persian)

INTERNATIONAL JOURNAL OF
COASTAL, OFFSHORE & ENVIRONMENTAL ENGINEERING IJCOE Vol.7/No. 2/Spring 2022 (49-54)

Available online at: www. Ijcoe.org

Numerical modeling of underwater acoustic wave using Differential Quadrature Method

Abolfazal Delbari[1], Ali Sheykhbahaei[2*]

[1]Department of Physical Oceanography, Faculty of Marine Science, Khorramshahr University of Marine Science and Technology, Khorramshahr, Iran, abolfazl_delbari@yahoo.com
[2] Department of Nonliving Resources of Atmosphere and Ocean, Faculty of Marine Science and Technology, University of Hormozgan, Bandar Abbas, Iran Abbas, Iran, ali.sheykhbahai@gmail.com*

ARTICLE INFO

Received: 10 Sep. 2021
Accepted: 1 Mar. 2022

Keywords:
Acoustic Wave Propagation
Differential Quadrature Method
Numerical Modeling

ABSTRACT

In this paper underwater acoustic wave propagation is studied numerically by Differential Quadrature method. Numerical methods are different with respect to accuracy. computer costs and practical flexibility. In this study Differential Quadrature (DQ) method is applied for numerical solution of underwater acoustic wave for first time. Two experimental cases are used to validate the two-dimensional wave model. first the numerical results are verified by analytical solution and the second one showed the applicability of current method in complex domain. Comparisons demonstrate the efficiency. accuracy and robustness of the Differential Quadrature method for acoustic wave simulation.

1. Introduction

During the recent two decades studies on the mathematical modeling of underwater acoustic wave propagation have been established. Numerous techniques have been used in the past to model acoustic wave propagation. As indicated by [1] most of these methods can be classified as Ray methods. Normal Mode methods and Parabolic Equation methods. The present study focuses on the mathematical modeling of underwater acoustic propagation over irregular bottom topography with Parabolic Equation methods.

Different numerical methods that have been applied to solve acoustic wave equation[2,3]. Costa et al. developed a numerical model to simulate the 2D acoustic wave propagation in the vicinity of an underwater configuration which combines two sub-regions using the Boundary Element Method and the Method of Fundamental Solutions[4]. Murphy and Chin-Bing applied the finite element method to produce a full-wave range-dependent scalar ocean acoustic propagation model[5]. Keiswetter et al. developed a program which uses finite-difference techniques to approximate the solution of the two-dimensional heterogeneous acoustic wave equation[6].

In this study a Differential Quadrature (DQ) Method is applied for the first time to solve the acoustic wave equation. Bellman et al. introduced DQ numerical method as a simple and highly accurate numerical technique[7]. which approximates the derivatives of function using a weighted sum of all the functional values along the orthogonal axis. Shu developed the weighting coefficient as a high-order polynomial that can be computed by the Lagrange polynomial interpolation with a recurrence relationship[8]. From the literature review. numerical solution by the DQ method can be very precise using a simple mesh system with a high-order polynomial employed. However, due to the geometric relationship of the wanted and the referenced nodes. the DQ method cannot be applied directly to irregular-domain problems. Shu and his colleagues proposed a domain-free discretization method to try to improve this disadvantage [9,10]. Nevertheless. the domain-free discretization method involves some points which may not be mesh nodes in the physical domain. and the physical values at these points require an interpolation/extrapolation scheme to be obtained. Such a technique will introduce an additional error near the boundaries.

Meanwhile. solution of the acoustic wave equation in a large domain obtained a large system of linear equations which should be solved simultaneously because of the nature of an elliptic boundary value problem. Therefore direct methods like Gauss elimination for solving a system of linear equation require huge storage and CPU time. For this purpose

the iterative scheme would be the best choice. In this study Conjugate Gradient (CG) iterative method is applied to guarantee convergence of solving the linear system of equations that was used by several researchers in the literature [11].

2. Mathematical Problem Statement

2.1. Governing Equation

In the vertical plane (x.z) for homogeneous harmonic two-dimensional problems. with assuming ideal fluid theory and constant sound velocity c. the complex velocity potential is defined as

$$\varphi(\mathrm{x.z.t}) = \phi(\mathrm{x.z})exp(-j\omega t) \tag{1}$$

where ω is the acoustic wave frequency. ϕ is the complex potential amplitude($\mathrm{j} = \sqrt{-1}$).
The wave equation then reduces to a Helmholtz equation in domain Ω

$$\nabla^2\phi + k^2\phi = -\sum_{i=1}^{N_S} S_i\delta\left(x_{S_i}, z_{S_i}\right) \text{ in } \Omega \tag{2}$$

$$\nabla^2\phi + k_0^2 n^2\phi = -\sum_{i-1}^{N_S} S_i\,\delta(x_{S_i}, z_{S_i}) \tag{3}$$

Where $k_0 = w/c_0$ is the reference wave number.

$$n = [c_0/c](1 + i\frac{BETA}{54.575054}) \tag{4}$$

is index of refraction.(BETA=attenuation (dB/wavelength) and S_i are values denote (potential) strengths of N_s point sources at locations $\left(x_{S_i}, z_{S_i}\right)$ (Fig. 1).

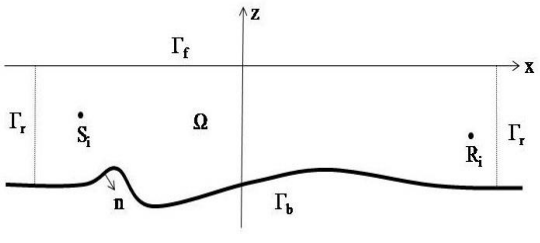

Figure 1. Schematic of underwater acoustic wave propagation domain

The relation between acoustic pressure and complex potential amplitude is

$$p(x,z) = \rho\omega^2\phi(x,z) \tag{5}$$

2.2. Boundary Conditions

For solving acoustic wave propagation appropriate boundary condition must be specified along boundary domain. The bottom is assumed rigid. hence; a no-flow condition applies

$$\frac{\partial\phi}{\partial n} = 0 \text{ on } \Gamma_b \text{ and } \Gamma_{b_i} \text{ (i = 1.2)} \tag{6}$$

At the steady free surface. assuming atmospheric pressure p = 0. we obtain from the linearized Bernoulli equation

$$p = -\rho\frac{\partial\phi}{\partial t} = j\omega\rho_0\phi = 0 \tag{7}$$

with ρ_0 the fluid density. i.e. with no wave present. $\phi = 0$ on Γ_f and Γ_{f_i} (i = 1.2)
On open boundaries. Γ_{r_i} (i = 1. 2). a radiation condition is specified such that the potential and its normal gradient are continuous from inside the computational domain to outside

$$\phi^i = \phi \text{ on } \Gamma_{r_i} \text{ (i = 1.2)} \tag{8}$$

$$\frac{\partial\phi^i}{\partial n} = \frac{\partial\phi}{\partial n} \text{ on } \Gamma_{r_i} \text{ (i = 1.2)} \tag{9}$$

3. Numerical Descretization

3.1. Differential Quadrature Descretization

Differential quadrature is characterized by approximating the derivatives of a function using a weighted linear sum of all the functional values along the orthogonal axis.

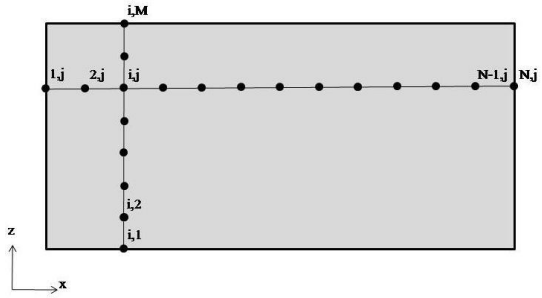

Figure 2. DQM domain descritization and point relationship

Therefore as shown in Fig.2. if the black point is a referenced point then it's derivative with respect to x (or y) direction is approximated by weighted linear sum of gray (or white) point function values that spread in all the problem

domain. Then the DQ descretization of two-dimensional problem domain ($N \times M$) at any location (x_i, y_j) the n_{th} order derivative of a function $f(x,y)$ with respect to x and y can be approximated by

$$\frac{\partial^n f(x_i, y_j)}{\partial x^n} = \sum_{k=1}^{N} w_{i,k}^{(n)} f(x_k, y_j) \quad (10)$$

$$\frac{\partial^n f(x_i, y_j)}{\partial y^n} = \sum_{k=1}^{M} w_{j,k}^{(n)} f(x_i, y_k) \quad (11)$$

respectively. for $i = 1,2,...,N$ and $j = 1,2,...,M$ Where $w^{(n)}$ is the weighing coefficient of n_{th} order derivative. Based on Shu's general approach. the explicit formulas for the first order weighting coefficients for x direction are

$$w_{i,j}^{(1)} = \frac{\prod_{k=1,\, k\neq i}^{N} (x_i - x_k)}{(x_i - x_j) \cdot \prod_{k=1,\, k\neq j}^{N} (x_j - x_k)}, \qquad for \quad i \neq j \quad (12a)$$

$$w_{i,i}^{(1)} = -\sum_{j=1,\, j\neq i}^{N} w_{i,j}^{(1)} \quad (12b)$$

Also for the second order derivative weighting coefficient of Shu's general approach is:

$$w_{i,j}^{(2)} = 2w_{i,j}^{(1)} \cdot \left(w_{i,i}^{(1)} - \frac{1}{x_i - x_j} \right), \qquad for \quad i \neq j \quad (13a)$$

$$w_{i,i}^{(2)} = -\sum_{j=1,\, j\neq i}^{N} w_{i,j}^{(2)} \quad (13b)$$

Similarly for y direction. weighting coefficients are computed for first and second order by replacing M instead of N and y instead of x.

However the DQ interpolation needs the function value on the whole domain. so the solution domain must be regular. The governing equation of wave propagation descretization by DQ method obtains

$$\frac{\partial^2(\varphi)}{\partial x^2} + \frac{\partial^2(\varphi)}{\partial y^2} + k_0^2 n^2 \varphi = -\sum_{i=1}^{N_S} S_i \delta(x_{S_i}, z_{S_i}) \quad (14)$$

Finally the MSE descretization by DQ method is written as:

$$\sum_{k=1}^{N} wx_{i,k}^{(2)} \varphi_{k,j} + \sum_{k=1}^{M} wy_{j,k}^{(2)} \varphi_{i,k} + k_0 n_{i,j}^2 \varphi_{i,j} = -\sum_{i=1}^{N_S} S_i \delta(x_{S_i}, z_{S_i}), \quad i = 1,2,...,N, \quad j = 1,2,...,M \quad (15)$$

4. Solution Method

By applying the discrete acoustic wave equation (equation 13 and 18) on all of the grid points in the problem domain. a large system of linear equations is obtained and it should be solved simultaneously over the whole domain.

$$[A]\{\varphi\} = \{b\} \quad (16)$$

where $[A]$ is an $(M \times N)^2$ complex matrix. and $\{b\}$ is an $(M \times N)$ vector. For solution of system of linear equations Conjugate Gradient (CG). the iterative scheme that proposed by Xu was applied to guarantee convergence of solving the linear system of equations[12]. Whereas the coefficient matrix $[A]$ is not diagonally-dominant. nor symmetric and positive definite. but for conjugate gradient iterative procedures matrix $[A]$ needs to be diagonally-dominant or symmetric and positive definite. so the following Gauss transformation that recommended by Panchang is applied to equation (16)[13].

$$[A^*][A]\{\varphi\} = [A^*]\{b\} \quad (17)$$

where $[A^*]$ is the complex conjugate transpose of $[A]$. Clearly $[A^*][A]$ is Hermitian and positive-definite matrix that is suitable for CG iterative scheme. The algorithm that is presented by Xu [12] is as follows:

Step 1. Select trial values $\{\varphi_0\}$ (i.e. 0^{th} iteration) for all nodes in the model domain where the solution is desired.

Step 2. Compute for all points $\{r_0\} = \{f\} - [A]\{\varphi_0\}$ and $\{p_0\} = [A^*]\{r_0\}$.

Step 3. Compute for the i^{th} iteration

$$\alpha_i = \frac{\| [A^*]\{r_i\} \|^2}{\| [A]\{p_i\} \|^2} \quad (18)$$

Step 4. Update $\{\varphi_{i+1}\} = \{\varphi_i\} + \alpha_i \{p_i\}$ for all points.

Step 5. Check for convergence of the solution. The criterion for convergence is

$$\frac{\left\| [A]\{\varphi_{i+1}\} - \{f\} \right\|^2}{\left\| \{\varphi_{i+1}\} \right\|^2} \prec \varepsilon \quad (19)$$

Where ε is a prescribed tolerance. If it is true. stop.
Step 6. Compute. for each grid point

$$\{r_{i+1}\} = \{r_i\} - \alpha_i [A]\{p_i\} \quad (20)$$

Step 7. Compute for the i[th] iteration

$$\beta_i = \frac{\left\| [A^*]\{r_{i+1}\} \right\|^2}{\left\| [A^*]\{r_i\} \right\|^2} \quad (21)$$

Step 8. Compute $\{p_{i+1}\} = [A^*]\{r_{i+1}\} + \beta_i \{p_i\}$.
Step 9. Set $i = i + 1$. and go to step 3.

5. Numerical Example (Model Verification)

In order to assess the computational efficiency and accuracy of LDQ method. two numerical examples are considered to validate the model. First example was acoustic wave propagation in rectangular domain which has an analytical solution and second was a wedge-shaped ocean appeared among the range-dependent benchmark solutions solicited by the Acoustical Society of America in 1987.

5.1. Example 1: Acoustic wave propagation in rectangular domain

This example has analytical solution and can be an appropriate case for validation of numerical modeling of the acoustic wave propagation with DQM. Numerical domain was showed in Fig. 3 in which $\Gamma 1. \Gamma 2$ and $\Gamma 3$ are rigid boundaries and $\Gamma 1$ is uniform potential boundary.

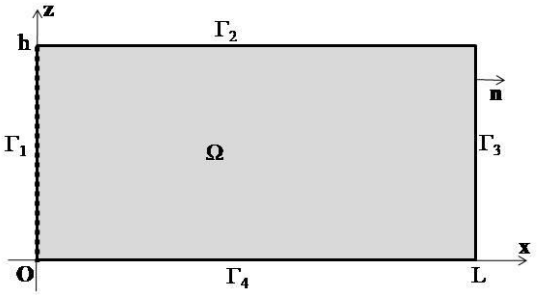

Figure 3. Example 1 domain geometry (L = 1 and h = 1)

$$\bar{\emptyset}(0.z) = \frac{1}{\omega\rho_0} cot(kL)\ for\ \{x = 0; 0 \le z \le L\} \quad (22)$$

$$\frac{\partial\bar{\emptyset}}{\partial n} = 0 \quad for \begin{Bmatrix} z = h; 0 \le x \le L \\ x = L; 0 \le z \le h \\ z = 0; 0 \le x \le L \end{Bmatrix} \quad (23)$$

where h is the domain height and L is the domain length. The problem has an exact solution given by.

$$\bar{\emptyset}(x.z) = \frac{1}{\omega\rho_0}\left\{sin(kx) + \frac{cos(kx)}{tan(kL)}\right\} \quad (24)$$

Fig. 4 shows the DQM solution of the acoustic wave propagation in the rectangular domain. Also. numerical result is compared with analytical solution in Fig 5. These figures show the accuracy of DQM numerical modeling by using small number of points for domain descritization.

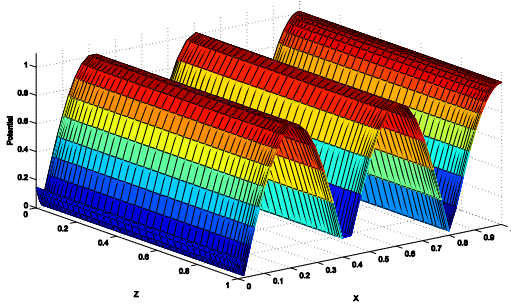

Figure 4. Numerical solution of acoustic wave equation in rectangular domain

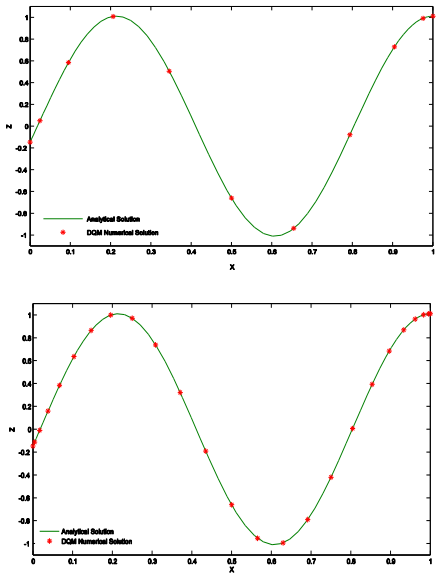

Figure 5. Comparison between DQM numerical results and analytical solutions

5.2. Example 2: Acoustic wave propagation in a wedge-shaped ocean

In this example applicability of DQM numerical modeling was studied in the more complex domain. The geometry domain was shown in Fig. 6. As shown in the figure a 25-Hz continuous wave source was located at zero range and mid depth in 200 m of water and the bottom slope was 1/20. Pressure receivers were located at depth of 30 and 150 m in horizontal arrays.

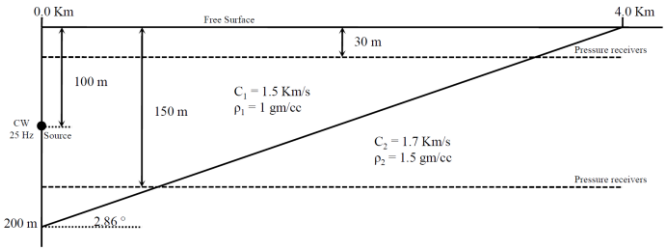

Figure 6. Acoustic wave propagation in a wedge-shaped ocean geometry

The solution for this problem appears in Fig. 7 which compares DQM numerical results with the F.B. Jensena & C.M. Ferla Benchmark data. The agreement is very good for the 30 m depth receivers and satisfactory for the 150 m receivers. These results demonstrated the accuracy and applicability of DQM numerical model for underwater acoustic wave propagation.

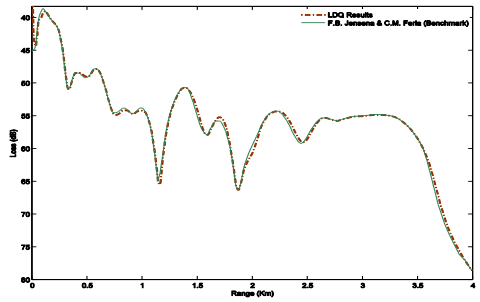

(a)

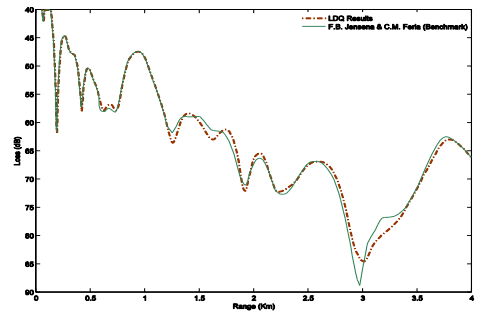

(b)

Figure 7. Numerical results of Acoustic wave propagation in a wedge-shaped ocean. a) for 30 m receivers b) for 150 m receivers

Well-known evaluation criteria were used to assess the performance of DQM compared to other numerical and experimental data.
The index of agreement is another usual evaluation criteria (Willmott. 1982).

$$d = 1 - \frac{\sum_{i=1}^{N_c}(P_i - O_i)^2}{\sum_{i=1}^{N_c}\left(|\tilde{P}_i| + |\tilde{O}_i|\right)^2} \qquad (25)$$

Where (observation (O) and predicted (P)) $\tilde{P}_i = P_i - \overline{O}$. $\tilde{O}_i = O_i - \overline{O}$ and $\overline{O}$ is the mean of the observed data. The index of agreement varies between 0 and 1 where 0 shows the complete disagreement and 1 the perfect agreement.
Table 1 shows index of agreement above 0.98 for this example which certified that the numerical model can predict good results.

Table 1. Index of agreement for Acoustic wave propagation in a wedge-shaped ocean

Receiver Depth	d
30 m	0.9913
150 m	0.9801

6. Conclusions and discussion

Two numerical examples described in the paper certified that the DQ method accuracy and efficiency for solution of acoustic wave equation are appropriate. Even inasmuch as the DQ numerical gain better results rather than other numerical method in some sections by less grid point distribution in the domain.
Even in some sections the DQ model predicted better results than the other numerical results in contrast with analytical solution and benchmark example that was studied here. Note that these results were obtained for less grid point distribution in the computation domain and so the system of linear equations that was obtained by numerical discrete method can be solved by the direct method like gauss elimination.
These (PE) methods. despite their acceptable results for most range and depth dependent problems. are restricted to a small angle approximation and hence. may experience difficulties for long range problems.

References

[1] F.Jensen, W.Kuperman, M.Porter & H.Schmidt. 2011.Computational Ocean Acoustics. AIP Press. New York.

[2] Christian Vanhille and Cleofe Campos-Pozuelo,2000, A time-domain numerical algorithm for the analysis of nonlinear standing acoustic waves, AIP Conference Proceedings 524, 177 (2000); https://doi.org/10.1063/1.1309199.

[3] Wilson Eberle; Zhiliang Zhang; Yan-Fei Liu; Paresh C. Sen,2009, A Practical Switching Loss Model for Buck Voltage Regulators, IEEE Transactions on Power Electronics ,24(3).

[4] Costa. E. G. A.. Godinho. L.. Santiago. J.A.F.. Pereira. A. and Dors. C.. 2011. Efficient numerical models for the prediction of acoustic wave propagation in the vicinity of a wedge coastal region. Engineering Analysis with Boundary Elements. 35(6): 855-867.

[5] Murphy. J.E. and Chin-Bing. S.A.. 1988. A finite element model for ocean acoustic propagation. Mathematical and Computer Modelling. 11(0): 70-74.

[6] K. Kieswetter, Z. Schwartz, D.D. Dean, B.D. Boyan, 1996, The role of Implant Surface Characteristics In the Healing of Bone. Crit Rev Oral Biol Med. 7(4):329-45. doi: 10.1177/10454411960070040301.

[7] R. Bellman, B.G. Kashef, J. Casti

[8] Differential Quadrature: A Thechnique for the rapid solution of non linear partial differential equations. J. Comp. Phys., 10 (40) (1972), p. 52

[9] Shu. C. . 2000. Differential Quadrature and Its Applications in Engineering. Springer-Verlag. Berlin.

[10] Wu, Y., Shu, C. Development of RBF-DQ method for derivative approximation and its application to simulate natural convection in concentric annuli. Computational Mechanics 29, 477–485 (2002). https://doi.org/10.1007/s00466-002-0357-4

[11] Shu. C. and Fan. L. F..2001. A New Discretization Method and Its Application to Solve Incompressible Navier-Stokes Equation. Comput. Mech.. vol. 27. pp. 292–301.

[12] Wei Chen, Vijay Panchang, Zeki Demirbilek, 2001, On the modeling of wave–current interaction using the elliptic mild-slope wave equation, Ocean Engineering 32(17-18):2135-2164.

[13] Joe, H. and Xu, J. (1996) The Estimation Method of Inference Functions for Margins for Multivariate Models. Technical Report No. 166, Department of Statistics, University of British Columbia, Vancouver.

[14] Panchang. V.G.. Pearce. B.R.. Wei. G. and Cushman-Roisin. B.. 1991. Solution of the mild-slope wave problem by iteration. Applied Ocean Research. 13(4): 187-199.